Journal of the Mechanics and Physics of Solids 133 (2019) 103709

Contents lists available at ScienceDirect

Journal of the Mechanics and Physics of Solids

journal homepage: www.elsevier.com/locate/jmps

Diffraction-based misorientation mapping: A continuum mechanics description

Shao-Shi Rui[a,b], Li-Sha Niu[a], Hui-Ji Shi[a,*], Shaolou Wei[b], C. Cem Tasan[b,**]

[a] Applied Mechanics Laboratory, School of Aerospace Engineering, Tsinghua University, Beijing 100084, China
[b] Department of Materials Science and Engineering, Massachusetts Institute of Technology, Cambridge, MA 02139, United States

ARTICLE INFO

Article history:
Received 14 February 2019
Revised 24 June 2019
Accepted 4 September 2019
Available online 5 September 2019

Keywords:
Misorientation
KAM and **GROD**
EBSD-ECCI-DIC
Dislocations
Crystal plasticity

ABSTRACT

As the typical intragranular misorientation parameters, Kernel Averaged Misorientation (**KAM**) and Grain Reference Orientation Deviation (**GROD**) are widely used in diffraction-based misorientation mapping, while their evolution laws under various conditions and physical meanings in continuum mechanics description are rarely investigated systematically. Therefore, we designed several comparative experiments considering the influences of grain boundaries (single-crystalline vs. poly-crystalline), sample geometries (smooth vs. notched) and plastic strain modes (tension vs. buckling) on **KAM** & **GROD** evolution, and captured the intragranular misorientation, dislocation density, and material distortion synchronously based on coupled EBSD-ECCI-DIC mapping in this research. Meanwhile, we also discussed the physical meanings of **KAM** & **GROD** based on continuum mechanics description and provided the theoretical explanations to phenomena observed in the above experiments. **KAM** results from three in-surface invariants ($\rho^{\mathrm{I}}_{\mathrm{GND}}$, $\rho^{\mathrm{II}}_{\mathrm{GND}}$ & $\rho^{\mathrm{III}}_{\mathrm{GND}}$) of GND density tensor $\boldsymbol{\rho}_{\mathbf{GND}}$ induced by plastic strain distribution incompatible with the activated slip systems in unloaded elastic-plastic condition, which cause the same lattice curvature effects as three elastic strain modes with non-zero curl (buckling, in-surface bending & torsion) in purely elastic condition. **GROD** reflects neither local plastic strain nor local material rotation alone, but its "V-type" distribution near the neutral surface reflects the buckling curvature of single-crystal. Besides, $\overline{\mathbf{KAM}}$ & $\overline{\mathbf{GROD}}$ averaged over multiple grains can be used to estimate the nominal plastic strain applied in poly-crystal.

1. Introduction

Two-dimensional Electron Back-Scattered Diffraction (2D-EBSD) based misorientation mapping method is now a standard analysis of plastically deformed crystalline metals and alloys (Kamaya et al., 2005; Kamaya et al., 2006; Schwartz et al., 2009). Different from the intergranular misorientation between two sides of grain boundary, the intragranular misorientation usually corresponds to grain distortion and a category of dislocations termed "geometrically necessary dislocations (GND)" (Gao and Huang, 2003). An important application of diffraction-based misorientation analysis is to exactly determine the GND density based on the continuum dislocation description established by Nye (1953), Bilby et al. (1955) and Kröner (1958). Representative studies regarding this application were pioneered by Adams (1997), El-Dasher et al. (2003) and

* Corresponding author at: Room N-513, Mong Man Wai Building of Science and Technology, Tsinghua University, Beijing 100084, China.
** Corresponding author at: Building 8-202, Massachusetts Institute of Technology, 77 Massachusetts Avenue, Cambridge, MA 02139, United States.
E-mail addresses: rss14@mails.tsinghua.edu.cn, rss18@mit.edu (S.-S. Rui), shihj@mail.tsinghua.edu.cn (H.-J. Shi), tasan@mit.edu (C.C. Tasan).

https://doi.org/10.1016/j.jmps.2019.103709
0022-5096/

Sun et al. (2000), and then continued by Field et al. (2005), Pantleon (2005,2008), Wallis et al. (2017,2016), Vilalta-Clemente et al. (2017), Littlewood and Wilkinson (2012), Jiang et al. (2013), Jiang et al. (2013), Konijnenberg et al. (2015), Calcagnotto et al. (2010), Sarac et al. (2016), Sarac and Kysar (2018), Kysar et al. (2010), Kysar et al. (2007), Dahlberg et al. (2014) and Dahlberg et al. (2017) in the last decades, mostly for the High-Resolution (HR) EBSD community which requires high spatial and angular resolution. Another common application of diffraction-based misorientation analysis aimed at commercial EBSD users is to assess the plastic deformation induced lattice curvature by intragranular misorientation parameters, which can serve as the indicator of dislocation density and material distortion in metallic materials (Kobayashi et al., 2013; Kobayashi et al., 2015). Typical intragranular misorientation parameters, including Kernel Averaged Misorientation (**KAM)** representing the local orientation gradient and Grain Reference Orientation Deviation (**GROD)** representing the intragranular orientation deviation, have been widely used for the failure analysis of metallic materials since they were firstly proposed by Wright et al. (2011,2016) and then summarized in Refs. Lehockey et al. (2000) and Brewer et al. (2009). Here **KAM** is typically defined as the average misorientation between a kernel point and its surrounding points excluding those out of grain boundary, while **GROD** is typically defined as the misorientation between an individual point and the intragranular reference point.

Kamaya et al. (2007,2009,2011) carried out a series of EBSD observations on plastically deformed austenitic stainless steels, revealing that the local misorientation parameter $\mathbf{M}_{\mathrm{L}}$ and its average value $\mathbf{M}_{\mathrm{ave}}$ (equivalent to $\overline{\mathbf{KAM}}$ averaged over multiple grains) as well as the crystal deformation parameter $\mathbf{C}_{\mathrm{d}}$ and its modified value **MCD** (equivalent to $\overline{\mathbf{GROD}}$ averaged over multiple grains) increase with the applied nominal plastic strain linearly. Fujiyama et al. (2009a,2009b,2007) used the decrease law of $\overline{\mathbf{KAM}}$ averaged over multiple grains obtained from the interrupted creep samples to track the dislocation recovery process in high chromium heat resistant steels, and thereby proposed a feasible EBSD analysis method for creep damage evaluation. Kobayashi et al. (2013) used the distribution curve of $\overline{\mathbf{GROD}}$ averaged over multiple grains measured in the cross section of ruptured samples to identify the various fracture modes of Ni-based superalloy, revealing that the cumulative plasticity distribution perpendicular to the fracture surface is significantly different under tension, impact, fatigue and creep conditions. Some typical failure characteristics, such as multiple slip traces, persistent slip bands and fatigue striations (Kobayashi et al., 2015; Kobayashi et al., 2014), can also be observed in **KAM** and **GROD** maps in some cases. In our previous work, the diffraction-based misorientation maps by **KAM** and **GROD** parameters were used in grain boundary micro-cracking analysis (Wei et al., 2019) of high-entropy alloys, fracture modes identification (Rui et al., 2017) and fatigue crack tip driving force prediction (Rui et al., 2018) of low alloy steels, as well as creep damage evaluation (Rui et al., 2018) of austenitic stainless steels.

Though widely used in plastic deformation and damage characterization of metallic materials, rigorous continuum mechanical descriptions of **KAM** and **GROD** are not present. **KAM** is usually regarded as a qualitative description of GND density distribution in both single-crystalline (SC) and poly-crystalline (PC) metallic materials (Calcagnotto et al., 2010; Kubushiro et al., 2015). But the specific in-surface invariants of GND density tensor $\boldsymbol{\rho}_{\mathrm{GND}}$ it reflects under the framework of continuum dislocation theory, as well as the evolution law it follows with respect to material distortion (both plastic strain and material rotation) have not yet been clarified, even contradictory phenomena were sometimes reported in the literature. The previous results reported by our co-author in Refs. Tasan et al. (2014a,2014b) verified that the **KAM** distribution does not strictly correspond to the von-Mises equivalent plastic strain distribution within each single grain, though $\overline{\mathbf{KAM}}$ averaged over multiple grains indeed increased with applied nominal plastic strain linearly (Shen and Efsing, 2018). Worse than **KAM** describing GND density distribution, **GROD** does not have physical meanings, only a linear correlation between $\overline{\mathbf{GROD}}$ averaged over multiple grains and applied nominal plastic strain has been revealed (Kamaya et al., 2005; Kamaya et al., 2006). In the absence of clear physical descriptions, the theoretical foundation of the applications of these intragranular misorientation parameters in plastic deformation and damage characterization cannot be rigorously justified. Thus the core of this research is to address this challenge by connecting crystallographic metrics and continuum descriptions thereof.

Theoretically, we rewrote the definitions of **KAM** and **GROD** based on orientation gradient tensor $\boldsymbol{\kappa}$ and relative lattice rotation tensor $\boldsymbol{\Delta\Omega}_{\mathrm{lattice}}$ respectively, to assign them detailed physical meanings in continuum mechanics description. **KAM** is actually the average projection of orientation gradient tensor $\boldsymbol{\kappa}$ along two axes $a\vec{\boldsymbol{e}}_1$ and $a\vec{\boldsymbol{e}}_2$ (a is the EBSD scanning step size) under the current 2D coordinate system, while **GROD** reflects the magnitude of relative lattice rotation tensor $\boldsymbol{\Delta\Omega}_{\mathrm{lattice}}$. With that, we then discussed the factors that contribute to the lattice curvature, including three in-surface invariants ($\rho^{\mathrm{I}}_{\mathrm{GND}}$, $\rho^{\mathrm{II}}_{\mathrm{GND}}$ & $\rho^{\mathrm{III}}_{\mathrm{GND}}$) of GND density tensor $\boldsymbol{\rho}_{\mathrm{GND}}$ under unloaded elastic-plastic condition, which cause the same lattice curvature effects as the three elastic strain modes (bending, in-surface buckling & torsion) with non-zero curl under purely elastic condition. The relationship between in-plane lattice rotation θ_3 and in-plane material distortion (plastic strain components: $\varepsilon^{\mathrm{p}}_1$, $\varepsilon^{\mathrm{p}}_2$, γ^{p}_3 and material rotation component ω_3) in SC samples, the dependence of misorientation distribution on the plastic strain modes in SC samples, as well as the linear evolution law of $\overline{\mathbf{KAM}}$ and $\overline{\mathbf{GROD}}$ averaged over multiple grains in PC samples were also clarified from a theoretical view.

Experimentally, we combined two experimental techniques, microscopic Digital Image Correlation (μ-DIC, for determining local material distortion field) and Electron Channeling Contrast Imaging (ECCI, for capturing true dislocations density distribution characteristics), with the aforementioned 2D-EBSD based misorientation mapping method to investigate the internal linkage between intragranular misorientation, dislocation density, and material distortion. μ-DIC based on Secondary Electron (SE) imaging was developed by our co-author in Ref. Yan et al. (2015). Meanwhile, ECCI provides a feasible way for the direct observation of lattice defects via electron channeling contrast shown in Back-Scatter Electron

Table 1
Chemical components of SC and PC Ni-based superalloys (wt. /%).

SC	Cr	Co	Mo	Al	Ti	Ta	W	C	Ni
	12.2	9.0	1.9	3.6	4.1	5.0	3.8	0.07	Bal.
PC	Cr	Co	Mo	Al	Ti	Nb	W	C	Ni
	16.0	13.0	4.0	2.2	3.7	0.8	4.0	0.02	Bal.

(BSE) images, by which we can identify the true dislocations density distribution very close to the polished sample surface (Gutierrez-Urrutia and Raabe, 2012). With the help of in-situ mechanical testing machine and coupled EBSD-ECCI-DIC mapping method, we can then achieve local misorientation, dislocation density and material distortion mapping synchronously on SC and PC Ni-based superalloys. Grain boundaries (SC vs. PC), sample geometries (smooth vs. notched) and plastic strain modes (tension vs. buckling) are three factors producing a great influence on **KAM** and **GROD** evolution. Therefore, comparative experiments were designed in this research to help us understand the evolution laws of **KAM** and **GROD** under various conditions, and reveal the internal linkage between crystallographic metrics and other physical quantities in continuum mechanics description.

2. Materials and experimental methods

2.1. Materials and mechanical tests

The materials used in this research are SC and PC Ni-based superalloys, whose microstructures consist of a high volume fraction γ' (Ni_3Al) precipitates embedded uniformly in the γ (Ni) matrix (Fig. 1a-b). The main chemical components of the selected SC and PC Ni-based superalloys here are summarized in Table 1. The lattice type in Ni-based superalloy is face-centered cubic (FCC) for γ phase, and LI_2 superstructure for γ' phase. LI_2 superstructure is similar with FCC structure except for replacing the nickel atoms in the cubic vertex by aluminum atoms (Fig. 1a). A coherent interfacial relationship exists between the γ and γ' lattice structure, whereby the dislocations originating from γ channels are able to pass the γ' precipitates directly by cut-through instead of bypassing during the plastic deformation at ambient temperature (Fig. 1b). Therefore, the plastic deformation mechanism of the multi-phases Ni-based superalloy here is equivalent to that of the single-phase pure Ni metal, where the continuum mechanics description and the continuum dislocation theory are thus applicative.

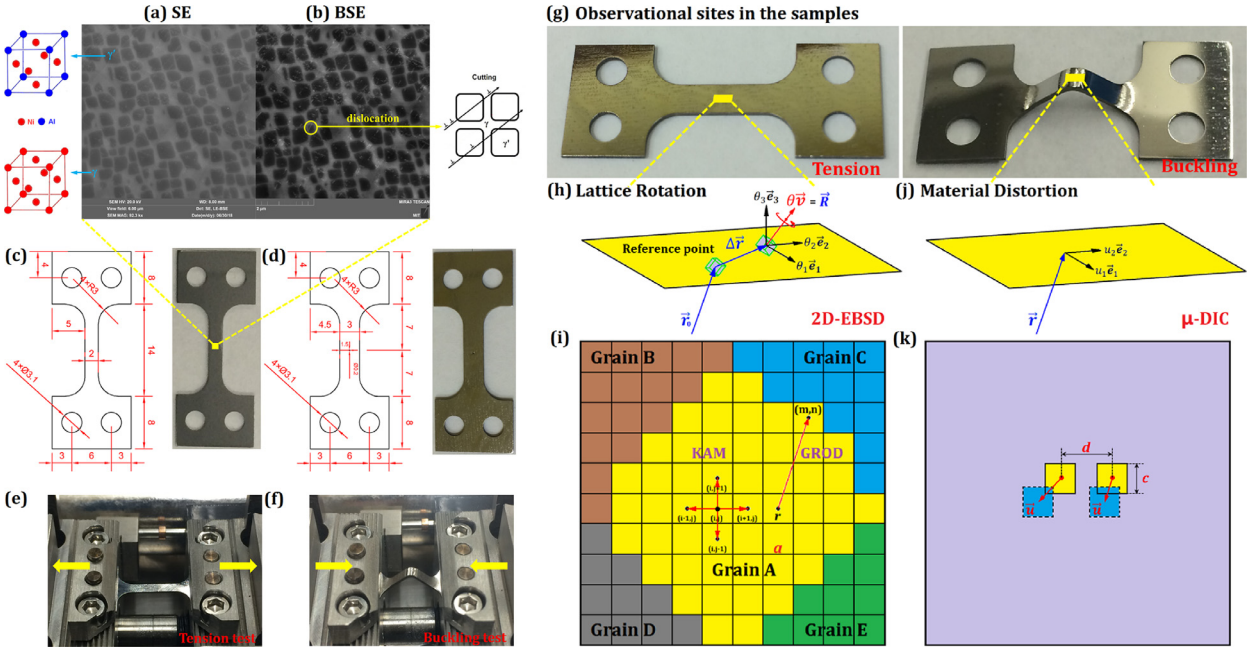

Fig. 1. Microstructural images of Ni-based superalloy taken by (a) SE & (b) BSE detectors, dimensions of (c) smooth & (d) notched samples (unit: mm), (e) tension & (f) buckling tests carried out by Gatan MT10460® 2KN EBSD W/C mechanical testing platform, (g) observational sites in tensile & buckled samples, (h) relative lattice rotation measured by 2D-EBSD, (i) residual material distortion measured by μ-DIC, (j) typical definitions of intragranular misorientation parameters **KAM** & **GROD** and (k) point distance d & facet size c used in μ-DIC analysis.

Table 2
Mechanical test scheme of SC and PC Ni-based superalloys.

Sample No.	#1	#2	#3	#4	#5	#6
Geometry type	Smooth	Smooth	Notched	Smooth	Smooth	Smooth
Material type	SC	PC	SC	SC	SC※	PC
Strain mode	Tension	Tension	Tension	Buckling	Buckling	Buckling

※: Sample #5 here is also SC, but its lattice orientation differs from other SC samples #1, #3 and #4.

Two types of sample geometry (0.5 mm thickness) were prepared for the following mechanical tests. One is smooth sample with 2 mm width (Fig. 1c), and another is centrally notched ($\varnothing = 0.2$ mm) sample with 3 mm width (Fig. 1d). Tension tests (Fig. 1e) were carried out on both smooth and notched samples by a Gatan MT10460® 2KN EBSD W/C mechanical testing platform, while buckling tests (Fig. 1f) were only carried out on smooth samples under compression mode. In total, six mechanical tests were carried out on various SC and PC samples, as shown in Table 2 for details. Meanwhile, three groups of comparison are designed in the test scheme. Firstly, the comparison between SC and PC samples (#1 vs. #2 in tension tests, #4 vs. #6 in buckling tests) will reveal the influence of grain boundaries on misorientation evolution. Secondly, the comparison between smooth and notched SC samples (#1 vs. #3) will display the effect of notch induced plastic strain gradient on misorientation distribution. Thirdly, the comparison between tension and buckling tests (#1 vs. #4 in SC samples, #2 vs. #6 in PC samples) is to investigate the dependence of lattice curvature on plastic strain modes.

2.2. FE-SEM based 2D-EBSD, μ-DIC and ECCI characterizations

The Field Emission Scanning Electron Microscope (FE-SEM) machine type for 2D-EBSD, μ-DIC and ECCI imaging in this research is TESCAN MIRA 3 LMH®, which is equipped with SE detector, BSE detector, Energy Dispersive Spectrometer (EDS) and EBSD camera. SE and BSE images provide detailed information on surface morphology and electron channeling contrast respectively, while EDS and EBSD images display information on surface chemical elements and crystallographic orientations respectively. The 2D-EBSD, μ-DIC and ECCI observational sites are located in the middle axis of gage length in the samples after the finish of mechanical tests (Fig. 1g).

All the samples for EBSD and ECCI imaging were firstly ground by 600#, 800# and 1200# sandpapers respectively to remove the initial surface, then roughly polished by Buehler AutoMet 250® machine with 3um diamond particles for 30∼40 min, and finally followed by 1 h colloidal silica (OPS) fine polishing to release the residual stress in the sample surface. The OPS solution contains weeny SiO_2 particles (∼200 nm) and acid liquid, which can remove the slight deformation layer quickly by coupled mechanical-chemical effects. With respect to the μ-DIC imaging, speckle pattern consisted of OPS particles need to be further prepared after the above polishing procedure finished.

2.2.1. Misorientation mapping based on 2D-EBSD

2D-EBSD technique records the orientation distribution in the polished sample surface point by point as the Euler angles (ϕ_1, ϕ, ϕ_2) through Hough transformation of Kikuchi pattern obtained from backscatter electron diffraction, which represent three relative rotations between local lattice coordinate ([100], [010], [001]) and global sample coordinate (RD, TD, ND). The EBSD camera equipped in the FE-SEM machine here is DigView® produced by EDAX, and the matched software for orientation data collection is EDAX/TSL-OIM Data Collection 8.0®. Three types of EBSD observational region size used in this research are 400×400um (step size $a = 1$um) for coupled EBSD & DIC characterization on samples #1 ∼ #3 (Figs. 6, 7 and 9), 160×720um (step size $a = 0.8$um) for single EBSD characterization on samples #1 ∼ #2 and #4 ∼ #6 (Fig. 13), as well as 6 × 6um (step size $a = 0.02$um) for coupled EBSD & ECCI characterization on sample #4 (Fig. 15). The saved orientation data are post-processed by software EDAX/TSL-OIM Analysis 7.0®. If necessary, these data can also be imported to MATLAB® for further analysis. For the convenience of misorientation calculation, the Euler angles (ϕ_1, ϕ, ϕ_2) are usually converted into the orientation matrix $\boldsymbol{g}$ as shown in Eq. (1):

$$\boldsymbol{g} = \begin{bmatrix} \cos\phi_2 & \sin\phi_2 & 0 \\ -\sin\phi_2 & \cos\phi_2 & 0 \\ 0 & 0 & 1 \end{bmatrix} \begin{bmatrix} 1 & 0 & 0 \\ 0 & \cos\phi & \sin\phi \\ 0 & -\sin\phi & \cos\phi \end{bmatrix} \begin{bmatrix} \cos\phi_1 & \sin\phi_1 & 0 \\ -\sin\phi_1 & \cos\phi_1 & 0 \\ 0 & 0 & 1 \end{bmatrix} \tag{1}$$

In the undeformed crystalline metallic materials without any initial dislocations, the orientation distribution within each single grain is uniform everywhere: $\boldsymbol{g}(\vec{\boldsymbol{r}}_1) = \boldsymbol{g}(\vec{\boldsymbol{r}}_2) = \cdots =$ Constant. Accompanied by the crystal deformation, local lattice will be gradually curved due to the inhomogeneous elastic strain or plastic incompatibility, and thus misorientation $\Delta\boldsymbol{g}(\vec{\boldsymbol{r}}_1, \vec{\boldsymbol{r}}_2) = \boldsymbol{g}(\vec{\boldsymbol{r}}_1) \cdot \boldsymbol{g}(\vec{\boldsymbol{r}}_2)^{-1}$ appears in this case. Then the orientation matrix $\boldsymbol{g}$ becomes position $\vec{\boldsymbol{r}}$ dependent, which can be described by an orientation matrix field $\boldsymbol{g}(\vec{\boldsymbol{r}})$. In order to characterize the orientation gradient and inhomogeneous lattice rotation in the deformed crystal, we select a reference position $\vec{\boldsymbol{r}}_0$ representing the undeformed area to remove the homogeneous part of total lattice rotation. The relative position vector $\Delta\vec{\boldsymbol{r}}$ between the individual point $\vec{\boldsymbol{r}}$ and the selected reference position $\vec{\boldsymbol{r}}_0$ can be further decomposed into two components $x_1\vec{\boldsymbol{e}}_1$ and $x_2\vec{\boldsymbol{e}}_2$ under the current coordinate system as shown in Eq. (2), while the third component $x_3\vec{\boldsymbol{e}}_3$ under the 2D-EBSD characterization condition is identically equal to zero.

$$\Delta\vec{\boldsymbol{r}} = x_1\vec{\boldsymbol{e}}_1 + x_2\vec{\boldsymbol{e}}_2 \tag{2}$$

The misorientation matrix $\Delta \boldsymbol{g}(\boldsymbol{\Delta}\vec{\boldsymbol{r}})$ between the individual point and selected reference position can be calculated according to Eq. (3):

$$\Delta \boldsymbol{g}(\boldsymbol{\Delta}\vec{\boldsymbol{r}}) = \boldsymbol{g}(\vec{\boldsymbol{r}}_0 + \boldsymbol{\Delta}\vec{\boldsymbol{r}}) \cdot \boldsymbol{g}(\vec{\boldsymbol{r}}_0)^{-1} \tag{3}$$

As a common measure of relative lattice rotation, the rotation angle θ and axis $\vec{\boldsymbol{v}}$ can also be derived from the above misorientation matrix $\Delta \boldsymbol{g}(\boldsymbol{\Delta}\vec{\boldsymbol{r}})$ (Pantleon, 2008) as shown in Eq. (4):

$$\theta = \arccos\left(\frac{\Delta g_{ii} - 1}{2}\right), \ \vec{\boldsymbol{v}} = \frac{-\epsilon_{ijk}\Delta g_{ij}}{2\sin\theta}\vec{\boldsymbol{e}}_k \tag{4}$$

The relative lattice rotation vector $\vec{\boldsymbol{R}}$ made up of rotation angle θ and axis $\vec{\boldsymbol{v}}$ can also be decomposed into three components $\theta_1\vec{\boldsymbol{e}}_1$, $\theta_2\vec{\boldsymbol{e}}_2$ and $\theta_3\vec{\boldsymbol{e}}_3$ under the current coordinate system when the lattice rotation angle θ is a small, as shown in Fig. 1h and Eq. (5):

$$\vec{\boldsymbol{R}}(\boldsymbol{\Delta}\vec{\boldsymbol{r}}) = \theta\vec{\boldsymbol{v}} = \theta_1(\boldsymbol{\Delta}\vec{\boldsymbol{r}})\vec{\boldsymbol{e}}_1 + \theta_2(\boldsymbol{\Delta}\vec{\boldsymbol{r}})\vec{\boldsymbol{e}}_2 + \theta_3(\boldsymbol{\Delta}\vec{\boldsymbol{r}})\vec{\boldsymbol{e}}_3 \tag{5}$$

Then the relative lattice rotation tensor $\Delta\boldsymbol{\Omega}_{\text{lattice}}$ is the conjugated two-order tensor of the above relative lattice rotation vector $\vec{\boldsymbol{R}}$, which is an antisymmetric tensor generated by the production of negative Eddington tensor $-\epsilon$ and relative lattice rotation vector $\vec{\boldsymbol{R}}$ as shown in Eq. (6):

$$\Delta\boldsymbol{\Omega}_{\text{lattice}}(\boldsymbol{\Delta}\vec{\boldsymbol{r}}) = \boldsymbol{\Omega}_{\text{lattice}}(\vec{\boldsymbol{r}}_0 + \boldsymbol{\Delta}\vec{\boldsymbol{r}}) - \boldsymbol{\Omega}_{\text{lattice}}(\vec{\boldsymbol{r}}_0) = -\epsilon \cdot \vec{\boldsymbol{R}}(\boldsymbol{\Delta}\vec{\boldsymbol{r}}) = \begin{bmatrix} 0 & \theta_3 & -\theta_2 \\ -\theta_3 & 0 & \theta_1 \\ \theta_2 & -\theta_1 & 0 \end{bmatrix} \tag{6}$$

Then the orientation gradient tensor $\boldsymbol{\kappa}$ can be derived from the gradient of lattice rotation vector $\vec{\boldsymbol{R}}$ with respect to relative position vector $\boldsymbol{\Delta}\vec{\boldsymbol{r}}$. Tensor $\boldsymbol{\kappa}$ here is also named after "Nye's tensor" because it was firstly introduced by Nye (1953) in his continuum dislocation theory, which describes the lattice curvature in dislocated crystals as shown in Eq. (7):

$$\boldsymbol{\kappa}(\Delta\vec{\boldsymbol{r}}) \overset{\text{def}}{=} \nabla\vec{\boldsymbol{R}}(\boldsymbol{\Delta}\vec{\boldsymbol{r}}) = \frac{\partial\vec{\boldsymbol{R}}}{\partial x_1}\vec{\boldsymbol{e}}_1 + \frac{\partial\vec{\boldsymbol{R}}}{\partial x_2}\vec{\boldsymbol{e}}_2 + \frac{\partial\vec{\boldsymbol{R}}}{\partial x_3}\vec{\boldsymbol{e}}_3 = \begin{bmatrix} \frac{\partial\theta_1}{\partial x_1} & \frac{\partial\theta_1}{\partial x_2} & \frac{\partial\theta_1}{\partial x_3} \\ \frac{\partial\theta_2}{\partial x_1} & \frac{\partial\theta_2}{\partial x_2} & \frac{\partial\theta_2}{\partial x_3} \\ \frac{\partial\theta_3}{\partial x_1} & \frac{\partial\theta_3}{\partial x_2} & \frac{\partial\theta_3}{\partial x_3} \end{bmatrix} = \lim_{a\to 0}\begin{bmatrix} \frac{\theta_{11}}{a} & \frac{\theta_{21}}{a} & \boxtimes \\ \frac{\theta_{12}}{a} & \frac{\theta_{22}}{a} & \boxtimes \\ \frac{\theta_{13}}{a} & \frac{\theta_{23}}{a} & \boxtimes \end{bmatrix} \tag{7}$$

In particular, the approximate gradient of relative rotation component θ_j along the x_i direction can be calculated as Eq. (8) by 2D-EBSD scanning with a small step size a, while three components θ_{31}, θ_{32} and θ_{33} in the orientation gradient tensor $\boldsymbol{\kappa}$ are unmeasurable (represented by "$\boxtimes$" in Eqs. (7), (12) and (14)) because the relative position vector change $d\vec{\boldsymbol{r}}$ is confined to two dimensions.

$$\frac{\partial\theta_j}{\partial x_i} = \lim_{a\to 0}\frac{\theta_j(\boldsymbol{\Delta}\vec{\boldsymbol{r}} + a\vec{\boldsymbol{e}}_i) - \theta_j(\boldsymbol{\Delta}\vec{\boldsymbol{r}})}{a} = \lim_{a\to 0}\frac{\theta_{ij}}{a}, \ \theta_{ij} = \theta_j(\boldsymbol{\Delta}\vec{\boldsymbol{r}} + a\vec{\boldsymbol{e}}_i) - \theta_j(\boldsymbol{\Delta}\vec{\boldsymbol{r}}) \tag{8}$$

KAM and **GROD** are actually scalars proposed for the convenience of quantifying the extent of local orientation gradient and relative lattice rotation respectively. However, the typical definition (see Fig. 1i and Eq. (9)) of **KAM** widely reported in current literatures (Wright et al., 2011; Wright et al., 2016; Lehockey et al., 2000; Brewer et al., 2009) only takes the rotation angle θ between kernel point (i, j) and its four surrounding points $(i \pm 1, j \pm 1)$ into consideration, but ignores the rotation axis $\vec{\boldsymbol{v}}$. The same problem also exists in the typical definition of **GROD**, which leads to information loss of the above misorientation parameters in continuum mechanics description.

$$\mathbf{KAM}^{\text{typ}}(i,j) \overset{\text{def}}{=} \frac{1}{4}\left(\theta|_{(i,j)}^{(i-1,j)} + \theta|_{(i,j)}^{(i+1,j)} + \theta|_{(i,j)}^{(i,j-1)} + \theta|_{(i,j)}^{(i,j+1)}\right), \ \mathbf{GROD}^{\text{typ}}(m,n) \overset{\text{def}}{=} \theta|_{r}^{(m,n)} \tag{9}$$

To have a better understanding on the physical meanings of misorientation parameters in continuum mechanics description, we hereby rewrite the definitions of **KAM** and **GROD** based on orientation gradient tensor $\boldsymbol{\kappa}$ and relative lattice rotation tensor $\Delta\boldsymbol{\Omega}_{\text{lattice}}$ respectively, which will not change their physical essence but deepen their physical connotation. The misorientation angle along two axes $d\vec{\boldsymbol{r}} = a\vec{\boldsymbol{e}}_1$ and $a\vec{\boldsymbol{e}}_2$ can be expressed as $\theta|_{(i,j)}^{(i\pm1,j)} = |\boldsymbol{\kappa}\cdot a\vec{\boldsymbol{e}}_1|$ and $\theta|_{(i,j)}^{(i,j\pm1)} = |\boldsymbol{\kappa}\cdot a\vec{\boldsymbol{e}}_2|$ respectively, thus **KAM** can be then rewritten as the average projection of orientation gradient tensor:

$$\mathbf{KAM} \overset{\text{def}}{=} \frac{a}{2}|\boldsymbol{\kappa}\cdot\vec{\boldsymbol{e}}_1| + \frac{a}{2}|\boldsymbol{\kappa}\cdot\vec{\boldsymbol{e}}_2| = \frac{1}{2}\sqrt{(\theta_{11})^2 + (\theta_{12})^2 + (\theta_{13})^2} + \frac{1}{2}\sqrt{(\theta_{21})^2 + (\theta_{22})^2 + (\theta_{23})^2} \tag{10}$$

GROD can be rewritten as the magnitude of relative lattice rotation vector or its conjugated tensor:

$$\mathbf{GROD} \overset{\text{def}}{=} \left|\vec{\boldsymbol{R}}\right| = \sqrt{\frac{1}{2}\Delta\boldsymbol{\Omega}_{\text{lattice}} : \Delta\boldsymbol{\Omega}_{\text{lattice}}} = \sqrt{(\theta_1)^2 + (\theta_2)^2 + (\theta_3)^2} \tag{11}$$

The above new definitions based on continuum mechanics description bring about the following two insights: (i) **KAM** is not an objective scalar since it relies on the EBSD step size a and 2D coordinate system $(\vec{\boldsymbol{e}}_1,\vec{\boldsymbol{e}}_2)$, and (ii) **GROD** is an objective scalar for it is independent of the above two factors.

2.2.2. Residual material distortion mapping based on μ-DIC

To achieve the μ-DIC mapping of residual material distortion field after unloading, speckle patterns made up of OPS particles should be prepared on the polished sample surface as follows after the final polishing procedure. On a clean polishing cloth plate, 10∼20 drops of OPS solution were placed along the circumferential direction. Then the sample was pressed by fingers on the cloth plate rotated at 100 RPM speed with water flushing for 10 s. Finally, the sample surface was rinsed with ethanol, and dried by an air fan. The above steps are supposed to create a uniform layer of SiO_2 particles deposition, serving as speckle patterns to track material point trajectory during deformation.

μ-DIC technique measures the 2D displacement field $\vec{\boldsymbol{u}}(\vec{\boldsymbol{r}}) = u_1\vec{\boldsymbol{e}}_1 + u_2\vec{\boldsymbol{e}}_2$ on the polished sample surface through tracking the trajectory of OPS particles in the view of field during deformation (Fig. 1j). The SE images for correlation here were taken under a high resolution (4096×4096 pixels) and low scanning speed (speed 8 in TESCAN operating system) conditions so as to clearly identify each OPS particle. The point distance d and facet size c (Fig. 1k) used in the DIC software GOM Correlate 2017® here are 9 pixels and 12 pixels respectively. The residual distortion tensor $\tilde{\boldsymbol{\beta}}$ is calculated from the gradient of displacement vector $\vec{\boldsymbol{u}}$ with respect to position vector $\vec{\boldsymbol{r}}$ as follows:

$$\tilde{\boldsymbol{\beta}}(\vec{\boldsymbol{r}}) \overset{\text{def}}{=} \nabla\vec{\boldsymbol{u}}(\vec{\boldsymbol{r}}) = \frac{\partial\vec{\boldsymbol{u}}}{\partial x_1}\vec{\boldsymbol{e}}_1 + \frac{\partial\vec{\boldsymbol{u}}}{\partial x_2}\vec{\boldsymbol{e}}_2 + \frac{\partial\vec{\boldsymbol{u}}}{\partial x_3}\vec{\boldsymbol{e}}_3 = \begin{bmatrix} \frac{\partial u_1}{\partial x_1} & \frac{\partial u_1}{\partial x_2} & \frac{\partial u_1}{\partial x_3} \\ \frac{\partial u_2}{\partial x_1} & \frac{\partial u_2}{\partial x_2} & \frac{\partial u_2}{\partial x_3} \\ \frac{\partial u_3}{\partial x_1} & \frac{\partial u_3}{\partial x_2} & \frac{\partial u_3}{\partial x_3} \end{bmatrix} = \lim_{d\to 0}\begin{bmatrix} \frac{u_{11}}{d} & \frac{u_{21}}{d} & \boxtimes \\ \frac{u_{12}}{d} & \frac{u_{22}}{d} & \boxtimes \\ \boxtimes & \boxtimes & \boxtimes \end{bmatrix} \tag{12}$$

The same as before, the approximate gradient of displacement component u_j along the x_i direction can be expressed as Eq. (13). But five components $u_{31}, u_{13}\ u_{32}\ u_{23}$ and u_{33} are unmeasurable because both displacement vector change $d\vec{\boldsymbol{u}}$ and position vector change $d\vec{\boldsymbol{r}}$ were confined to two dimensions.

$$\frac{\partial u_j}{\partial x_i} = \lim_{d\to 0}\frac{u_j(\vec{\boldsymbol{r}} + d\vec{\boldsymbol{e}}_i) - u_j(\vec{\boldsymbol{r}})}{d} = \lim_{d\to 0}\frac{u_{ij}}{d},\ u_{ij} = u_j(\vec{\boldsymbol{r}} + d\vec{\boldsymbol{e}}_i) - u_j(\vec{\boldsymbol{r}}) \tag{13}$$

Furthermore, the residual material distortion tensor $\tilde{\boldsymbol{\beta}}$ can be decomposed into the symmetric part ε^{p} (plastic strain tensor) and anti-symmetric part $\boldsymbol{\Omega}_{\text{material}}$ (material rotation tensor), as shown in Eq. (14). The von-Mises equivalent plastic strain $\varepsilon_{\mathrm{v}}^{\mathrm{p}}$ here is a scalar widely used for measuring the extent of local plastic strain in the μ-DIC mapping.

$$\boldsymbol{\varepsilon}^{\mathrm{p}} = \frac{1}{2}\left(\tilde{\boldsymbol{\beta}} + \tilde{\boldsymbol{\beta}}^{\mathrm{T}}\right) = \begin{bmatrix} \varepsilon_1^{\mathrm{p}} & \gamma_3^{\mathrm{p}} & \boxtimes \\ \gamma_3^{\mathrm{p}} & \varepsilon_2^{\mathrm{p}} & \boxtimes \\ \boxtimes & \boxtimes & \boxtimes \end{bmatrix},\ \boldsymbol{\Omega}_{\text{material}} = \frac{1}{2}\left(\tilde{\boldsymbol{\beta}} - \tilde{\boldsymbol{\beta}}^{\mathrm{T}}\right) = \begin{bmatrix} 0 & \omega_3 & \boxtimes \\ -\omega_3 & 0 & \boxtimes \\ \boxtimes & \boxtimes & 0 \end{bmatrix},\ \varepsilon_{\mathrm{v}}^{\mathrm{p}} = \sqrt{\frac{2}{3}\boldsymbol{\varepsilon}^{\mathrm{p}} : \boldsymbol{\varepsilon}^{\mathrm{p}}} \tag{14}$$

Coupled EBSD and DIC analysis should in principle enable the comparison between misorientation parameters measured by EBSD and residual material distortion measured by μ-DIC, from which we can interpret their linkage.

2.2.3. True dislocation density mapping based on ECCI

ECCI image is actually a high resolution (2048×2048 pixels, speed 7) BSE image taken with a short working distance (WD = 8 mm) and high channeling contrast. The channeling contrast ratio shown in the BSE image relies on the diffraction condition and becomes strongest when the incident and transmission beams yield the so-called "two-beam condition" (Zaefferer and Elhami, 2014). In the actual operation, we rotate or tilt the sample continuously (0.5° per step) in the SEM machine to observe the change of channeling contrast ratio, until the dislocation looks bright in the dark background as shown in Fig. 1b.

ECCI technique can identify true dislocation density distribution near the carefully polished sample surface. However, total true dislocations consist of two parts: the aforementioned GND induced by incompatible plastic strain, as well as Statistically Storage Dislocation (SSD) induced by compatible plastic strain. According to the continuum dislocation theory established by Nye (1953) and Bilby et al. (1955) and Kröner (1958) et.al, GND beyond a specific characteristic scale is determined by the orientation gradient measured under the corresponding spatial resolution, while SSD stored within this characteristic scale does not contribute to lattice curvature due to the offset between positive and negative effects (Arsenlis and Parks, 1999). The smaller the characteristic scale, the more percentage the GND occupies in total true dislocations, as shown in Fig. A2 of the Appendix I. All the true dislocations will be categorized as GND when the characteristic scale is even smaller than the dislocation dipole size (J. Jiang et al., 2013).

ECCI technique cannot distinguish the GND from total true dislocations, while EBSD based **KAM** mapping can only identify the distribution of GND density associated with the specific characteristic scale (i.e. EBSD scanning step size a) rather than SSD density. Coupled EBSD and ECCI analysis here enables the comparison between true dislocations distribution directly observed by ECCI and GND distribution indirectly evaluated by EBSD (Rogowitz et al., 2018), from which a better understanding on the dislocation characterization by diffraction-based misorientation mapping can be accomplished.

3. Theoretical description on the physical meanings of KAM and GROD

3.1. Origin of lattice curvature during crystal deformation

Under small elastic-plastic deformation assumption, the total material distortion tensor $\boldsymbol{\beta}$ can be additively decomposed into two parts: the elastic distortion tensor $\boldsymbol{\beta}^{\mathrm{e}}$and the plastic distortion tensor $\boldsymbol{\beta}^{\mathrm{p}}$. Furthermore, both the elastic and plastic distortion tensors can be additively decomposed into the antisymmetric part: lattice rotation $\boldsymbol{\Omega}_{\mathrm{lattice}}$ and non-lattice rotation $\boldsymbol{\Omega}_{\mathrm{non-lattice}}$, as well as the symmetric part: elastic strain ε^{e} and plastic strain ε^{p}, as shown in Eq. (15). Following the continuum dislocation theory established by Nye (1953), Bilby et al. (1955) and Kröner (1958) and well summarized in the work of Sun et al. (2000,1998), the GND density tensor $\boldsymbol{\rho}_{\mathrm{GND}}$ made up of the $1^{\mathrm{st}}\cdots\alpha^{\mathrm{th}}\cdots k^{\mathrm{th}}$ type GND density $\rho^{\alpha}_{\mathrm{GND}}$ (burgers vector $\vec{\boldsymbol{b}}^{\alpha}$, dislocation line unit vector $\vec{\boldsymbol{t}}^{\alpha}$) can be calculated from the curl of elastic distortion tensor $\boldsymbol{\beta}^{\mathrm{e}}\times\nabla$. A detailed derivation of Eq. (15) is given in the Appendix I.

$$\boldsymbol{\beta}=\boldsymbol{\beta}^{\mathrm{e}}+\boldsymbol{\beta}^{\mathrm{p}}\ =\boldsymbol{\Omega}_{\mathrm{lattice}}+\boldsymbol{\varepsilon}^{\mathrm{e}}+\boldsymbol{\Omega}_{\mathrm{non-lattice}}+\boldsymbol{\varepsilon}^{\mathrm{p}},\ \ \boldsymbol{\rho}_{\mathrm{GND}}\overset{\mathrm{def}}{=}\sum_{\alpha=1}^{k}\rho^{\alpha}_{\mathrm{GND}}\vec{\boldsymbol{b}}^{\alpha}\vec{\boldsymbol{t}}^{\alpha}=\boldsymbol{\beta}^{\mathrm{e}}\times\nabla \tag{15}$$

The EBSD measurable misorientation information is stored in the above lattice rotation item $\boldsymbol{\Omega}_{\mathrm{lattice}}$. The orientation gradient tensor $\boldsymbol{\kappa}$ can be naturally derived from the curl of lattice rotation item $\boldsymbol{\Omega}_{\mathrm{lattice}}\times\nabla$ as shown in Eq. (16), whose detailed derivation is given in the Appendix II. Replacing the $\boldsymbol{\Omega}_{\mathrm{lattice}}\times\nabla$ by $\boldsymbol{\rho}_{\mathrm{GND}}-\boldsymbol{\varepsilon}^{\mathrm{e}}\times\nabla$ according to the above calculation method of GND density tensor $\boldsymbol{\rho}_{\mathrm{GND}}=\boldsymbol{\beta}^{\mathrm{e}}\times\nabla=\boldsymbol{\Omega}_{\mathrm{lattice}}\times\nabla+\boldsymbol{\varepsilon}^{\mathrm{e}}\times\nabla$, we can see clearly that the lattice curvature during the crystal deformation results from two aspects: (i) the elastic strain with non-zero curl (including the strain modes of buckling, bending and torsion) and (ii) the GND induced by plastic incompatibility.

$$\boldsymbol{\kappa}=\frac{1}{2}[(\boldsymbol{\Omega}_{\mathrm{lattice}}\times\nabla):\mathbf{I}]\mathbf{I}-(\boldsymbol{\Omega}_{\mathrm{lattice}}\times\nabla)^{\mathrm{T}}=\underbrace{(\boldsymbol{\varepsilon}^{\mathrm{e}}\times\nabla)^{\mathrm{T}}}_{\text{elastic buckling/bending/torsion}}+\underbrace{\left[\frac{1}{2}(\boldsymbol{\rho}_{\mathrm{GND}}:\mathbf{I})\mathbf{I}-\boldsymbol{\rho}^{\mathrm{T}}_{\mathrm{GND}}\right]}_{\text{GND (plastic incompatibility)}} \tag{16}$$

For purely elastic condition, the GND density tensor $\boldsymbol{\rho}_{\mathrm{GND}}$ in the elastically deformed crystal is approximately equal to zero if the initial dislocation density is infinitesimal, thus the orientation gradient $\boldsymbol{\kappa}$ in this case is only induced by the aforementioned elastic strain with non-zero curl, including buckling, bending and torsion as shown in Fig. A1b. The contribution of elastic strain components gradient $\partial\varepsilon^{\mathrm{e}}_{i}/\partial x_{j}$ and $\partial\gamma^{\mathrm{e}}_{i}/\partial x_{j}$ to orientation gradient components is shown in Eq. (17):

$$\boldsymbol{\rho}_{\mathrm{GND}}\approx 0,\ \boldsymbol{\kappa}=(\boldsymbol{\varepsilon}^{\mathrm{e}}\times\nabla)^{\mathrm{T}}=\begin{bmatrix}-\dfrac{\partial\gamma^{\mathrm{e}}_{2}}{\partial x_{2}}+\dfrac{\partial\gamma^{\mathrm{e}}_{3}}{\partial x_{3}} & \dfrac{\partial\varepsilon^{\mathrm{e}}_{2}}{\partial x_{3}}-\dfrac{\partial\gamma^{\mathrm{e}}_{1}}{\partial x_{2}} & -\dfrac{\partial\varepsilon^{\mathrm{e}}_{3}}{\partial x_{2}}+\dfrac{\partial\gamma^{\mathrm{e}}_{1}}{\partial x_{3}}\\ -\dfrac{\partial\varepsilon^{\mathrm{e}}_{1}}{\partial x_{3}}+\dfrac{\partial\gamma^{\mathrm{e}}_{2}}{\partial x_{1}} & -\dfrac{\partial\gamma^{\mathrm{e}}_{3}}{\partial x_{3}}+\dfrac{\partial\gamma^{\mathrm{e}}_{1}}{\partial x_{1}} & \dfrac{\partial\varepsilon^{\mathrm{e}}_{3}}{\partial x_{1}}-\dfrac{\partial\gamma^{\mathrm{e}}_{2}}{\partial x_{3}}\\ \dfrac{\partial\varepsilon^{\mathrm{e}}_{1}}{\partial x_{2}}-\dfrac{\partial\gamma^{\mathrm{e}}_{3}}{\partial x_{1}} & -\dfrac{\partial\varepsilon^{\mathrm{e}}_{2}}{\partial x_{1}}+\dfrac{\partial\gamma^{\mathrm{e}}_{3}}{\partial x_{2}} & -\dfrac{\partial\gamma^{\mathrm{e}}_{1}}{\partial x_{1}}+\dfrac{\partial\gamma^{\mathrm{e}}_{2}}{\partial x_{2}}\end{bmatrix} \tag{17}$$

For unloaded elastic-plastic condition, the elastic strain ε^{e} in the plastically deformed crystal will mostly disappear when the applied macroscopic stress is completely removed, thus the residual orientation gradient $\tilde{\boldsymbol{\kappa}}$ in this case only results from GND induced by plastic incompatibility, as shown in Fig. A1c. The contribution of edge components $b^{\mathrm{e}}_{ij}(i\neq j)$ and screw components $b^{\mathrm{s}}_{ij}(i=j)$ in GND density tensor $\boldsymbol{\rho}_{\mathrm{GND}}$ to orientation gradient components is shown in Eq. (18):

$$\boldsymbol{\varepsilon}^{\mathrm{e}}\approx 0,\ \tilde{\boldsymbol{\kappa}}=\frac{1}{2}(\boldsymbol{\rho}_{\mathrm{GND}}:\mathbf{I})\mathbf{I}-\boldsymbol{\rho}^{\mathrm{T}}_{\mathrm{GND}}=\begin{bmatrix}\dfrac{b^{\mathrm{s}}_{22}+b^{\mathrm{s}}_{33}-b^{\mathrm{s}}_{11}}{2} & -b^{\mathrm{e}}_{21} & -b^{\mathrm{e}}_{31}\\ -b^{\mathrm{e}}_{12} & \dfrac{b^{\mathrm{s}}_{33}+b^{\mathrm{s}}_{11}-b^{\mathrm{s}}_{22}}{2} & -b^{\mathrm{e}}_{32}\\ -b^{\mathrm{e}}_{13} & -b^{\mathrm{e}}_{23} & \dfrac{b^{\mathrm{s}}_{11}+b^{\mathrm{s}}_{22}-b^{\mathrm{s}}_{33}}{2}\end{bmatrix} \tag{18}$$

Accompanied by removing the elastic lattice strain ε^{e} from elastic distortion tensor $\boldsymbol{\beta}^{\mathrm{e}}$, one part of the lattice rotation item disappears at the same time, while the residual inhomogeneous part $\tilde{\boldsymbol{\Omega}}_{\mathrm{lattice}}$ is non-unloadable due to the existence of GND induced by plastic incompatibility. Thus the residual material distortion $\tilde{\boldsymbol{\beta}}$ consists of residual lattice rotation $\tilde{\boldsymbol{\Omega}}_{\mathrm{lattice}}$, non-lattice rotation $\boldsymbol{\Omega}_{\mathrm{non-lattice}}$ and plastic strain ε^{p} as shown in Eq. (19). The first two items make up the material rotation $\boldsymbol{\Omega}_{\mathrm{material}}$.

$$\tilde{\boldsymbol{\beta}}=\tilde{\boldsymbol{\Omega}}_{\mathrm{lattice}}+\boldsymbol{\beta}^{\mathrm{p}}=\tilde{\boldsymbol{\Omega}}_{\mathrm{lattice}}+\boldsymbol{\Omega}_{\mathrm{non-lattice}}+\boldsymbol{\varepsilon}^{\mathrm{p}}=\boldsymbol{\Omega}_{\mathrm{material}}+\boldsymbol{\varepsilon}^{\mathrm{p}},\ \ \boldsymbol{\rho}_{\mathrm{GND}}=\tilde{\boldsymbol{\Omega}}_{\mathrm{lattice}}\times\nabla \tag{19}$$

It should be noted that the elastic strain ε^{e} cannot be completely released in most practical situations, especially in PC samples where the grain boundaries' constraint is not negligible. However, we still suggest this approximation in the present work especially for those commercial EBSD users due to the following three reasons. Firstly, extracting the small unreleased elastic strain ε^{e} from Kikuchi patterns in the presence of large residual lattice rotation $\tilde{\boldsymbol{\Omega}}_{\mathrm{lattice}}$ needs the cross-correlation

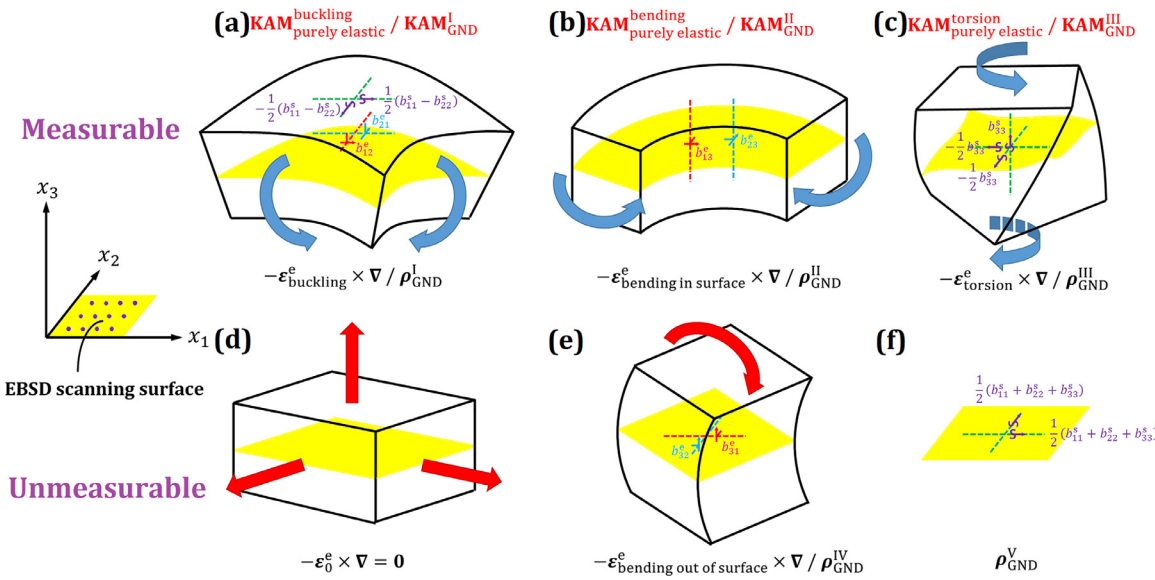

Fig. 2. (a) elastic buckling & the first sub-GND density tensor $\boldsymbol{\rho}^{\mathrm{I}}_{\mathrm{GND}}$, (b) elastic bending in surface & the second sub-GND density tensor $\boldsymbol{\rho}^{\mathrm{II}}_{\mathrm{GND}}$, (c) elastic torsion & the third sub-GND density tensor $\boldsymbol{\rho}^{\mathrm{III}}_{\mathrm{GND}}$, (d) elastic strain mode without curl, (e) elastic bending out of surface & the fourth sub-GND density tensor $\boldsymbol{\rho}^{\mathrm{IV}}_{\mathrm{GND}}$, and (f) the fifth sub-GND density tensor $\boldsymbol{\rho}^{\mathrm{V}}_{\mathrm{GND}}$.

based HR EBSD technique (Britton and Wilkinson, 2012), rather than the conventional Hough-transform based commercial EBSD equipment. Secondly, the unreleased elastic strain ε^{e} indeed becomes negligible compared with residual lattice rotation $\tilde{\boldsymbol{\Omega}}_{\mathrm{lattice}}$ (Jiang et al., 2016) under unloaded elastic-plastic condition, and the contribution of its curl $\varepsilon^{\mathrm{e}} \times \nabla$ to the lattice curvature $\tilde{\boldsymbol{\kappa}}$ only leads to very small changes in the estimation of GND density even in the PC samples (Wilkinson and Randman, 2010) according to the HR EBSD measurement results. Thirdly, the assumption that GND tends to arrange in constellations of lowest energy can be made to minimize the unreleased elastic strain ε^{e} in the plastically deformed crystalline materials (Konijnenberg et al., 2015).

3.2. Mechanism of *KAM* on characterizing elastic strain modes and GND density tensor invariants

According to the Eq. (10) shown in the above Section 2.2.1, **KAM** can be rewritten as the average projection of orientation gradient tensor $\boldsymbol{\kappa}$ along two axes $a\vec{\boldsymbol{e}}_1$ and $a\vec{\boldsymbol{e}}_2$ in the EBSD observational surface. However, there are two disadvantages to the current definition of **KAM**. Firstly, **KAM** is an non-objective parameter whose value will change with the rotation of 2D coordinate system ($\vec{\boldsymbol{e}}_1$ is the EBSD scanning direction and $\vec{\boldsymbol{e}}_2$ is the normal direction) located in the EBSD observational surface, because it is not the in-surface invariant of any tensors (Nye's tensor $\boldsymbol{\kappa}$ or $\tilde{\boldsymbol{\kappa}}$, GND density tensor $\boldsymbol{\rho}_{\mathrm{GND}}$ and the curl of elastic strain tensor $\varepsilon^{\mathrm{e}} \times \nabla$) independent of the axes $\vec{\boldsymbol{e}}_1$ and $\vec{\boldsymbol{e}}_2$. Secondly, the contributions of elastic strain components and GND density tensor components to the orientation gradient components have been revealed in the Eqs. (17) and (18) respectively, but the contributions of each elastic strain mode and each GND density tensor invariant to the **KAM** generated from orientation gradient tensor $\boldsymbol{\kappa}$ are still unrevealed. Thus an objective $\mathbf{KAM}^{\mathrm{obj}}$ will be redefined based on three independent sub-parameters, which accordingly correspond to three elastic strain modes in purely elastic condition and three GND density tensor invariants in unloaded elastic-plastic condition.

For purely elastic condition, the elastic strain curl $\varepsilon^{\mathrm{e}} \times \nabla$ can be additively decomposed into five items: $\boldsymbol{\varepsilon}^{\mathrm{e}}_{\mathrm{buckling}} \times \nabla$, $\boldsymbol{\varepsilon}^{\mathrm{e}}_{\mathrm{bending\ in\ suface}} \times \nabla$, $\boldsymbol{\varepsilon}^{\mathrm{e}}_{\mathrm{torsion}} \times \nabla$, $\boldsymbol{\varepsilon}^{\mathrm{e}}_{\mathrm{bending\ out\ of\ surface}} \times \nabla$ and $\boldsymbol{\varepsilon}^{\mathrm{e}}_{0} \times \nabla = 0$ as shown in Eq. (20) and schematically depicted in Fig. 2, which represent five elastic strain modes respectively when the observational surface (out of surface direction: $\vec{\boldsymbol{e}}_3$) is determined. The first four elastic strain items are of none-zero curl, which correspond to the strain modes of buckling, bending in surface, torsion and bending out of surface respectively, as shown in Fig. 2a, b, c and e. The last elastic strain item is of zero curl, which does not contribute to the lattice curvature, as shown in Fig. 2d.

$$\boldsymbol{\varepsilon}^{\mathrm{e}} \times \nabla = \boldsymbol{\varepsilon}^{\mathrm{e}}_{\mathrm{buckling}} \times \nabla + \boldsymbol{\varepsilon}^{\mathrm{e}}_{\mathrm{bending\ in\ suface}} \times \nabla + \boldsymbol{\varepsilon}^{\mathrm{e}}_{\mathrm{torsion}} \times \nabla + \boldsymbol{\varepsilon}^{\mathrm{e}}_{\mathrm{bending\ out\ of\ surface}} \times \nabla + \boldsymbol{\varepsilon}^{\mathrm{e}}_{0} \times \nabla \tag{20}$$

Accordingly, the orientation gradient tensor $\boldsymbol{\kappa}$ can also be additively decomposed into five items: $\boldsymbol{\kappa}_{\mathrm{I}}$, $\boldsymbol{\kappa}_{\mathrm{II}}$, $\boldsymbol{\kappa}_{\mathrm{III}}$, $\boldsymbol{\kappa}_{\mathrm{IV}}$ and $\boldsymbol{\kappa}_{\mathrm{V}} = 0$ as shown in Eq. (21), which correspond to lattice curvatures induced by elastic strain modes of buckling, bending in surface, torsion and bending out of surface respectively. Due to the extra constraint $\boldsymbol{\kappa} : \mathbf{I} = 0$ under the purely elastic

condition (see the details in Eq. (A8) in Appendix II), $-(\partial\theta_1/\partial x_1+\partial\theta_2/\partial x_2)$ is identically equal to $\partial\theta_3/\partial x_3$ in the $\boldsymbol{\kappa}_{\mathrm{III}}$ item.

$$\boldsymbol{\kappa}=\overbrace{\begin{bmatrix}\frac{1}{2}\left(\frac{\partial\theta_1}{\partial x_1}-\frac{\partial\theta_2}{\partial x_2}\right) & \frac{\partial\theta_1}{\partial x_2} & 0\\ \frac{\partial\theta_2}{\partial x_1} & -\frac{1}{2}\left(\frac{\partial\theta_1}{\partial x_1}-\frac{\partial\theta_2}{\partial x_2}\right) & 0\\ 0 & 0 & 0\end{bmatrix}}^{\boldsymbol{\kappa}_{\mathrm{I}}}+\overbrace{\begin{bmatrix}0 & 0 & 0\\ 0 & 0 & 0\\ \frac{\partial\theta_3}{\partial x_1} & \frac{\partial\theta_3}{\partial x_2} & 0\end{bmatrix}}^{\boldsymbol{\kappa}_{\mathrm{II}}}+\overbrace{\begin{bmatrix}\frac{1}{2}\left(\frac{\partial\theta_1}{\partial x_1}+\frac{\partial\theta_2}{\partial x_2}\right) & 0 & 0\\ 0 & \frac{1}{2}\left(\frac{\partial\theta_1}{\partial x_1}+\frac{\partial\theta_2}{\partial x_2}\right) & 0\\ 0 & 0 & \overbrace{-\left(\frac{\partial\theta_1}{\partial x_1}+\frac{\partial\theta_2}{\partial x_2}\right)}^{=\frac{\partial\theta_3}{\partial x_3}}\end{bmatrix}}^{\boldsymbol{\kappa}_{\mathrm{III}}}+\overbrace{\begin{bmatrix}0 & 0 & \frac{\partial\theta_1}{\partial x_3}\\ 0 & 0 & \frac{\partial\theta_2}{\partial x_3}\\ 0 & 0 & 0\end{bmatrix}}^{\boldsymbol{\kappa}_{\mathrm{IV}}}+\overbrace{\mathbf{0}}^{\boldsymbol{\kappa}_{\mathrm{IV}}} \tag{21}$$

Here the first item Eq. (22) represents elastic buckling of the observational surface, as shown in Fig. 2a.

$$\begin{aligned}\boldsymbol{\varepsilon}^{\mathrm{e}}_{\mathrm{buckling}}\times\nabla&=\begin{bmatrix}-\frac{1}{2}\left(\frac{\partial\gamma_1^{\mathrm{e}}}{\partial x_1}+\frac{\partial\gamma_2^{\mathrm{e}}}{\partial x_2}-2\frac{\partial\gamma_3^{\mathrm{e}}}{\partial x_3}\right) & -\frac{\partial\varepsilon_1^{\mathrm{e}}}{\partial x_3}+\frac{\partial\gamma_2^{\mathrm{e}}}{\partial x_1} & 0\\ \frac{\partial\varepsilon_2^{\mathrm{e}}}{\partial x_3}-\frac{\partial\gamma_1^{\mathrm{e}}}{\partial x_2} & \frac{1}{2}\left(\frac{\partial\gamma_1^{\mathrm{e}}}{\partial x_1}+\frac{\partial\gamma_2^{\mathrm{e}}}{\partial x_2}-2\frac{\partial\gamma_3^{\mathrm{e}}}{\partial x_3}\right) & 0\\ 0 & 0 & 0\end{bmatrix}=\boldsymbol{\kappa}_{\mathrm{I}}^{\mathrm{T}}=\begin{bmatrix}\frac{1}{2}\left(\frac{\partial\theta_1}{\partial x_1}-\frac{\partial\theta_2}{\partial x_2}\right) & \frac{\partial\theta_2}{\partial x_1} & 0\\ \frac{\partial\theta_1}{\partial x_2} & -\frac{1}{2}\left(\frac{\partial\theta_1}{\partial x_1}-\frac{\partial\theta_2}{\partial x_2}\right) & 0\\ 0 & 0 & 0\end{bmatrix}\\&=(\boldsymbol{\varepsilon}^{\mathrm{e}}\times\nabla)-\vec{\boldsymbol{e}}_3\vec{\boldsymbol{e}}_3\cdot(\boldsymbol{\varepsilon}^{\mathrm{e}}\times\nabla)-(\boldsymbol{\varepsilon}^{\mathrm{e}}\times\nabla)\cdot\vec{\boldsymbol{e}}_3\vec{\boldsymbol{e}}_3+2\vec{\boldsymbol{e}}_3\vec{\boldsymbol{e}}_3\cdot(\boldsymbol{\varepsilon}^{\mathrm{e}}\times\nabla)\cdot\vec{\boldsymbol{e}}_3\vec{\boldsymbol{e}}_3+\frac{1}{2}[(\boldsymbol{\varepsilon}^{\mathrm{e}}\times\nabla):\vec{\boldsymbol{e}}_3\vec{\boldsymbol{e}}_3](\mathbf{I}-3\vec{\boldsymbol{e}}_3\vec{\boldsymbol{e}}_3)\end{aligned} \tag{22}$$

The second item Eq. (23) represents elastic bending in the observational surface, as shown in Fig. 2b.

$$\boldsymbol{\varepsilon}^{\mathrm{e}}_{\text{bending in suface}}\times\nabla=\begin{bmatrix}0 & 0 & \frac{\partial\varepsilon_1^{\mathrm{e}}}{\partial x_2}-\frac{\partial\gamma_3^{\mathrm{e}}}{\partial x_1}\\ 0 & 0 & -\frac{\partial\varepsilon_2^{\mathrm{e}}}{\partial x_1}+\frac{\partial\gamma_3^{\mathrm{e}}}{\partial x_2}\\ 0 & 0 & 0\end{bmatrix}=\boldsymbol{\kappa}_{\mathrm{II}}^{\mathrm{T}}=\begin{bmatrix}0 & 0 & \frac{\partial\theta_3}{\partial x_1}\\ 0 & 0 & \frac{\partial\theta_3}{\partial x_2}\\ 0 & 0 & 0\end{bmatrix}=(\mathbf{I}-\vec{\boldsymbol{e}}_3\vec{\boldsymbol{e}}_3)\cdot(\boldsymbol{\varepsilon}^{\mathrm{e}}\times\nabla)\cdot\vec{\boldsymbol{e}}_3\vec{\boldsymbol{e}}_3 \tag{23}$$

The third item Eq. (24) represents elastic torsion of the observational surface, as shown in Fig. 2c.

$$\begin{aligned}\boldsymbol{\varepsilon}^{\mathrm{e}}_{\mathrm{torsion}}\times\nabla&=\begin{bmatrix}-\frac{1}{2}\left(-\frac{\partial\gamma_1^{\mathrm{e}}}{\partial x_1}+\frac{\partial\gamma_2^{\mathrm{e}}}{\partial x_2}\right) & 0 & 0\\ 0 & -\frac{1}{2}\left(-\frac{\partial\gamma_1^{\mathrm{e}}}{\partial x_1}+\frac{\partial\gamma_2^{\mathrm{e}}}{\partial x_2}\right) & 0\\ 0 & 0 & -\frac{\partial\gamma_1^{\mathrm{e}}}{\partial x_1}+\frac{\partial\gamma_2^{\mathrm{e}}}{\partial x_2}\end{bmatrix}\\&=\boldsymbol{\kappa}_{\mathrm{III}}^{\mathrm{T}}=\begin{bmatrix}\frac{1}{2}\left(\frac{\partial\theta_1}{\partial x_1}+\frac{\partial\theta_2}{\partial x_2}\right) & 0 & 0\\ 0 & \frac{1}{2}\left(\frac{\partial\theta_1}{\partial x_1}+\frac{\partial\theta_2}{\partial x_2}\right) & 0\\ 0 & 0 & -\left(\frac{\partial\theta_1}{\partial x_1}+\frac{\partial\theta_2}{\partial x_2}\right)\end{bmatrix}\\&=-\frac{1}{2}[(\boldsymbol{\varepsilon}^{\mathrm{e}}\times\nabla):\vec{\boldsymbol{e}}_3\vec{\boldsymbol{e}}_3](\mathbf{I}-3\vec{\boldsymbol{e}}_3\vec{\boldsymbol{e}}_3)\end{aligned} \tag{24}$$

The fourth item Eq. (25) represents elastic bending out of observational surface, as shown in Fig. 2e.

$$\boldsymbol{\varepsilon}^{\mathrm{e}}_{\text{bending out of surface}}\times\nabla=\begin{bmatrix}0 & 0 & 0\\ 0 & 0 & 0\\ -\frac{\partial\varepsilon_3^{\mathrm{e}}}{\partial x_2}+\frac{\partial\gamma_1^{\mathrm{e}}}{\partial x_3} & \frac{\partial\varepsilon_3^{\mathrm{e}}}{\partial x_1}-\frac{\partial\gamma_2^{\mathrm{e}}}{\partial x_3} & 0\end{bmatrix}=\boldsymbol{\kappa}_{\mathrm{IV}}^{\mathrm{T}}=\begin{bmatrix}0 & 0 & 0\\ 0 & 0 & 0\\ \frac{\partial\theta_1}{\partial x_3} & \frac{\partial\theta_2}{\partial x_3} & 0\end{bmatrix}=\vec{\boldsymbol{e}}_3\vec{\boldsymbol{e}}_3\cdot(\boldsymbol{\varepsilon}^{\mathrm{e}}\times\nabla)\cdot(\mathbf{I}-\vec{\boldsymbol{e}}_3\vec{\boldsymbol{e}}_3) \tag{25}$$

And the last item Eq. (26) represents elastic strain mode $\boldsymbol{\varepsilon}_0^{\mathrm{e}}$ without curl as shown in Fig. 2d, where $\psi(x_1, x_2, x_3)$ is a two-order differentiable function.

$$\varepsilon_0^{\mathrm{e}}\times\nabla=\boldsymbol{\kappa}_{\mathrm{V}}^{\mathrm{T}}=0,\quad \varepsilon_0^{e}(x_1,x_2,x_3)=\begin{bmatrix}\frac{\partial^2\psi(x_1,x_2,x_3)}{\partial x_1^2} & \frac{\partial^2\psi(x_1,x_2,x_3)}{\partial x_1\partial x_2} & \frac{\partial^2\psi(x_1,x_2,x_3)}{\partial x_1\partial x_3}\\ \frac{\partial^2\psi(x_1,x_2,x_3)}{\partial x_2\partial x_1} & \frac{\partial^2\psi(x_1,x_2,x_3)}{\partial x_2^2} & \frac{\partial^2\psi(x_1,x_2,x_3)}{\partial x_2\partial x_3}\\ \frac{\partial^2\psi(x_1,x_2,x_3)}{\partial x_3\partial x_1} & \frac{\partial^2\psi(x_1,x_2,x_3)}{\partial x_3\partial x_2} & \frac{\partial^2\psi(x_1,x_2,x_3)}{\partial x_3^2}\end{bmatrix} \tag{26}$$

The above additive decomposition operation on elastic strain curl $\varepsilon^{\mathrm{e}}\times\nabla$ shown in the formulas Eqs. (22)–(26) only involves the target tensor itself $\varepsilon^{\mathrm{e}}\times\nabla$, the metric tensor $\mathbf{I}$, and the component $\vec{\boldsymbol{e}}_3\vec{\boldsymbol{e}}_3$ of metric tensor $\mathbf{I}$ only related to the axis $\vec{\boldsymbol{e}}_3$ out

of the EBSD observational surface. Thus, the final decomposition result is independent of the axes $\vec{\boldsymbol{e}}_1$ and $\vec{\boldsymbol{e}}_2$ in the EBSD observational surface.

For the unloaded elastic-plastic condition, the GND density tensor $\boldsymbol{\rho}_{\mathrm{GND}}$ can be additively decomposed into five items: $\boldsymbol{\rho}^{\mathrm{I}}_{\mathrm{GND}}$, $\boldsymbol{\rho}^{\mathrm{II}}_{\mathrm{GND}}$, $\boldsymbol{\rho}^{\mathrm{III}}_{\mathrm{GND}}$, $\boldsymbol{\rho}^{\mathrm{IV}}_{\mathrm{GND}}$ and $\boldsymbol{\rho}^{\mathrm{V}}_{\mathrm{GND}}$ as shown in Eq. (27). The first four sub-GND density tensor items cause the same lattice curvature effect as that induced by elastic strain modes of buckling, in-surface bending, torsion, and out-of-surface bending respectively as shown in Fig. 2a, b, c and e. The last sub-GND density tensor item causes the extra lattice curvature effect as shown in Fig. 2f, which does not correspond to any elastic strain modes.

$$\boldsymbol{\rho}_{\mathrm{GND}} = \boldsymbol{\rho}^{\mathrm{I}}_{\mathrm{GND}} + \boldsymbol{\rho}^{\mathrm{II}}_{\mathrm{GND}} + \boldsymbol{\rho}^{\mathrm{III}}_{\mathrm{GND}} + \boldsymbol{\rho}^{\mathrm{IV}}_{\mathrm{GND}} + \boldsymbol{\rho}^{\mathrm{V}}_{\mathrm{GND}} \tag{27}$$

Accordingly, the residual orientation gradient tensor $\tilde{\boldsymbol{\kappa}}$ can also be additively decomposed into five items: $\tilde{\boldsymbol{\kappa}}_{\mathrm{I}}$, $\tilde{\boldsymbol{\kappa}}_{\mathrm{II}}$, $\tilde{\boldsymbol{\kappa}}_{\mathrm{III}}$, $\tilde{\boldsymbol{\kappa}}_{\mathrm{IV}}$ and $\tilde{\boldsymbol{\kappa}}_{\mathrm{V}}$ as shown in Eq. (28), which correspond to lattice curvatures induced by the sub-GND density tensor items $\boldsymbol{\rho}^{\mathrm{I}}_{\mathrm{GND}}$, $\boldsymbol{\rho}^{\mathrm{II}}_{\mathrm{GND}}$, $\boldsymbol{\rho}^{\mathrm{III}}_{\mathrm{GND}}$, $\boldsymbol{\rho}^{\mathrm{IV}}_{\mathrm{GND}}$ and $\boldsymbol{\rho}^{\mathrm{V}}_{\mathrm{GND}}$ respectively. Here $\tilde{\boldsymbol{\kappa}}_{\mathrm{I}}$, $\tilde{\boldsymbol{\kappa}}_{\mathrm{II}}$, $\tilde{\boldsymbol{\kappa}}_{\mathrm{III}}$ and $\tilde{\boldsymbol{\kappa}}_{\mathrm{V}}$ has the same form with $\boldsymbol{\kappa}_{\mathrm{I}}$, $\boldsymbol{\kappa}_{\mathrm{II}}$, $\boldsymbol{\kappa}_{\mathrm{III}}$ and $\boldsymbol{\kappa}_{\mathrm{IV}}$ shown in Eq. (21). But it should be noted that $-(\partial\theta_1/\partial x_1 + \partial\theta_2/\partial x_2)$ is no longer equal to $\partial\theta_3/\partial x_3$ in the $\tilde{\boldsymbol{\kappa}}_{\mathrm{III}}$ item, and the $\tilde{\boldsymbol{\kappa}}_{\mathrm{V}}$ item is also no longer equal to $\mathbf{0}$ without the extra constraint $\tilde{\boldsymbol{\kappa}} : \mathbf{I} = 0$ under the unloaded elastic-plastic condition.

$$\tilde{\boldsymbol{\kappa}} = \tilde{\boldsymbol{\kappa}}_{\mathrm{I}} + \tilde{\boldsymbol{\kappa}}_{\mathrm{II}} + \overbrace{\begin{bmatrix} \frac{1}{2}\left(\frac{\partial\theta_1}{\partial x_1} + \frac{\partial\theta_2}{\partial x_2}\right) & 0 & 0 \\ 0 & \frac{1}{2}\left(\frac{\partial\theta_1}{\partial x_1} + \frac{\partial\theta_2}{\partial x_2}\right) & 0 \\ 0 & 0 & \overbrace{-\left(\frac{\partial\theta_1}{\partial x_1} + \frac{\partial\theta_2}{\partial x_2}\right)}^{\neq \frac{\partial\theta_3}{\partial x_3}} \end{bmatrix}}^{\tilde{\boldsymbol{\kappa}}_{\mathrm{III}}} + \tilde{\boldsymbol{\kappa}}_{\mathrm{IV}} + \overbrace{\begin{bmatrix} 0 & 0 & 0 \\ 0 & 0 & 0 \\ 0 & 0 & \frac{\partial\theta_1}{\partial x_1} + \frac{\partial\theta_2}{\partial x_2} + \frac{\partial\theta_3}{\partial x_3} \end{bmatrix}}^{\tilde{\boldsymbol{\kappa}}_{\mathrm{V}}} \tag{28}$$

Here the first item Eq. (29) causes the same lattice curvature effect as that induced by elastic buckling.

$$\begin{aligned} \boldsymbol{\rho}^{\mathrm{I}}_{\mathrm{GND}} &= \begin{bmatrix} \frac{b^{\mathrm{s}}_{11} - b^{\mathrm{s}}_{22}}{2} & b^{\mathrm{e}}_{12} & 0 \\ b^{\mathrm{e}}_{21} & -\frac{b^{\mathrm{s}}_{11} - b^{\mathrm{s}}_{22}}{2} & 0 \\ 0 & 0 & 0 \end{bmatrix} = (\tilde{\boldsymbol{\kappa}}_{\mathrm{I}} : \mathbf{I})\mathbf{I} - \tilde{\boldsymbol{\kappa}}_{\mathrm{I}}^{\mathrm{T}} = -\tilde{\boldsymbol{\kappa}}_{\mathrm{I}}^{\mathrm{T}} = \begin{bmatrix} -\frac{1}{2}\left(\frac{\partial\theta_1}{\partial x_1} - \frac{\partial\theta_2}{\partial x_2}\right) & -\frac{\partial\theta_2}{\partial x_1} & 0 \\ -\frac{\partial\theta_1}{\partial x_2} & \frac{1}{2}\left(\frac{\partial\theta_1}{\partial x_1} - \frac{\partial\theta_2}{\partial x_2}\right) & 0 \\ 0 & 0 & 0 \end{bmatrix} \\ &= \boldsymbol{\rho}_{\mathrm{GND}} - \vec{\boldsymbol{e}}_3\vec{\boldsymbol{e}}_3 \cdot \boldsymbol{\rho}_{\mathrm{GND}} - \boldsymbol{\rho}_{\mathrm{GND}} \cdot \vec{\boldsymbol{e}}_3\vec{\boldsymbol{e}}_3 + 2\vec{\boldsymbol{e}}_3\vec{\boldsymbol{e}}_3 \cdot \boldsymbol{\rho}_{\mathrm{GND}} \cdot \vec{\boldsymbol{e}}_3\vec{\boldsymbol{e}}_3 + \frac{1}{2}[\boldsymbol{\rho}_{\mathrm{GND}} : \vec{\boldsymbol{e}}_3\vec{\boldsymbol{e}}_3](\mathbf{I} - 3\vec{\boldsymbol{e}}_3\vec{\boldsymbol{e}}_3) \\ &\quad - \frac{1}{2}(\boldsymbol{\rho}_{\mathrm{GND}} : \mathbf{I})(\mathbf{I} - \vec{\boldsymbol{e}}_3\vec{\boldsymbol{e}}_3) \end{aligned} \tag{29}$$

the second item Eq. (30) causes the same lattice curvature effect as that induced by in-surface elastic bending.

$$\boldsymbol{\rho}^{\mathrm{II}}_{\mathrm{GND}} = \begin{bmatrix} 0 & 0 & b^{\mathrm{e}}_{13} \\ 0 & 0 & b^{\mathrm{e}}_{23} \\ 0 & 0 & 0 \end{bmatrix} = (\tilde{\boldsymbol{\kappa}}_{\mathrm{II}} : \mathbf{I})\mathbf{I} - \tilde{\boldsymbol{\kappa}}_{\mathrm{II}}^{\mathrm{T}} = -\tilde{\boldsymbol{\kappa}}_{\mathrm{II}}^{\mathrm{T}} = \begin{bmatrix} 0 & 0 & -\frac{\partial\theta_3}{\partial x_1} \\ 0 & 0 & -\frac{\partial\theta_3}{\partial x_2} \\ 0 & 0 & 0 \end{bmatrix} = (\mathbf{I} - \vec{\boldsymbol{e}}_3\vec{\boldsymbol{e}}_3) \cdot \boldsymbol{\rho}_{\mathrm{GND}} \cdot \vec{\boldsymbol{e}}_3\vec{\boldsymbol{e}}_3 \tag{30}$$

The third item Eq. (31) causes the same lattice curvature effect as that induced by elastic torsion.

$$\begin{aligned} \boldsymbol{\rho}^{\mathrm{III}}_{\mathrm{GND}} &= \begin{bmatrix} -\frac{1}{2}b^{\mathrm{s}}_{33} & 0 & 0 \\ 0 & -\frac{1}{2}b^{\mathrm{s}}_{33} & 0 \\ 0 & 0 & b^{\mathrm{s}}_{33} \end{bmatrix} = (\tilde{\boldsymbol{\kappa}}_{\mathrm{III}} : \mathbf{I})\mathbf{I} - \tilde{\boldsymbol{\kappa}}_{\mathrm{III}}^{\mathrm{T}} = -\tilde{\boldsymbol{\kappa}}_{\mathrm{III}}^{\mathrm{T}} = \begin{bmatrix} -\frac{1}{2}\left(\frac{\partial\theta_1}{\partial x_1} + \frac{\partial\theta_2}{\partial x_2}\right) & 0 & 0 \\ 0 & -\frac{1}{2}\left(\frac{\partial\theta_1}{\partial x_1} + \frac{\partial\theta_2}{\partial x_2}\right) & 0 \\ 0 & 0 & \frac{\partial\theta_1}{\partial x_1} + \frac{\partial\theta_2}{\partial x_2} \end{bmatrix} \\ &= -\frac{1}{2}[\boldsymbol{\rho}_{\mathrm{GND}} : \vec{\boldsymbol{e}}_3\vec{\boldsymbol{e}}_3](\mathbf{I} - 3\vec{\boldsymbol{e}}_3\vec{\boldsymbol{e}}_3) \end{aligned} \tag{31}$$

The fourth item Eq. (32) causes the same lattice curvature effect as that induced by out-of-surface elastic bending.

$$\boldsymbol{\rho}^{\mathrm{IV}}_{\mathrm{GND}} = \begin{bmatrix} 0 & 0 & 0 \\ 0 & 0 & 0 \\ b^{\mathrm{e}}_{31} & b^{\mathrm{e}}_{32} & 0 \end{bmatrix} = (\tilde{\boldsymbol{\kappa}}_{\mathrm{IV}} : \mathbf{I})\mathbf{I} - \tilde{\boldsymbol{\kappa}}_{\mathrm{IV}}^{\mathrm{T}} = -\tilde{\boldsymbol{\kappa}}_{\mathrm{IV}}^{\mathrm{T}} = \begin{bmatrix} 0 & 0 & 0 \\ 0 & 0 & 0 \\ -\frac{\partial\theta_1}{\partial x_3} & -\frac{\partial\theta_2}{\partial x_3} & 0 \end{bmatrix} = \vec{\boldsymbol{e}}_3\vec{\boldsymbol{e}}_3 \cdot \boldsymbol{\rho}_{\mathrm{GND}} \cdot (\mathbf{I} - \vec{\boldsymbol{e}}_3\vec{\boldsymbol{e}}_3) \tag{32}$$

And the last item Eq. (33) reflects the extra contribution of remaining GND screw components to the orientation gradient not corresponding to any elastic strain modes, as shown in Fig. 2f.

$$\begin{aligned} \boldsymbol{\rho}^{\mathrm{V}}_{\mathrm{GND}} &= \begin{bmatrix} \frac{b^{\mathrm{s}}_{11} + b^{\mathrm{s}}_{22} + b^{\mathrm{s}}_{33}}{2} & 0 & 0 \\ 0 & \frac{b^{\mathrm{s}}_{11} + b^{\mathrm{s}}_{22} + b^{\mathrm{s}}_{33}}{2} & 0 \\ 0 & 0 & 0 \end{bmatrix} = (\tilde{\boldsymbol{\kappa}}_{\mathrm{V}} : \mathbf{I})\mathbf{I} - \tilde{\boldsymbol{\kappa}}_{\mathrm{V}}^{\mathrm{T}} = \begin{bmatrix} \frac{\partial\theta_1}{\partial x_1} + \frac{\partial\theta_2}{\partial x_2} + \frac{\partial\theta_3}{\partial x_3} & 0 & 0 \\ 0 & \frac{\partial\theta_1}{\partial x_1} + \frac{\partial\theta_2}{\partial x_2} + \frac{\partial\theta_3}{\partial x_3} & 0 \\ 0 & 0 & 0 \end{bmatrix} \\ &= \frac{1}{2}(\boldsymbol{\rho}_{\mathrm{GND}} : \mathbf{I})(\mathbf{I} - \vec{\boldsymbol{e}}_3\vec{\boldsymbol{e}}_3) \end{aligned} \tag{33}$$

Similar with the above additive decomposition operation on elastic strain curl $\varepsilon^{e} \times \nabla$, the decomposition operation on GND density tensor $\boldsymbol{\rho}_{GND}$ shown in the formulas Eqs. (29)–(33) is also independent of the axes $\vec{\boldsymbol{e}}_1$ and $\vec{\boldsymbol{e}}_2$ in the EBSD observational surface, and only relies on the axis $\vec{\boldsymbol{e}}_3$ out of the EBSD observational surface. Therefore, the double multiplication between each sub-GND density tensor item and itself will generate the in-surface invariant of GND density tensor $\boldsymbol{\rho}_{GND}$ independent of the two axes $\vec{\boldsymbol{e}}_1$ and $\vec{\boldsymbol{e}}_2$ in the EBSD observational surface, such as $\rho^{I}_{GND} = \sqrt{\boldsymbol{\rho}^{I}_{GND} : \boldsymbol{\rho}^{I}_{GND}}$, $\rho^{II}_{GND} = \sqrt{\boldsymbol{\rho}^{II}_{GND} : \boldsymbol{\rho}^{II}_{GND}}$, $\rho^{III}_{GND} = \sqrt{\boldsymbol{\rho}^{III}_{GND} : \boldsymbol{\rho}^{III}_{GND}}$. $\rho^{IV}_{GND} = \sqrt{\boldsymbol{\rho}^{IV}_{GND} : \boldsymbol{\rho}^{IV}_{GND}}$ and $\rho^{V}_{GND} = \sqrt{\boldsymbol{\rho}^{V}_{GND} : \boldsymbol{\rho}^{V}_{GND}}$.

Based on the above decomposition operation on elastic strain curl $\varepsilon^{e} \times \nabla$ and GND density tensor $\boldsymbol{\rho}_{GND}$, we can propose several sub-parameters at first to characterize each elastic strain mode and each GND density tensor invariant respectively. $\mathbf{KAM}^{buckling}_{purely\ elastic}$ representing the degree of elastic buckling $\boldsymbol{\varepsilon}^{e}_{buckling} \times \nabla$ and $\mathbf{KAM}^{I}_{GND}$ representing the first in-surface invariant ρ^{I}_{GND} of GND density tensor cause the indistinguishable lattice curvature effect as shown in Fig. 2a and Eq. (34):

$$\begin{aligned}
&\mathbf{KAM}^{buckling}_{purely\ elastic} \overset{def}{=} \sqrt{\left(\boldsymbol{\varepsilon}^{e}_{buckling} \times \nabla\right) : \left(\boldsymbol{\varepsilon}^{e}_{buckling} \times \nabla\right)} = \sqrt{\boldsymbol{\kappa}_{I} : \boldsymbol{\kappa}_{I}} \\
&\Leftrightarrow \mathbf{KAM}^{I}_{GND} \overset{def}{=} \sqrt{\boldsymbol{\rho}^{I}_{GND} : \boldsymbol{\rho}^{I}_{GND}} = \sqrt{\tilde{\boldsymbol{\kappa}}_{I} : \tilde{\boldsymbol{\kappa}}_{I}} = \lim_{a \to 0} \sqrt{\left(\frac{\theta_{12}}{a}\right)^2 + \left(\frac{\theta_{21}}{a}\right)^2 + \frac{1}{2}\left(\frac{\theta_{11}}{a} - \frac{\theta_{22}}{a}\right)^2}
\end{aligned} \tag{34}$$

$\mathbf{KAM}^{bending}_{purely\ elastic}$ representing the degree of in-surface elastic bending $\boldsymbol{\varepsilon}^{e}_{bending} \times \nabla$ and $\mathbf{KAM}^{II}_{GND}$ representing the second in-surface invariant ρ^{II}_{GND} of GND density tensor cause the indistinguishable lattice curvature effect as shown in Fig. 2b and Eq. (35):

$$\begin{aligned}
&\mathbf{KAM}^{bending}_{purely\ elastic} \overset{def}{=} \sqrt{\left(\boldsymbol{\varepsilon}^{e}_{bending\ in\ suface} \times \nabla\right) : \left(\boldsymbol{\varepsilon}^{e}_{bending\ in\ suface} \times \nabla\right)} = \sqrt{\boldsymbol{\kappa}_{II} : \boldsymbol{\kappa}_{II}} \\
&\Leftrightarrow \mathbf{KAM}^{II}_{GND} \overset{def}{=} \sqrt{\boldsymbol{\rho}^{II}_{GND} : \boldsymbol{\rho}^{II}_{GND}} = \sqrt{\tilde{\boldsymbol{\kappa}}_{II} : \tilde{\boldsymbol{\kappa}}_{II}} = \lim_{a \to 0} \sqrt{\left(\frac{\theta_{13}}{a}\right)^2 + \left(\frac{\theta_{23}}{a}\right)^2}
\end{aligned} \tag{35}$$

$\mathbf{KAM}^{torsion}_{purely\ elastic}$ representing the degree of elastic torsion $\boldsymbol{\varepsilon}^{e}_{bending} \times \nabla$ and $\mathbf{KAM}^{III}_{GND}$ representing the third in-surface invariant ρ^{III}_{GND} of GND density tensor cause the indistinguishable lattice curvature effect as shown in Fig. 2c and Eq. (36):

$$\begin{aligned}
&\mathbf{KAM}^{torsion}_{purely\ elastic} \overset{def}{=} \sqrt{\frac{1}{3}\left(\boldsymbol{\varepsilon}^{e}_{torsion} \times \nabla\right) : \left(\boldsymbol{\varepsilon}^{e}_{torsion} \times \nabla\right)} = \sqrt{\frac{1}{3}\boldsymbol{\kappa}_{III} : \boldsymbol{\kappa}_{III}} \\
&\Leftrightarrow \mathbf{KAM}^{III}_{GND} \overset{def}{=} \sqrt{\frac{1}{3}\boldsymbol{\rho}^{III}_{GND} : \boldsymbol{\rho}^{III}_{GND}} = \sqrt{\frac{1}{3}\tilde{\boldsymbol{\kappa}}_{III} : \tilde{\boldsymbol{\kappa}}_{III}} = \lim_{a \to 0} \frac{\sqrt{2}}{2}\left|\frac{\theta_{11}}{a} + \frac{\theta_{22}}{a}\right|
\end{aligned} \tag{36}$$

With respect to the elastic strain mode without curl $\boldsymbol{\varepsilon}^{e}_{0} \times \nabla = 0$ (Fig. 2d) and the out-of-surface elastic bending $\boldsymbol{\varepsilon}^{e}_{bending\ out\ of\ surface} \times \nabla$ (Fig. 2e), as well as the in-surface invariants ρ^{IV}_{GND} (Fig. 2e) and ρ^{V}_{GND} of GND density tensor (Fig. 2f), there are no suitable sub-parameters for their characterization because they do not cause any measurable orientation gradient in the 2D EBSD observational surface. Then we can redefine the new objective parameter $\mathbf{KAM}^{obj}$ based on the synthesis of the above measurable elastic strain modes and GND density tensor invariants as Eq. (37):

$$\begin{aligned}
&\left(\mathbf{KAM}^{obj}\right)^2 \xrightarrow{purely\ elastic} \left(\mathbf{KAM}^{buckling}_{purely\ elastic}\right)^2 + \left(\mathbf{KAM}^{bending}_{purely\ elastic}\right)^2 + \left(\mathbf{KAM}^{torsion}_{purely\ elastic}\right)^2 \\
&= \left(\boldsymbol{\varepsilon}^{e}_{buckling} \times \nabla\right) : \left(\boldsymbol{\varepsilon}^{e}_{buckling} \times \nabla\right) + \left(\boldsymbol{\varepsilon}^{e}_{bending\ in\ suface} \times \nabla\right) : \left(\boldsymbol{\varepsilon}^{e}_{bending\ in\ suface} \times \nabla\right) \\
&+ \frac{1}{3}\left(\boldsymbol{\varepsilon}^{e}_{torsion} \times \nabla\right) : \left(\boldsymbol{\varepsilon}^{e}_{torsion} \times \nabla\right) \\
&= \boldsymbol{\kappa}_{I} : \boldsymbol{\kappa}_{I} + \boldsymbol{\kappa}_{II} : \boldsymbol{\kappa}_{II} + \frac{1}{3}\boldsymbol{\kappa}_{III} : \boldsymbol{\kappa}_{III} = \left(\boldsymbol{\kappa} \cdot \vec{\boldsymbol{e}}_1\right)^2 + \left(\boldsymbol{\kappa} \cdot \vec{\boldsymbol{e}}_2\right)^2 = \boldsymbol{\kappa} : \boldsymbol{\kappa} - \left(\boldsymbol{\kappa} \cdot \vec{\boldsymbol{e}}_3\right)^2 \\
&\xrightarrow{elastic-plastic} \left(\mathbf{KAM}^{I}_{GND}\right)^2 + \left(\mathbf{KAM}^{II}_{GND}\right)^2 + \left(\mathbf{KAM}^{III}_{GND}\right)^2 = \boldsymbol{\rho}^{I}_{GND} : \boldsymbol{\rho}^{I}_{GND} + \boldsymbol{\rho}^{II}_{GND} : \boldsymbol{\rho}^{II}_{GND} + \frac{1}{3}\boldsymbol{\rho}^{III}_{GND} : \boldsymbol{\rho}^{III}_{GND} \\
&= \tilde{\boldsymbol{\kappa}}_{I} : \tilde{\boldsymbol{\kappa}}_{I} + \tilde{\boldsymbol{\kappa}}_{II} : \tilde{\boldsymbol{\kappa}}_{II} + \frac{1}{3}\tilde{\boldsymbol{\kappa}}_{III} : \tilde{\boldsymbol{\kappa}}_{III} = \left(\tilde{\boldsymbol{\kappa}} \cdot \vec{\boldsymbol{e}}_1\right)^2 + \left(\tilde{\boldsymbol{\kappa}} \cdot \vec{\boldsymbol{e}}_2\right)^2 = \tilde{\boldsymbol{\kappa}} : \tilde{\boldsymbol{\kappa}} - \left(\tilde{\boldsymbol{\kappa}} \cdot \vec{\boldsymbol{e}}_3\right)^2 \\
&= \lim_{a \to 0}\left[\left(\frac{\theta_{11}}{a}\right)^2 + \left(\frac{\theta_{12}}{a}\right)^2 + \left(\frac{\theta_{13}}{a}\right)^2 + \left(\frac{\theta_{21}}{a}\right)^2 + \left(\frac{\theta_{22}}{a}\right)^2 + \left(\frac{\theta_{23}}{a}\right)^2\right]
\end{aligned} \tag{37}$$

$\mathbf{KAM}^{obj}$ here contains all the 2D orientation gradient information induced by buckling, in-surface bending and torsion in purely elastic condition, as well as the in-surface invariants ρ^{I}_{GND}, ρ^{II}_{GND} and ρ^{III}_{GND} of GND density tensor $\boldsymbol{\rho}_{GND}$ in unloaded elastic-plastic condition. Compared with the original definition of **KAM** shown in Eqs. (9) and (10), $\mathbf{KAM}^{obj}$ will not change with the rotation of 2D coordinate system ($\vec{\boldsymbol{e}}_1$,$\vec{\boldsymbol{e}}_2$) in the EBSD observational surface and EBSD scanning step size a. However,

KAM is easier to be calculated in diffraction-based misorientation mapping, and serves as a qualitative description of $\mathbf{KAM}^{\mathrm{obj}}$ distribution without changing its physical essence when the 2D coordinate system $(\vec{\boldsymbol{e}}_1,\vec{\boldsymbol{e}}_2)$ and scanning step size a are determined, as shown in the following Eq. (38):

$$\mathbf{KAM} \overset{\mathrm{def}}{=} \frac{a}{2}|\boldsymbol{\kappa}\cdot\vec{\boldsymbol{e}}_1| + \frac{a}{2}|\boldsymbol{\kappa}\cdot\vec{\boldsymbol{e}}_2| = \frac{a}{2}\mathbf{KAM}^{\mathrm{obj}}(|\cos\vartheta| + |\sin\vartheta|) \sim \mathbf{KAM}^{\mathrm{obj}} \tag{38}$$

3.3. Mechanisms of *GROD* and *KAM* on characterizing in-plane plastic strain and material rotation

As the symmetric and antisymmetric parts of typical in-plane material distortion $\tilde{\boldsymbol{\beta}}$ under unloaded elastic-plastic condition, the in-plane plastic strain ε^{p} contains two independent components γ_3^{p}, ε^{p}(invariable volume : $\varepsilon_1^{\mathrm{p}} = -\varepsilon_2^{\mathrm{p}} = \varepsilon^{\mathrm{p}}$), while the in-plane material rotation $\boldsymbol{\Omega}_{\mathrm{material}}$ contains one independent component ω_3, as shown in Eq. (39). However, the residual lattice rotation $\tilde{\boldsymbol{\Omega}}_{\mathrm{lattice}}(\tilde{\boldsymbol{\beta}})$ still cannot be decoupled from the material rotation $\boldsymbol{\Omega}_{\mathrm{material}}(\tilde{\boldsymbol{\beta}})$ without the activated slip systems information, even if the material distortion $\tilde{\boldsymbol{\beta}}$ has been given in advance.

$$\tilde{\boldsymbol{\beta}} = \boldsymbol{\varepsilon}^{\mathrm{p}} + \boldsymbol{\Omega}_{\mathrm{material}} = \begin{bmatrix} \varepsilon_1^{\mathrm{p}} = \varepsilon^{\mathrm{p}} & \gamma_3^{\mathrm{p}} + \omega_3 \\ \gamma_3^{\mathrm{p}} - \omega_3 & \varepsilon_2^{\mathrm{p}} = -\varepsilon^{\mathrm{p}} \end{bmatrix} = \boldsymbol{\beta}^{\mathrm{p}}\left(\tilde{\boldsymbol{\beta}}\right) + \tilde{\boldsymbol{\Omega}}_{\mathrm{lattice}}\left(\tilde{\boldsymbol{\beta}}\right),\ \tilde{\boldsymbol{\Omega}}_{\mathrm{lattice}}\left(\tilde{\boldsymbol{\beta}}\right) = \begin{bmatrix} 0 & \theta_3 \\ -\theta_3 & 0 \end{bmatrix} \tag{39}$$

In the 2D case, at least two independent non-orthogonal slip systems $(\vec{\boldsymbol{s}}^1, \vec{\boldsymbol{n}}^1)$ and $(\vec{\boldsymbol{s}}^2, \vec{\boldsymbol{n}}^2)$ located in plane should be activated to undertake any status of in-plane plastic strain ε^{p} containing two independent components, and the plastic distortion tensor $\boldsymbol{\beta}^{\mathrm{p}}(\tilde{\boldsymbol{\beta}})$ is made up of the slip amounts γ_1 and γ_2 in the above two slip systems. If the azimuthal angle φ_α $(|\varphi_1 - \varphi_2| \neq \pi/2)$ between slip direction $\vec{\boldsymbol{s}}^\alpha$ and axis $\vec{\boldsymbol{e}}_1$ is given, the orientations of two slip systems can be determined completely. Then the dependence of residual lattice rotation angle θ_3 on plastic strain components ε^{p}, γ_3^{p} and material rotation component ω_3 can be obtained as shown in Eq. (40), which is influenced by azimuthal angles φ_1, φ_2 of activated slip systems. The detailed derivation process is given in the Appendix III.

$$\theta_3\left(\varepsilon^{\mathrm{p}}, \gamma_3^{\mathrm{p}}, \omega_3, \varphi_1, \varphi_2\right) = \omega_3 + \frac{\sin(\varphi_1+\varphi_2)}{\cos(\varphi_1-\varphi_2)}\varepsilon^{\mathrm{p}} - \frac{\cos(\varphi_1+\varphi_2)}{\cos(\varphi_1-\varphi_2)}\gamma_3^{\mathrm{p}} \tag{40}$$

Once the reference point is selected, the relative lattice rotation angle $\Delta\theta_3$, i.e. $\mathbf{GROD}(\tilde{\boldsymbol{\beta}})$ can be then expressed by the relative plastic strain components $\Delta\varepsilon^{\mathrm{p}}$, $\Delta\gamma_3^{\mathrm{p}}$ and the relative material rotation component $\Delta\omega_3$ as shown in Eq. (41), which also relies on azimuthal angles φ_1, φ_2 of two slip systems.

$$\mathbf{GROD}\left(\tilde{\boldsymbol{\beta}}\right) = |\theta_3 - \theta_{\mathrm{ref}}| = \left|(\omega_3 - \omega_{\mathrm{ref}}) + \frac{\sin(\varphi_1+\varphi_2)}{\cos(\varphi_1-\varphi_2)}\left(\varepsilon^{\mathrm{p}} - \varepsilon_{\mathrm{ref}}^{\mathrm{p}}\right) - \frac{\cos(\varphi_1+\varphi_2)}{\cos(\varphi_1-\varphi_2)}\left(\gamma_3^{\mathrm{p}} - \gamma_{\mathrm{ref}}^{\mathrm{p}}\right)\right| \tag{41}$$

GROD is the function of relative plastic strain $\Delta\varepsilon^{\mathrm{p}}$, $\Delta\gamma_3^{\mathrm{p}}$ and relative material rotation $\Delta\omega_3$, as well as azimuthal angles φ_1, φ_2 of two slip systems at the same time. Therefore, it corresponds to neither the local plastic strain ε^{p}, γ_3^{p} nor the local material rotation ω_3 alone in the in-plane deformed SC sample even if the $(\varepsilon_{\mathrm{ref}}^{\mathrm{p}}, \gamma_{\mathrm{ref}}^{\mathrm{p}}, \omega_{\mathrm{ref}})$ at the reference point is equal to zero, as reported in Refs. (Kamaya et al., 2007; Di Gioacchino and Quinta da Fonseca, 2015).

Further, the gradient of residual lattice rotation angle θ_3 along x_1 and x_2 axes can be expressed as Eq. (42), where the gradient of material rotation component ω_3 was replaced by $\partial\omega_3/\partial x_1 = \partial\varepsilon_1^{\mathrm{p}}/\partial x_2 - \partial\gamma_3^{\mathrm{p}}/\partial x_1$, $\partial\omega_3/\partial x_2 = -\partial\varepsilon_2^{\mathrm{p}}/\partial x_1 + \partial\gamma_3^{\mathrm{p}}/\partial x_2$ considering the compatibility of residual material distortion tensor $\tilde{\boldsymbol{\beta}}\times\nabla = 0$. It is obvious that the orientation gradient components relies on not only the plastic strain components gradient but also the azimuthal angles φ_1, φ_2 of slip systems.

$$\begin{bmatrix} \dfrac{\partial\theta_3}{\partial x_1} \\ \dfrac{\partial\theta_3}{\partial x_2} \end{bmatrix} = \begin{bmatrix} -\dfrac{\sin(\varphi_1+\varphi_2)}{\cos(\varphi_1-\varphi_2)} & 1 \\ -1 & \dfrac{\sin(\varphi_1+\varphi_2)}{\cos(\varphi_1-\varphi_2)} \end{bmatrix} \begin{bmatrix} \dfrac{\partial\varepsilon_2^{\mathrm{p}}}{\partial x_1} \\ \dfrac{\partial\varepsilon_1^{\mathrm{p}}}{\partial x_2} \end{bmatrix} + \begin{bmatrix} -\dfrac{2\cos\varphi_1\cos\varphi_2}{\cos(\varphi_1-\varphi_2)} & 0 \\ 0 & \dfrac{2\sin\varphi_1\sin\varphi_2}{\cos(\varphi_1-\varphi_2)} \end{bmatrix} \begin{bmatrix} \dfrac{\partial\gamma_3^{\mathrm{p}}}{\partial x_1} \\ \dfrac{\partial\gamma_3^{\mathrm{p}}}{\partial x_2} \end{bmatrix} \tag{42}$$

Then the average local orientation gradient $(\partial\theta_3/\partial x_1 + \partial\theta_3/\partial x_2)/2$, i.e. $\mathbf{KAM}(\varepsilon^{\mathrm{p}})$ can be expressed by the plastic strain components gradient $\partial\varepsilon_2^{\mathrm{p}}/\partial x_1$, $\partial\varepsilon_1^{\mathrm{p}}/\partial x_2$, $\partial\gamma_3^{\mathrm{p}}/\partial x_1$ and $\partial\gamma_3^{\mathrm{p}}/\partial x_2$ as shown in Eq. (43), which also relies on azimuthal angles φ_1, φ_2 of slip systems and EBSD step size a.

$$\mathbf{KAM}(\boldsymbol{\varepsilon}^{\mathrm{p}}) = \frac{a}{2}\left|\frac{\partial\varepsilon_1^{\mathrm{p}}}{\partial x_2} - \frac{\sin(\varphi_1+\varphi_2)}{\cos(\varphi_1-\varphi_2)}\frac{\partial\varepsilon_2^{\mathrm{p}}}{\partial x_1} - \frac{2\cos\varphi_1\cos\varphi_2}{\cos(\varphi_1-\varphi_2)}\frac{\partial\gamma_3^{\mathrm{p}}}{\partial x_1}\right| + \frac{a}{2}\left|\frac{\sin(\varphi_1+\varphi_2)}{\cos(\varphi_1-\varphi_2)}\frac{\partial\varepsilon_1^{\mathrm{p}}}{\partial x_2} - \frac{\partial\varepsilon_2^{\mathrm{p}}}{\partial x_1} + \frac{2\sin\varphi_1\sin\varphi_2}{\cos(\varphi_1-\varphi_2)}\frac{\partial\gamma_3^{\mathrm{p}}}{\partial x_2}\right| \tag{43}$$

KAM corresponds to the plastic strain gradient $\partial\varepsilon_2^{\mathrm{p}}/\partial x_1$, $\partial\varepsilon_1^{\mathrm{p}}/\partial x_2$, $\partial\gamma_3^{\mathrm{p}}/\partial x_1$ and $\partial\gamma_3^{\mathrm{p}}/\partial x_2$, rather than the local plastic strain ε^{p}, γ_3^{p} or the local material rotation ω_3 in the in-plane deformed SC sample.

The $\boldsymbol{\varepsilon}_0^{\mathrm{p}}(x_1, x_2)$ shown in Eq. (44) is plastic strain distribution compatible with the activated slip systems, where $\gamma_1(n_1^1 x_1 + n_2^1 x_2)$ and $\gamma_2(n_1^2 x_1 + n_2^2 x_2)$ are differentiable functions only changing along the normal directions $\vec{\boldsymbol{n}}^1$ and $\vec{\boldsymbol{n}}^2$ of

two independent slip systems respectively. Both **KAM** and **GROD** are identically equal to zero under this distribution, including the homogeneously distributed plastic strain with $\partial\varepsilon_2^{\mathrm{p}}/\partial x_1 = \partial\varepsilon_1^{\mathrm{p}}/\partial x_2 = \partial\gamma_3^{\mathrm{p}}/\partial x_1 = \partial\gamma_3^{\mathrm{p}}/\partial x_2 = 0$ and $\Delta\omega_3 = \Delta\varepsilon^{\mathrm{p}} = \Delta\gamma_3^{\mathrm{p}} = 0$.

$$\boldsymbol{\varepsilon}_0^{\mathrm{p}}(x_1, x_2) = \begin{bmatrix} -\frac{1}{2}\sin 2\varphi_1\gamma_1\left(n_1^1x_1 + n_2^1x_2\right) - \frac{1}{2}\sin 2\varphi_2\gamma_2\left(n_1^2x_1 + n_2^2x_2\right) & \frac{1}{2}\cos 2\varphi_1\gamma_1\left(n_1^1x_1 + n_2^1x_2\right) + \frac{1}{2}\cos 2\varphi_2\gamma_2\left(n_1^2x_1 + n_2^2x_2\right) \\ \frac{1}{2}\cos 2\varphi_1\gamma_1\left(n_1^1x_1 + n_2^1x_2\right) + \frac{1}{2}\cos 2\varphi_2\gamma_2\left(n_1^2x_1 + n_2^2x_2\right) & \frac{1}{2}\sin 2\varphi_1\gamma_1\left(n_1^1x_1 + n_2^1x_2\right) + \frac{1}{2}\sin 2\varphi_2\gamma_2\left(n_1^2x_1 + n_2^2x_2\right) \end{bmatrix} \tag{44}$$

3.4. Dependence of *GROD* and *KAM* distributions on plastic strain modes of SC material

The dependence of lattice curvature on plastic strain modes of SC material has been noticed by Jiang et al. (2016) during their research on the deformation compatibility of a SC Ni superalloy by HR-EBSD. To explain the effect of plastic strain modes on misorientation distribution, we consider the buckling and tension of SC material respectively, and discuss their **GROD** and **KAM** distributions quantitatively. The residual material distortion distribution $\tilde{\boldsymbol{\beta}}_{\mathrm{buckling}}(\vec{\boldsymbol{r}})$ in buckled SC material (see Fig. 3a, it is buckling from x_1Ox_2 view, but bending from x_1Ox_3 view) can be expressed as Eq. (45):

$$\begin{aligned} \tilde{\boldsymbol{\beta}}_{\mathrm{buckling}}(\vec{\boldsymbol{r}}) &= \boldsymbol{\varepsilon}^{\mathrm{p}}(\vec{\boldsymbol{r}}) + \boldsymbol{\Omega}_{\mathrm{material}}(\vec{\boldsymbol{r}}) = \frac{r - r_0}{r_0}\vec{\boldsymbol{e}}_\varphi\vec{\boldsymbol{e}}_\varphi - \frac{r - r_0}{r_0}\vec{\boldsymbol{e}}_r\vec{\boldsymbol{e}}_r + \left(\varphi - \frac{\pi}{2}\right)\vec{\boldsymbol{e}}_r\vec{\boldsymbol{e}}_\varphi - \left(\varphi - \frac{\pi}{2}\right)\vec{\boldsymbol{e}}_\varphi\vec{\boldsymbol{e}}_r \\ &= \frac{r - r_0}{r_0}\cos 2\varphi\vec{\boldsymbol{e}}_3\vec{\boldsymbol{e}}_3 - \frac{r - r_0}{r_0}\cos 2\varphi\vec{\boldsymbol{e}}_1\vec{\boldsymbol{e}}_1 + \left(\varphi - \frac{\pi}{2} - \frac{r - r_0}{r_0}\sin 2\varphi+\right)\vec{\boldsymbol{e}}_1\vec{\boldsymbol{e}}_3 \\ &\quad - \left(\varphi - \frac{\pi}{2} + \frac{r - r_0}{r_0}\sin 2\varphi\right)\vec{\boldsymbol{e}}_3\vec{\boldsymbol{e}}_1 \end{aligned} \tag{45}$$

where r_0 is the neutral radius, r and φ are the polar axis and polar angle respectively under the polar coordinate system with the curvature center as original point. Based on the in-plane slip assumption (both slip direction $\vec{\boldsymbol{s}}^{\alpha}$ and normal direction $\vec{\boldsymbol{n}}^{\alpha}$ are located in the x_1Ox_3 plane) and the previous solved result shown in Eq. (40), both the residual lattice rotation angle $\theta_2(\vec{\boldsymbol{r}})$ and the residual lattice rotation tensor $\tilde{\boldsymbol{\Omega}}_{\mathrm{lattice}}(\vec{\boldsymbol{r}})$ here can be then solved as shown in Eq. (46):

$$\theta_2(\vec{\boldsymbol{r}}) = \frac{\pi}{2} - \varphi + \frac{r_0 - r}{r_0}\frac{\sin(2\varphi - \varphi_1 - \varphi_2)}{\cos(\varphi_1 - \varphi_2)},\quad \tilde{\boldsymbol{\Omega}}_{\mathrm{lattice}}(\vec{\boldsymbol{r}}) = \begin{bmatrix} 0 & 0 & -\theta_2(\vec{\boldsymbol{r}}) \\ 0 & 0 & 0 \\ \theta_2(\vec{\boldsymbol{r}}) & 0 & 0 \end{bmatrix} \tag{46}$$

The GND density tensor distribution $\boldsymbol{\rho}_{\mathrm{GND}}(\vec{\boldsymbol{r}})$ can be calculated from the curl operation on residual lattice rotation tensor $\tilde{\boldsymbol{\Omega}}_{\mathrm{lattice}}(\vec{\boldsymbol{r}})$ as shown in Eq. (47) and Fig. 3b. Edge GND density components $\rho_{\mathrm{GND}}^{\mathrm{e}-r}$ and $\rho_{\mathrm{GND}}^{\mathrm{e}-\varphi}$ will be close to zero when the neutral radius r_0 and polar axis r tend towards infinitude.

$$\begin{aligned} \boldsymbol{\rho}_{\mathrm{GND}}(\vec{\boldsymbol{r}}) &= \rho_{\mathrm{GND}}^{\mathrm{e}-r}b\vec{\boldsymbol{e}}_r\vec{\boldsymbol{e}}_2 + \rho_{\mathrm{GND}}^{\mathrm{e}-\varphi}b\vec{\boldsymbol{e}}_\varphi\vec{\boldsymbol{e}}_2 = \tilde{\boldsymbol{\Omega}}_{\mathrm{lattice}}(\vec{\boldsymbol{r}}) \times \nabla = -\frac{\partial\theta_2}{\partial r}\vec{\boldsymbol{e}}_r\vec{\boldsymbol{e}}_2 - \frac{1}{r}\frac{\partial\theta_2}{\partial\varphi}\vec{\boldsymbol{e}}_\varphi\vec{\boldsymbol{e}}_2 \\ &= \frac{1}{r_0}\frac{\sin(2\varphi - \varphi_1 - \varphi_2)}{\cos(\varphi_1 - \varphi_2)}\vec{\boldsymbol{e}}_r\vec{\boldsymbol{e}}_2 + \left[\frac{1}{r} + 2\left(\frac{1}{r_0} - \frac{1}{r}\right)\frac{\cos(2\varphi - \varphi_1 - \varphi_2)}{\cos(\varphi_1 - \varphi_2)}\right]\vec{\boldsymbol{e}}_\varphi\vec{\boldsymbol{e}}_2 \xrightarrow{r\to r_0,\ \varphi\to\frac{\pi}{2}} \frac{1}{r_0}\frac{\sin(\varphi_1 + \varphi_2)}{\cos(\varphi_1 - \varphi_2)}\vec{\boldsymbol{e}}_3\vec{\boldsymbol{e}}_2 - \frac{1}{r_0}\vec{\boldsymbol{e}}_1\vec{\boldsymbol{e}}_2 \\ &= \overbrace{\begin{bmatrix} 0 & -\frac{1}{r_0} & 0 \\ 0 & 0 & 0 \\ 0 & \frac{1}{r_0}\frac{\sin(\varphi_1+\varphi_2)}{\cos(\varphi_1-\varphi_2)} & 0 \end{bmatrix}}^{\boldsymbol{\rho}_{\mathrm{GND}}\left(r=r_0,\ \varphi=\frac{\pi}{2}\right)} = \overbrace{\begin{bmatrix} 0 & -\frac{1}{r_0} & 0 \\ 0 & 0 & 0 \\ 0 & 0 & 0 \end{bmatrix}}^{\boldsymbol{\rho}_{\mathrm{GND}}^{\mathrm{I}}\left(r=r_0,\ \varphi=\frac{\pi}{2}\right)} + \overbrace{\begin{bmatrix} 0 & 0 & 0 \\ 0 & 0 & 0 \\ 0 & \frac{1}{r_0}\frac{\sin(\varphi_1+\varphi_2)}{\cos(\varphi_1-\varphi_2)} & 0 \end{bmatrix}}^{\boldsymbol{\rho}_{\mathrm{GND}}^{\mathrm{IV}}\left(r=r_0,\ \varphi=\frac{\pi}{2}\right)} \end{aligned} \tag{47}$$

At the special middle position located in $r \to r_0, \varphi \to \pi/2$ near the neutral radius, the GND density tensor $\boldsymbol{\rho}_{\mathrm{GND}}(r = r_0,\ \varphi = \pi/2)$ only contains the first ($\boldsymbol{\rho}_{\mathrm{GND}}^{\mathrm{I}}$) and fourth ($\boldsymbol{\rho}_{\mathrm{GND}}^{\mathrm{IV}}$) sub-GND density tensor items, while the other sub-GND density tensor items $\boldsymbol{\rho}_{\mathrm{GND}}^{\mathrm{II}}$, $\boldsymbol{\rho}_{\mathrm{GND}}^{\mathrm{III}}$ and $\boldsymbol{\rho}_{\mathrm{GND}}^{\mathrm{V}}$ are equal to zero.

If the EBSD observational surface is selected in $x_3 = r_0 + \delta$ (see Fig. 3c, δ is the distance between neutral surface and observational surface), the **GROD** distribution along $x_1 = x$ is captured as Eq. (48). The reference point for **GROD** calculation here is located in the middle position: $r = r_0 + \delta,\ \varphi = \pi/2$. The length of rectangular EBSD observational regions here is 720um, thus x is much smaller than the neutral radius r_0 ($x \to 0$), and the quadratic item x^2 can be then ignored. Finally, the **GROD** distribution tends towards a "V-type" with $1/r_0$ slope, regardless of slip systems' azimuthal angles φ_1, φ_2 when the EBSD observational surface is very close to the neutral surface ($\delta \to 0$).

$$\begin{aligned} \mathbf{GROD}(x) &= \left|\theta_2\left(r = \sqrt{(r_0 + \delta)^2 + x^2}, \varphi = \arccos\frac{x}{\sqrt{(r_0 + \delta)^2 + x^2}}\right) - \theta_2\left(r = r_0 + \delta, \varphi = \frac{\pi}{2}\right)\right| \\ &= \left|\frac{\pi}{2} - \arccos\left(\frac{x}{\sqrt{(r_0 + \delta)^2 + x^2}}\right) + \frac{r_0 - \sqrt{(r_0 + \delta)^2 + x^2}}{r_0}\cdot\frac{2(r_0 + \delta)x\cdot\cos(\varphi_1 + \varphi_2) - 2x^2\cdot\sin(\varphi_1 + \varphi_2)}{\left[(r_0 + \delta)^2 + x^2\right]\cdot\cos(\varphi_1 - \varphi_2)}\right| \\ &\xrightarrow{x\to 0} \left|-\frac{x}{r_0 + \delta} + \frac{\delta}{r_0}\cdot\frac{2x\cdot\cos(\varphi_1 + \varphi_2)}{(r_0 + \delta)\cdot\cos(\varphi_1 - \varphi_2)}\right| = \left|\frac{2\delta}{r_0}\cdot\frac{\cos(\varphi_1 + \varphi_2)}{\cos(\varphi_1 - \varphi_2)} - 1\right|\cdot\frac{|x|}{r_0 + \delta} \xrightarrow{\delta\to 0} \frac{|x|}{r_0} \end{aligned} \tag{48}$$

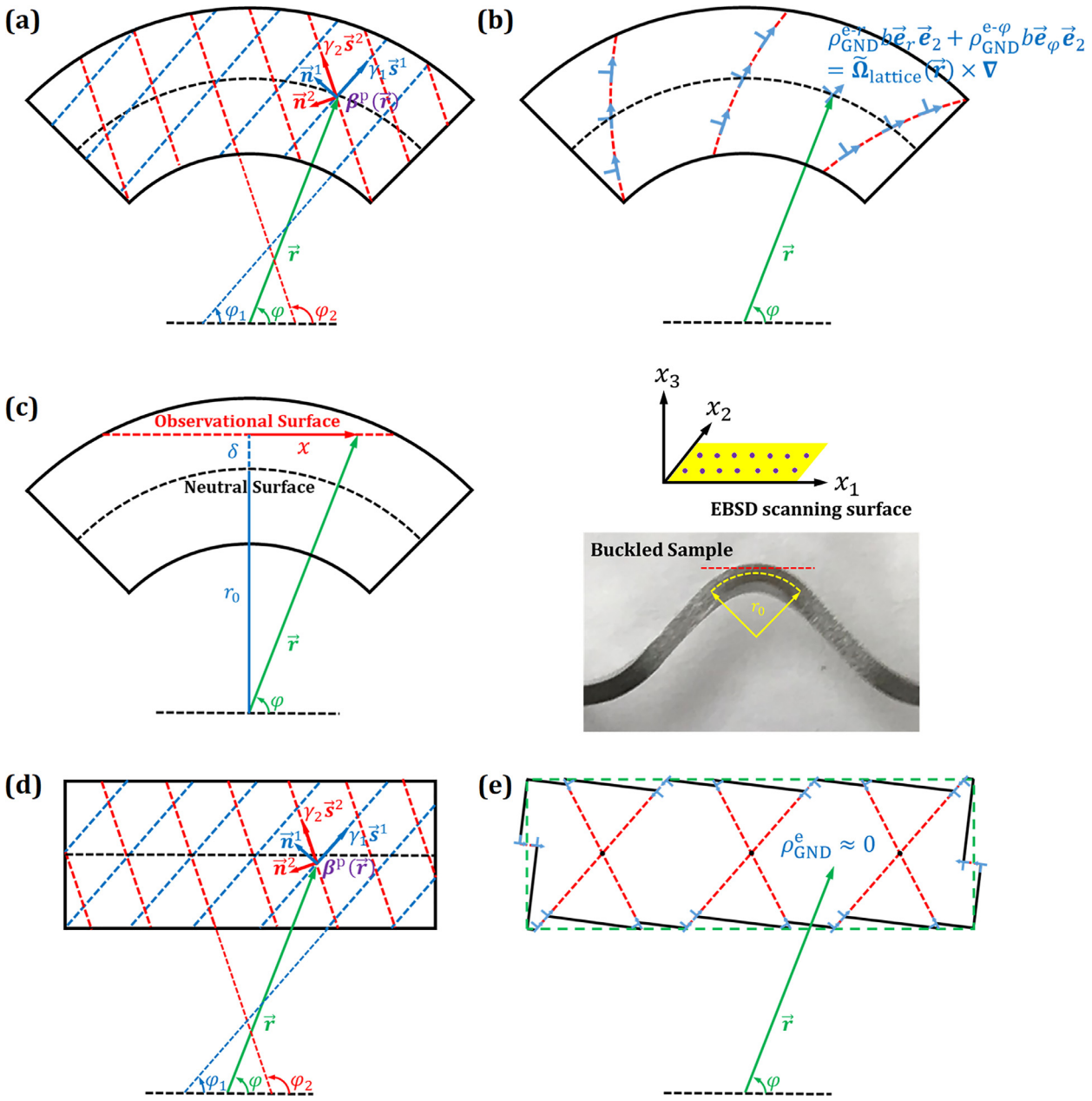

Fig. 3. Schematic diagrams of (a) residual material distortion and (b) GND distribution in the buckled SC sample, (c) EBSD observational surface in the buckled SC sample, as well as (d) residual material distortion and (e) GND distribution in the tensile SC sample.

Then the objective $\mathbf{KAM}^{\mathrm{obj}}$ distribution along $x_1 = x$ is captured as Eq. (49), which is equal to the buckling curvature $1/r_0$. This value is also exactly the first in-surface invariant $\rho^{\mathrm{I}}_{\mathrm{GND}}$ of the GND density tensor, i.e. the first sub-parameter $\mathbf{KAM}^{\mathrm{I}}_{\mathrm{GND}}$ of the total objective parameter $\mathbf{KAM}^{\mathrm{obj}}$, while the other sub-parameters $\mathbf{KAM}^{\mathrm{II}}_{\mathrm{GND}}$ and $\mathbf{KAM}^{\mathrm{III}}_{\mathrm{GND}}$ are equal to zero.

$$\mathbf{KAM}^{\mathrm{obj}}(x) = \left| \frac{\partial \theta_2}{\partial x}\left(r = \sqrt{(r_0+\delta)^2 + x^2},\ \varphi = \arccos\frac{x}{\sqrt{(r_0+\delta)^2+x^2}} \right) \right|$$
$$\xrightarrow{x\to 0,\ \delta\to 0} \frac{1}{r_0} = \sqrt{\boldsymbol{\rho}^{\mathrm{I}}_{\mathrm{GND}}\left(r=r_0,\ \varphi=\frac{\pi}{2}\right) : \boldsymbol{\rho}^{\mathrm{I}}_{\mathrm{GND}}\left(r=r_0,\ \varphi=\frac{\pi}{2}\right)} = \mathbf{KAM}^{\mathrm{I}}_{\mathrm{GND}},\ \mathbf{KAM}^{\mathrm{II}}_{\mathrm{GND}} = \mathbf{KAM}^{\mathrm{III}}_{\mathrm{GND}} = 0 \tag{49}$$

Compared with the above buckled SC material, the tensile SC material displays a different residual material distortion tensor $\tilde{\boldsymbol{\beta}}_{\text{tension}}(\vec{\boldsymbol{r}})$ distribution as shown in Fig. 3d and Eq. (50):

$$\tilde{\boldsymbol{\beta}}_{\text{tension}}(\vec{\boldsymbol{r}}) = \boldsymbol{\varepsilon}^{\text{p}} = \varepsilon^{\text{p}}\vec{\boldsymbol{e}}_1\vec{\boldsymbol{e}}_1 - \varepsilon^{\text{p}}\vec{\boldsymbol{e}}_3\vec{\boldsymbol{e}}_3 \tag{50}$$

Based on the previous solved result shown in Eq. (40), both the residual lattice rotation angle $\theta_2(\vec{\boldsymbol{r}})$ and the residual lattice rotation tensor $\tilde{\boldsymbol{\Omega}}_{\text{lattice}}$ distribution here can also be solved as shown in Eq. (51):

$$\theta_2(\vec{\boldsymbol{r}}) = -\frac{\sin(\varphi_1+\varphi_2)}{\cos(\varphi_1-\varphi_2)}\varepsilon^{\text{p}},\ \ \tilde{\boldsymbol{\Omega}}_{\text{lattice}} = \begin{bmatrix} 0 & 0 & -\theta_2(\vec{\boldsymbol{r}}) \\ 0 & 0 & 0 \\ \theta_2(\vec{\boldsymbol{r}}) & 0 & 0 \end{bmatrix} \tag{51}$$

From the above result we can see that the residual lattice rotation tensor $\tilde{\boldsymbol{\Omega}}_{\text{lattice}}$ is homogenously distributed thus the GND density (Fig. 3e) calculated from the curl operation on $\tilde{\boldsymbol{\Omega}}_{\text{lattice}}$ tends to zero:

$$\boldsymbol{\rho}_{\text{GND}} = \tilde{\boldsymbol{\Omega}}_{\text{lattice}} \times \nabla = 0 \tag{52}$$

Similarly, the **GROD** distribution along $x_1 = x$ in the similar EBSD observational region is captured as shown in Eq. (53), which is identically equal to zero.

$$\mathbf{GROD}(x) = \left| \theta_2\left(r = \sqrt{(r_0+\delta)^2 + x^2}, \varphi = \arccos\frac{x}{\sqrt{(r_0+\delta)^2+x^2}} \right) - \theta_2\left(r = r_0+\delta, \varphi = \frac{\pi}{2} \right) \right| = 0 \tag{53}$$

And the objective $\mathbf{KAM}^{\text{obj}}$ distribution along $x_1 = x$ is captured as Eq. (54), which is also identically equal to zero. All the sub-parameters $\mathbf{KAM}^{\text{I}}_{\text{GND}}$, $\mathbf{KAM}^{\text{II}}_{\text{GND}}$ and $\mathbf{KAM}^{\text{III}}_{\text{GND}}$ are equal to zero in this case.

$$\mathbf{KAM}^{\text{obj}}(x) = \left| \frac{\partial\theta_2}{\partial x}\left(r = \sqrt{(r_0+\delta)^2 + x^2}, \varphi = \arccos\frac{x}{\sqrt{(r_0+\delta)^2+x^2}} \right) \right| = 0 \tag{54}$$

The above derivation revealed that the **GROD** and **KAM** distribution in SC material strongly depends on the plastic strain modes. Both **GROD** and **KAM** have the capability of characterizing the gradient plastic strain incompatible with the given slip systems in the buckled SC material, rather than the homogenous plastic strain compatible with the given slip systems in the tensile SC material.

3.5. Linear evolution of $\overline{\mathbf{KAM}}$ *and* $\overline{\mathbf{GROD}}$ *averaged over multiple grains in tension of PC material*

SC and PC materials follow different misorientation evolution laws during the tensile deformation. Here we established a simple 2D PC model to explain the linear evolution of $\overline{\mathbf{KAM}}$ and $\overline{\mathbf{GROD}}$ averaged over multiple grains widely reported in tension of PC material (Kamaya et al., 2005; Kamaya et al., 2006; Kamaya et al., 2007; Kamaya, 2009; Kamaya, 2011). A spheroidal grain with the diameter of D_{Grain} is deeply placed inside the PC material and surrounded by the neighboring grains (D, E, F, H, I and J), whose center is selected as the reference point (Fig. 4a-c). Then we analyzed the residual in-plane material distortion $\tilde{\boldsymbol{\beta}}$ and residual in-plane lattice rotation $\tilde{\boldsymbol{\Omega}}_{\text{lattice}}$ inside each spheroidal grain based on the following four hypotheses: i) the residual material distortion at the grain center $\tilde{\boldsymbol{\beta}}(0)$ is equal to the nominal plastic strain $\boldsymbol{\varepsilon}^{\text{p}}_{\text{applied}}$ applied in the far field; ii) the residual lattice rotation near the grain boundary $\tilde{\boldsymbol{\Omega}}^{\boldsymbol{\Gamma}}_{\text{lattice}}$ approaches to zero due to the constraint of fixed orientation relationship between the two sides of grain boundary; iii) two independent non-orthogonal slip systems located in plane are activated inside each spheroidal grain, and their azimuthal angles are set as φ_1, φ_2 respectively; iv) the residual lattice rotation $\tilde{\boldsymbol{\Omega}}_{\text{lattice}}(r)$ distribution is isotropic (only relies on polar axis r), and the edge GND density $\rho^{\text{e}}_{\text{GND}}$ distribution is uniform (relies on neither polar axis r nor polar angle φ) inside each spheroidal grain.

Based on the residual material distortion at the grain center $\tilde{\boldsymbol{\beta}}(0) = \boldsymbol{\varepsilon}^{\text{p}}_{\text{applied}}$ given by the first hypotheses, Eq. (55) concerning the residual lattice rotation angle $\theta_3(0)$ and the residual lattice rotation tensor $\tilde{\boldsymbol{\Omega}}_{\text{lattice}}(0)$ at the grain center can be then established as follows:

$$\tilde{\boldsymbol{\beta}}(0) = \boldsymbol{\varepsilon}^{\text{p}}_{\text{applied}} = \begin{bmatrix} -\varepsilon^{\text{p}} & 0 \\ 0 & \varepsilon^{\text{p}} \end{bmatrix} = \boldsymbol{\beta}^{\text{p}}(0) + \tilde{\boldsymbol{\Omega}}_{\text{lattice}}(0) \tag{55}$$

According to the second hypotheses, the residual lattice rotation tensor $\tilde{\boldsymbol{\Omega}}^{\boldsymbol{\Gamma}}_{\text{lattice}}$ near the grain boundary $\boldsymbol{\Gamma}$ approaches to zero, thus the residual lattice rotation angle $\theta_3(\text{D}_{\text{Grain}}/2)$ and the residual lattice rotation tensor $\tilde{\boldsymbol{\Omega}}_{\text{lattice}}(\text{D}_{\text{Grain}}/2)$ at the grain boundary can be determined as shown in Eq. (56):

$$\tilde{\boldsymbol{\Omega}}_{\text{lattice}}\left(\frac{\text{D}_{\text{Grain}}}{2}\right) = \begin{bmatrix} 0 & \theta_3\left(\frac{\text{D}_{\text{Grain}}}{2}\right) \\ -\theta_3\left(\frac{\text{D}_{\text{Grain}}}{2}\right) & 0 \end{bmatrix} = \tilde{\boldsymbol{\Omega}}^{\boldsymbol{\Gamma}}_{\text{lattice}} = 0 \tag{56}$$

Then the boundary conditions $\theta_3(0)$ and $\theta_3(\text{D}_{\text{Grain}}/2)$ of the residual lattice rotation angle distribution $\theta_3(r)$ can be solved from Eqs. (55) and (56) respectively based on the in-plane slip assumption given by the third hypotheses and the previous

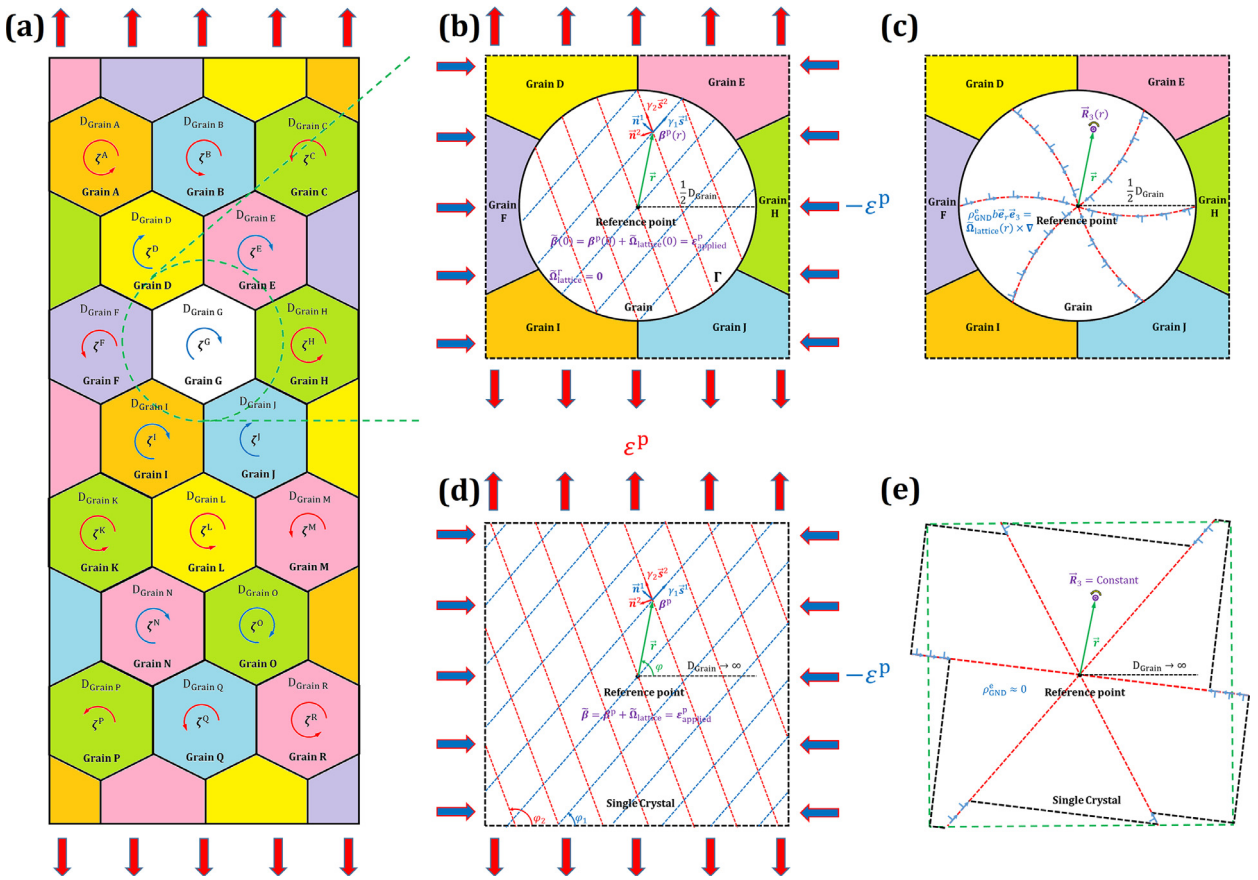

Fig. 4. Schematic diagrams of (a) intragranular misorientation averaged over multiple grains, (b) residual material distortion and (c) GND distribution within each single grain of the tensile PC sample, as well as (d) residual material distortion and (e) GND distribution in the tensile SC sample.

solved result shown in Eq. (40). The $\theta_3(0)$ at the grain center relies on not only applied strain ε^{p}, but also azimuthal angles φ_1, φ_2 of slip systems.

$$\theta_3(0) = -\frac{\sin(\varphi_1+\varphi_2)}{\cos(\varphi_1-\varphi_2)}\varepsilon^{\mathrm{p}},\ \ \theta_3\left(\frac{\mathrm{D_{Grain}}}{2}\right)=0,\ \ \tilde{\boldsymbol{\Omega}}_{\mathrm{lattice}}(r)=\begin{bmatrix}0 & \theta_3(r)\\ -\theta_3(r) & 0\end{bmatrix} \tag{57}$$

To further determine the functional form of the residual lattice rotation angle $\theta_3(r)$ distribution along the polar axis inside the spheroidal grain, the last hypothesis should be taken into consideration. The edge GND density $\rho^{\mathrm{e}}_{\mathrm{GND}}$ can be calculated from the curl operation on the residual lattice rotation tensor $\tilde{\boldsymbol{\Omega}}_{\mathrm{lattice}}(r)$, and the result will be independent of the position vector $\vec{\boldsymbol{r}}$ (both polar axis r and polar angle φ) when the $\theta_3(r)$ follows a linear relationship with the polar axis r, as shown in Eq. (58):

$$\boldsymbol{\rho}_{\mathrm{GND}} = \rho^{\mathrm{e}}_{\mathrm{GND}} b\vec{\boldsymbol{e}}_r\vec{\boldsymbol{e}}_3 = \tilde{\boldsymbol{\Omega}}_{\mathrm{lattice}}(r)\times\nabla = -\frac{\partial\theta_3(r)}{\partial r}\vec{\boldsymbol{e}}_r\vec{\boldsymbol{e}}_3,\ \ \theta_3(r)=\frac{\sin(\varphi_1+\varphi_2)}{\cos(\varphi_1-\varphi_2)}\varepsilon^{\mathrm{p}}\left(\frac{2r}{\mathrm{D_{Grain}}}-1\right) \tag{58}$$

Then the absolute value of edge GND density $\rho^{\mathrm{e}}_{\mathrm{GND}}$ (see a similar result in Ref. (Ashby, 1970)) and the residual orientation gradient tensor $\tilde{\boldsymbol{\kappa}}$ in unloaded elastic-plastic condition can be calculated from the above GND density tensor $\boldsymbol{\rho}_{\mathrm{GND}}$ respectively as shown in Eq. (59), where b is the magnitude of burgers vector.

$$\rho^{\mathrm{e}}_{\mathrm{GND}} = \left|\frac{\sin(\varphi_1+\varphi_2)}{\cos(\varphi_1-\varphi_2)}\right|\frac{2\varepsilon^{\mathrm{p}}}{b\mathrm{D_{Grain}}},\ \ \tilde{\boldsymbol{\kappa}}=\frac{1}{2}(\boldsymbol{\rho}_{\mathrm{GND}}:\mathbf{I})\mathbf{I}-\boldsymbol{\rho}^{\mathbf{T}}_{\mathrm{GND}}=\frac{\sin(\varphi_1+\varphi_2)}{\cos(\varphi_1-\varphi_2)}\frac{2\varepsilon^{\mathrm{p}}}{\mathrm{D_{Grain}}}\vec{\boldsymbol{e}}_3\vec{\boldsymbol{e}}_r \tag{59}$$

Local **KAM** value can be calculated from the average projection of residual orientation gradient tensor $\tilde{\boldsymbol{\kappa}}$ along $a\vec{\boldsymbol{e}}_1$ and $a\vec{\boldsymbol{e}}_2$ (a is the EBSD scanning step size) as shown in Eq. (60) according to its original definition (Eq. (10)), which is independent of the polar axis r but relies on the polar angle φ.

$$\mathbf{KAM}(\varphi)=\frac{a}{2}(|\cos\varphi|+|\sin\varphi|)\left|\frac{\sin(\varphi_1+\varphi_2)}{\cos(\varphi_1-\varphi_2)}\right|\frac{2\varepsilon^{\mathrm{p}}}{\mathrm{D_{Grain}}}=\frac{a}{2}(|\cos\varphi|+|\sin\varphi|)\ \zeta(\varphi_1,\varphi_2)\frac{2\varepsilon^{\mathrm{p}}}{\mathrm{D_{Grain}}} \tag{60}$$

If local **KAM** values are averaged over the whole grain area S_{Grain} at first, the $\mathbf{KAM}_{ave}$ can be then expressed as Eq. (61), which no longer relies on the polar angle φ.

$$\mathbf{KAM}_{ave} = \frac{1}{S_{Grain}} \int_0^{2\pi} \mathbf{KAM}(\varphi) \frac{1}{2} \left(\frac{D_{Grain}}{2} \right)^2 d\varphi = \frac{a\zeta \varepsilon^p}{2\pi D_{Grain}} \int_0^{2\pi} (|\cos\varphi| + |\sin\varphi|) d\varphi = \frac{4a\zeta \varepsilon^p}{\pi D_{Grain}} \tag{61}$$

where $\zeta(\varphi_1, \varphi_2) = |\sin(\varphi_1 + \varphi_2)/\cos(\varphi_1 - \varphi_2)|$ is the factor including the azimuthal angles φ_1, φ_2 of slip systems. From Eq. (61) we can see that $\mathbf{KAM}_{ave}$ is proportional to the nominal plastic strain ε^p but inversely proportional to the grain size D_{Grain}. Combining with Eq. (59), $\mathbf{KAM}_{ave}$ can be further translated into $(2ab/\pi)\rho^e_{GND}$. Thus $\mathbf{KAM}_{ave}$ serves as a good measure of GND density of each grain.

Local **GROD** value can be calculated from the relative lattice rotation angle $|\theta_3(r) - \theta_3(0)|$ as shown in Eq. (62) according to its original definition Eq. (11) when the grain center was selected as the reference point, which is independent of the polar angle φ but relies on the polar axis r.

$$\mathbf{GROD}(r) = |\theta_3(r) - \theta_3(0)| = \left| \frac{\sin(\varphi_1 + \varphi_2)}{\cos(\varphi_1 - \varphi_2)} \right| \frac{2r}{D_{Grain}} \varepsilon^p = \zeta(\varphi_1, \varphi_2) \frac{2r}{D_{Grain}} \varepsilon^p \tag{62}$$

If local **GROD** values were averaged over the whole grain area S_{Grain} at first, $\mathbf{GROD}_{ave}$ can be then expressed as Eq. (63), which no longer relies on the polar axis r.

$$\mathbf{GROD}_{ave} = \frac{1}{S_{Grain}} \int_0^{\frac{D_{Grain}}{2}} \mathbf{GROD}(r) 2\pi r dr = \frac{16\zeta \varepsilon^p}{D^3_{Grain}} \int_0^{\frac{D_{Grain}}{2}} r^2 dr = \frac{2}{3} \zeta \varepsilon^p \tag{63}$$

where $\zeta(\varphi_1, \varphi_2)$ is the same factor as that in Eq. (61). From Eq. (63) we can see that $\mathbf{GROD}_{ave}$ is proportional to the nominal plastic strain ε^p but independent of the grain size D_{Grain}.

To further eliminate the influence of various grain lattice orientations (usually with different azimuthal angles φ_1, φ_2 of slip systems) on the above linear relationship as much as possible, the $\mathbf{KAM}_{ave}$ values already averaged over the whole grain area S_{Grain} need to be further averaged over a representative region containing enough grains A, B, C…as shown in Fig. 4a and Eq. (64):

$$\overline{\mathbf{KAM}} = \frac{S_{Grain\ A} \cdot \mathbf{KAM}^A_{ave} + S_{Grain\ B} \cdot \mathbf{KAM}^B_{ave} + S_{Grain\ C} \cdot \mathbf{KAM}^C_{ave} + \cdots}{S_{Grain\ A} + S_{Grain\ B} + S_{Grain\ C} + \cdots} = \frac{4a\zeta^* \varepsilon^p}{\pi D^*_{Grain}} = \frac{2ab}{\pi} \bar{\rho}^e_{GND} \tag{64}$$

where ζ^* and D^*_{Grain} are the equivalent values of factors ζ^A, ζ^B, ζ^C… and grain diameters $D_{Grain\,A}$, $D_{Grain\,B}$, $D_{Grain\,C}$…. respectively in grain A, B, C… averaged by the following method in Eq. (65):

$$\frac{\zeta^*}{D^*_{Grain}} = \frac{S_{Grain\ A} \cdot \dfrac{\zeta^A}{D_{Grain\ A}} + S_{Grain\ B} \cdot \dfrac{\zeta^B}{D_{Grain\ B}} + S_{Grain\ C} \cdot \dfrac{\zeta^C}{D_{Grain\ C}} + \cdots}{S_{Grain\ A} + S_{Grain\ B} + S_{Grain\ C} + \cdots} \not\sim (\varphi_1, \varphi_2) \tag{65}$$

For the same purpose, the $\mathbf{GROD}_{ave}$ values already averaged over the whole grain area S_{Grain} need to be further averaged over a representative region containing enough grains A, B, C…as shown in Fig. 4a and Eq. (66):

$$\overline{\mathbf{GROD}} = \frac{S_{Grain\ A} \cdot \mathbf{GROD}^A_{ave} + S_{Grain\ B} \cdot \mathbf{GROD}^B_{ave} + S_{Grain\ C} \cdot \mathbf{GROD}^C_{ave} + \cdots}{S_{Grain\ A} + S_{Grain\ B} + S_{Grain\ C} + \cdots} = \frac{2}{3} \zeta^{**} \varepsilon^p \tag{66}$$

where ζ^{**} is another equivalent value of factors ζ^A, ζ^B, ζ^C…in grain A, B, C… averaged by the following method in Eq. (67):

$$\zeta^{**} = \frac{S_{Grain\ A} \cdot \zeta^A + S_{Grain\ B} \cdot \zeta^B + S_{Grain\ C} \cdot \zeta^C + \cdots}{S_{Grain\ A} + S_{Grain\ B} + S_{Grain\ C} + \cdots} \not\sim (\varphi_1, \varphi_2) \tag{67}$$

Both the equivalent factors ζ^* and ζ^{**} here are independent of the individual grain lattice orientation. Compared with $\overline{\mathbf{KAM}}$ more suitable for describing the distribution of average edge GND density $\bar{\rho}^e_{GND}$, the $\overline{\mathbf{GROD}}$ here is more suitable for characterizing the plastic strain ε^p applied in PC material, for its independence of the EBSD scanning step size a and the equivalent grain diameters D^*_{Grain}.

In summary, the grain boundary plays an important role in the intragranular misorientation evolution during the plastic deformation of PC material (Sun et al., 2000; Dahlberg et al., 2017). It is the grain boundaries' constraint on lattice rotation that results in the relative lattice rotation $\vec{\boldsymbol{R}}_3(r) = [\theta_3(r) - \theta_3(0)]\vec{\boldsymbol{e}}_3$ between center and boundary of each grain, as shown in Fig. 4b and c. Meanwhile, that is also exactly the reason why both $\overline{\mathbf{KAM}}$ and $\overline{\mathbf{GROD}}$ follow a linear evolution law with the nominal plastic strain ε^p applied in the PC material. As a contrast, the lattice rotation during the tensile deformation of SC material free from the grain boundaries' constraint is always synchronous without introducing any relative lattice rotation, i.e. $\theta_3(r) = \theta_3(0)$ and $\vec{\boldsymbol{R}}_3(r) = \vec{0}$, as shown in Fig. 4d and e. This case is equivalent to $D_{Grain} \to \infty$ in Eqs. (59), (60) and (62), which finally results in $\rho^e_{GND} \approx 0$, $\mathbf{KAM} \approx 0$ and $\mathbf{GROD} \approx 0$.

4. Experimental validation on the evolution laws of KAM and GROD

4.1. Comparison of misorientation evolution laws between the tension tests of SC and PC samples

SC and PC Ni-based superalloys showed different mechanical behaviors in tension tests (Fig. 5). The yield stress of PC superalloy (1250 MPa) is a little higher than that of SC superalloy (960 MPa), and the hardening effect of the former is more obvious than that of the latter. Four interrupted cases with various deformation levels for coupled EBSD & DIC characterizations are A (0%), B (1.1%), C (2.4%), D (4.1%) in the SC sample #1 and E (0%), F (1.5%), G (3%), H (4.8%) in the PC sample #2.

Fig. 6 shows the evolution laws of residual material distortion (including normal plastic strain components ε_1^p, ε_2^p and von-Mises equivalent plastic strain ε_v^p measured by μ-DIC) and local misorientation (including **KAM** and **GROD** measured

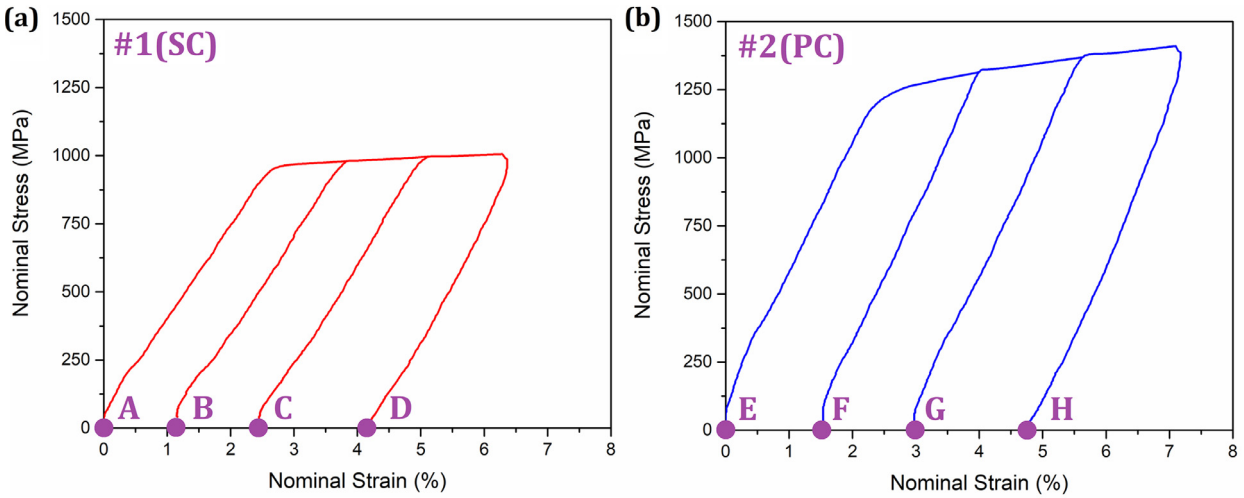

Fig. 5. Nominal stress – nominal strain curves of tensile (a) SC sample #1 and (b) PC sample #2.

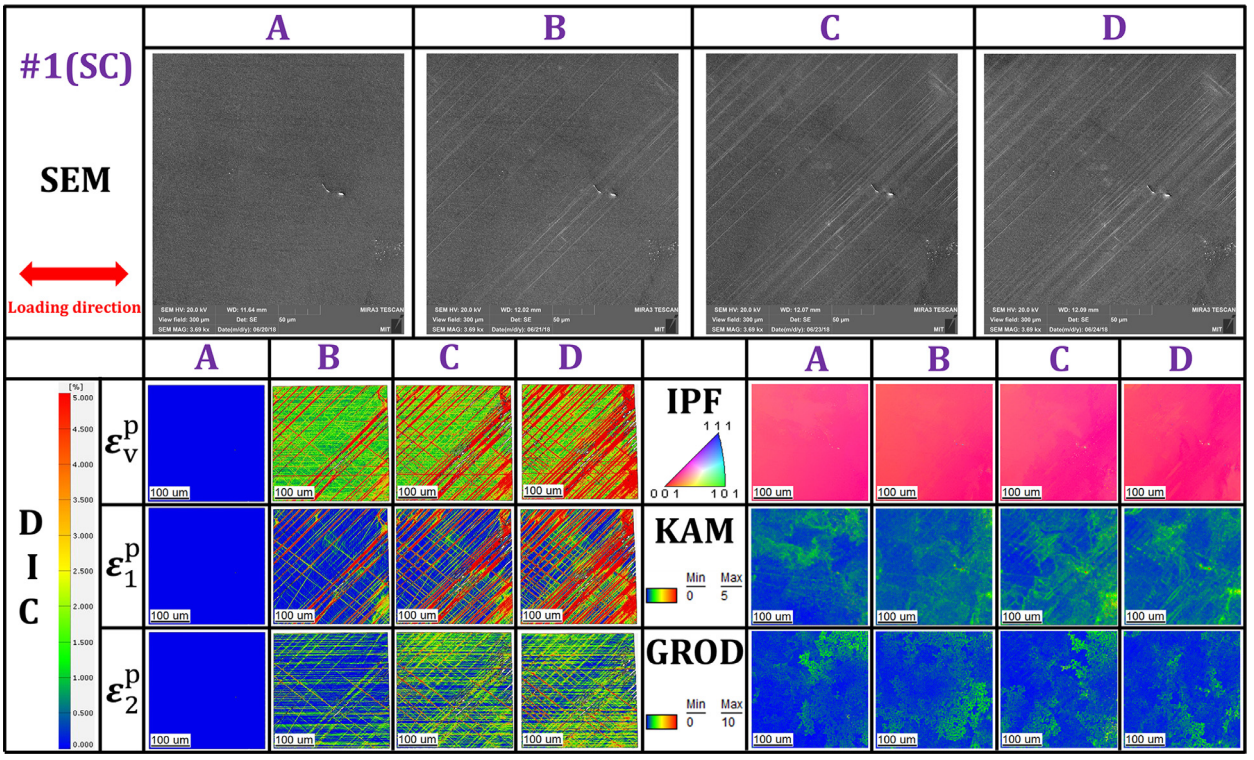

Fig. 6. Residual material distortion and local misorientation evolution in the SC sample #1.

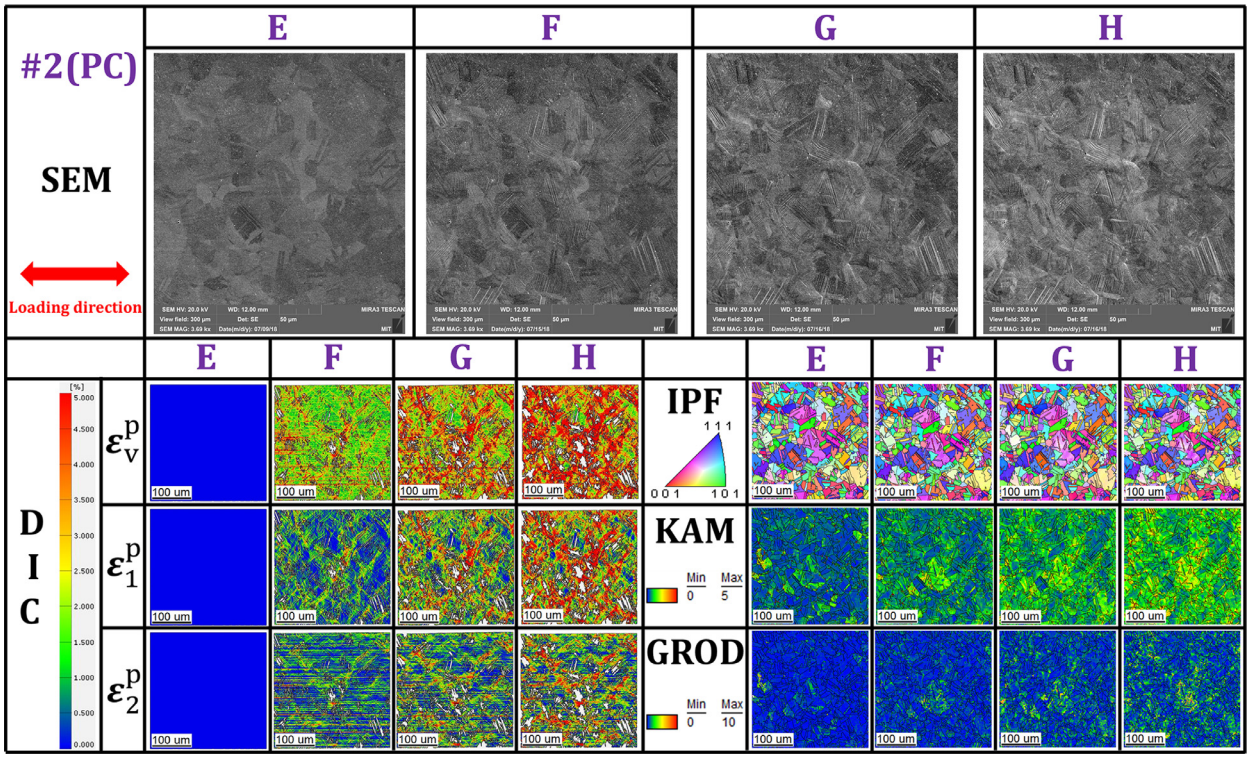

Fig. 7. Residual material distortion and intragranular misorientation evolution in the PC sample #2.

by 2D-EBSD) in the SC sample #1. From the μ-DIC maps, we can see clearly that strain localization occurred in the active slip bands, and the slip bands became denser and denser accompanied by the development of applied nominal strain. Meanwhile, the misorientation parameters ($\overline{\textbf{KAM}}$ & $\overline{\textbf{GROD}}$) averaged over the whole EBSD observational area in SC sample #1 keeps almost constant (Fig. 8a) during the tension test, while the local misorientation distribution shown in both **KAM** and **GROD** maps is obviously different from the microstructural plastic strain ($\varepsilon_1^{\mathrm{p}}$, $\varepsilon_2^{\mathrm{p}}$ and $\varepsilon_{\mathrm{v}}^{\mathrm{p}}$) distribution shown in μ-DIC maps.

Fig. 7 shows the evolution laws of residual material distortion and intragranular misorientation in the PC sample #2. The same as the previous SC sample #1, the intragranular misorientation distribution within each single grain shown in both **KAM** and **GROD** maps also does not correspond to the microstructural plastic strain distribution shown in μ-DIC maps. But different from the SC sample #1, the continuous slip bands here are interrupted by grain boundaries, and the misorientation parameters ($\overline{\textbf{KAM}}$ & $\overline{\textbf{GROD}}$) averaged over the whole EBSD observational area in PC sample #2 increases with the development of applied nominal plastic strain linearly (Fig. 8b). This experimental result here agrees with the theoretical analysis shown in previous Section 3.5 exactly, which reveals that the diffraction-based misorientation mapping only works in the estimation of tensile deformation applied in the PC, rather than the SC metallic materials.

4.2. Comparison between misorientation and distortion distributions in tension of notched SC sample

Compared with the previous smooth SC sample #1, the existence of the central hole in the notched SC sample #3 will induce inhomogeneous plastic strain distribution around the hole during the tensile deformation. Four cases with various stress levels I (0 MPa), J (400 MPa), K (1094 MPa) and L (1120 MPa) were interrupted for coupled EBSD & DIC characterizations, and the evolution of residual material distortion and local misorientation distribution around the central hole was captured and shown in Fig. 9. Different from the above smooth SC sample #1 without any evolution of $\overline{\textbf{KAM}}$ and $\overline{\textbf{GROD}}$ during the tensile deformation, the notched SC sample #3 here shows an obvious increase of local misorientation (especially **GROD**) in the bottom right corner of the central hole.

To further analyze the distribution of microstructural plastic strain ($\varepsilon_1^{\mathrm{p}}$, $\varepsilon_2^{\mathrm{p}}$, γ_3^{p}), material rotation (ω_3) and relative lattice rotation (θ_3 and **GROD**) around the central hole, we selected a concentric circuit with a radius of 150um around the central hole to draw the distribution curves of the above physical quantities. The bottom middle point in the circuit was specified as the reference point for calculation of relative lattice rotation θ_3 and **GROD**. Obviously, there are four positive peak values ε^{p} in distribution curves of normal plastic strains $\varepsilon_1^{\mathrm{p}}$ & $\varepsilon_2^{\mathrm{p}}$ (Fig. 10a and b), as well as two positive peak values $\gamma^{\mathrm{p}}(\omega)$ and two negative peak values $-\gamma^{\mathrm{p}}(-\omega)$ in distribution curves of shearing plastic strain γ_3^{p} (Fig. 10c) and material rotation ω_3 (Fig. 10d) respectively along the circuit in deformed case L.

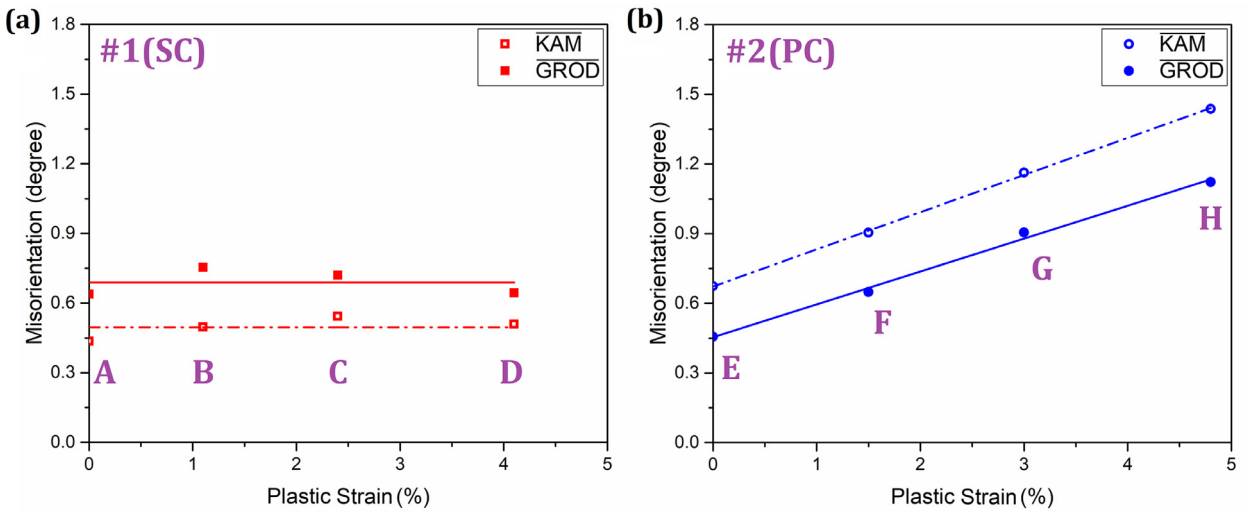

Fig. 8. Evolution of misorientation parameters averaged over the whole EBSD observational area with the nominal plastic strain applied in SC and PC samples.

However, the θ_3 and **GROD** maps here show a quite different distribution along the circuit. Only one peak appears in the distribution curve of relative lattice rotation angle **GROD** (Fig. 11a) in deformed case L compared with undeformed case I, while multiple peaks exist in the distribution curves of plastic strain components $\varepsilon_1^{\mathrm{p}}$, $\varepsilon_2^{\mathrm{p}}$, γ_3^{p} (Fig. 10a–c), especially absolute material rotation angle $|\omega_3|$ (Fig. 11b) in deformed case L. This difference indicates that neither the local plastic strain, nor the local material rotation corresponds to the local misorientation (especially **GROD**), i.e. the latter cannot serve as a measure of local plastic strain or material rotation alone in the SC material. This is also the reason why both local misorientation distribution in SC sample #1 and intragranular misorientation distribution in PC sample #2 do not correspond to the local plastic strain distributions.

Moreover, the above non-correspondence can be explained by the previous theoretical analysis shown in Section 3.3. From the μ-DIC maps shown in Fig. 9 and the distribution curves of material distortion components ($\varepsilon_1^{\mathrm{p}}$, $\varepsilon_2^{\mathrm{p}}$, γ_3^{p} and ω_3) around the central hole shown in Fig. 10, we can notice the $\varepsilon_1^{\mathrm{p}}$ and $\varepsilon_2^{\mathrm{p}}$ distributions with quartic rotational symmetry, as well as the γ_3^{p} and ω_3 distributions with quadratic rotational symmetry. The peak values of normal plastic strains $\varepsilon_1^{\mathrm{p}}$ & $\varepsilon_2^{\mathrm{p}}$, shearing plastic strain γ_3^{p} and material rotation ω_3 in the bottom right corner, top right corner, top left corner and bottom left corner can be approximately recorded as $(\varepsilon^{\mathrm{p}}, -\gamma^{\mathrm{p}}, -\omega)$, $(\varepsilon^{\mathrm{p}}, \gamma^{\mathrm{p}}, \omega)$, $(\varepsilon^{\mathrm{p}}, -\gamma^{\mathrm{p}}, -\omega)$ and $(\varepsilon^{\mathrm{p}}, \gamma^{\mathrm{p}}, \omega)$ respectively as shown in the fourth SEM image of Fig. 9. Meanwhile, only one major slip system was activated in each corner around the central hole (azimuthal angles $\varphi_1 = \varphi_2 = \psi$), and the slip directions indicated by the slip traces are also marked in the fourth SEM image of Fig. 9. Here the slip directions in the top right corner, top left corner and bottom left corner point toward the hole center with centrosymmetry, whose azimuthal angles can be approximately recorded as ψ, $\pi - \psi$ and ψ respectively. But the slip direction in the bottom right corner tangents to the hole, whose azimuthal angle can be approximately recorded as ψ, rather than $\pi - \psi$. The $(\varepsilon_{\mathrm{ref}}^{\mathrm{p}}, \gamma_{\mathrm{ref}}^{\mathrm{p}}, \omega_{\mathrm{ref}})$ at the reference point (bottom middle point) is close to zero (Fig. 10), thus the **GROD** values in four corners can be determined by the material distortion components and azimuthal angles of slip directions according to Eqs. (40) and (41). As the results shown in Eq. (68), the $\mathbf{GROD}^{\text{bottom right corner}}$ will be much higher than the other three **GROD** values for its special slip direction is not centrosymmetric with the other three slip directions, if $\mathbf{GROD}^{\text{top right corner}} = \mathbf{GROD}^{\text{top left corner}} = \mathbf{GROD}^{\text{bottom left corner}}$ are minor values.

$$\left.\begin{aligned}
&\mathbf{GROD}^{\text{top right corner}} = \mathbf{GROD}(\varepsilon^{\mathrm{p}},\ \gamma^{\mathrm{p}}, \omega, \psi) = |\omega + \sin 2\psi \cdot \varepsilon^{\mathrm{p}} - \cos 2\psi \cdot \gamma^{\mathrm{p}}| \\
&\mathbf{GROD}^{\text{top left corner}} = \mathbf{GROD}(\varepsilon^{\mathrm{p}}, -\gamma^{\mathrm{p}}, -\omega, \pi - \psi) = |-\omega - \sin 2\psi \cdot \varepsilon^{\mathrm{p}} + \cos 2\psi \cdot \gamma^{\mathrm{p}}| \\
&\mathbf{GROD}^{\text{bottom left corner}} = \mathbf{GROD}(\varepsilon^{\mathrm{p}}, \gamma^{\mathrm{p}}, \omega, \psi) = |\omega + \sin 2\psi \cdot \varepsilon^{\mathrm{p}} - \cos 2\psi \cdot \gamma^{\mathrm{p}}|
\end{aligned}\right\} \text{Minor values}$$

$$\mathbf{GROD}^{\text{bottom right corner}} = \mathbf{GROD}(\varepsilon^{\mathrm{p}}, -\gamma^{\mathrm{p}}, -\omega, \psi) = |-\omega + \sin 2\psi \cdot \varepsilon^{\mathrm{p}} + \cos 2\psi \cdot \gamma^{\mathrm{p}}| \ \text{Peak value} \tag{68}$$

4.3. Comparison of misorientation distributions between tension and buckling of smooth SC samples

Apart from grain boundaries and sample geometries, plastic strain modes (tension vs. buckling) also produce a significant influence on the local misorientation distribution of plastically deformed samples. As a comparison of final misorientation distributions between tension and buckling, SC sample #1 and PC sample #2 were plastically deformed under the tensile mode of Gatan Tester (#1was ruptured, #2 was interrupted), while SC samples #4, #5 and PC sample #6 were plastically buckled under the compressive mode of Gatan Tester, whose mechanical respond curves are shown in Fig. 12.

Fig. 13 shows orientation (Inverse Pole Figure) and misorientation (including $\mathbf{KAM}^{\text{obj}}$, $\mathbf{KAM}^{\text{I}}_{\text{GND}}$, $\mathbf{KAM}^{\text{II}}_{\text{GND}}$, $\mathbf{KAM}^{\text{III}}_{\text{GND}}$ and **GROD**) maps in five plastically deformed SC and PC samples. We used the distance covering 25 pixels (20um) as the step

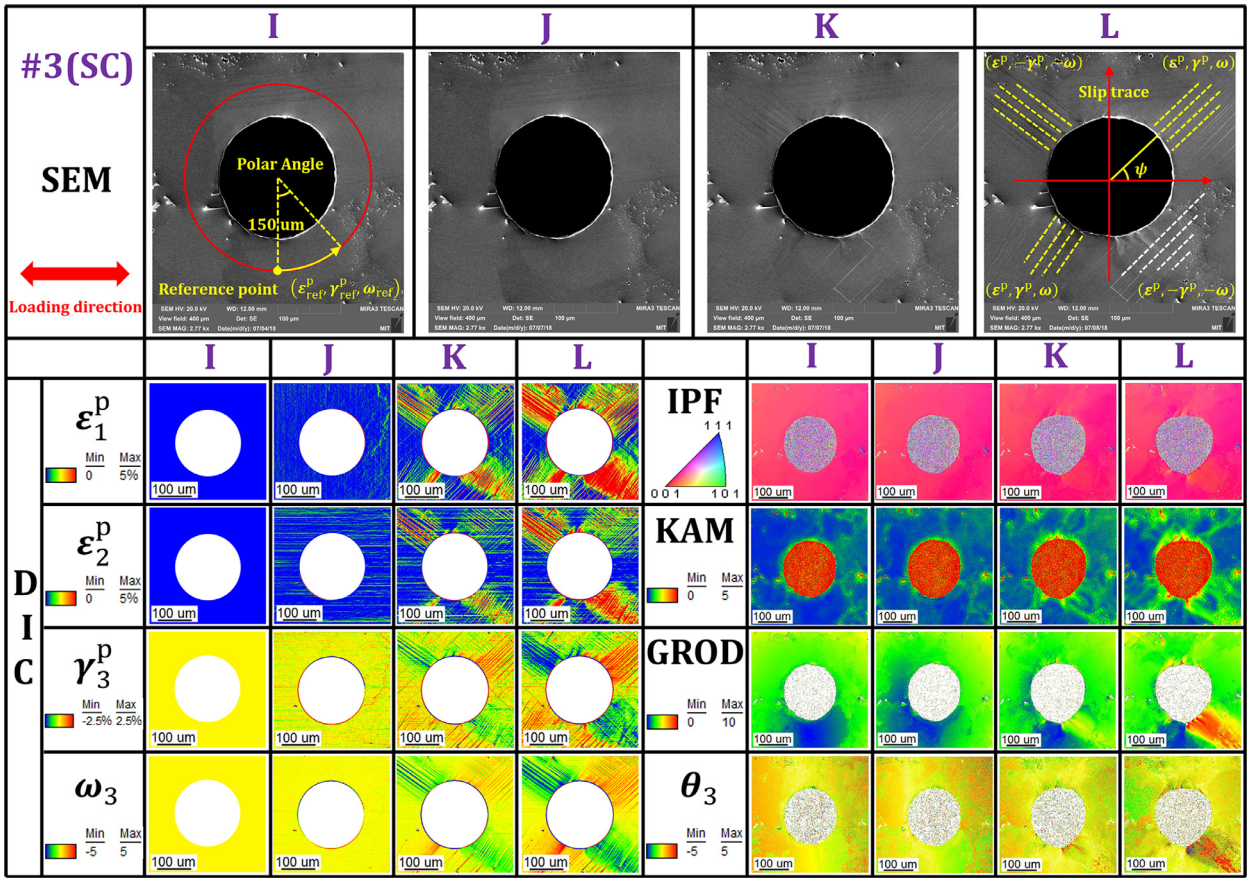

Fig. 9. Residual material distortion and local misorientation evolution in the SC sample #3.

size for **KAM** calculation, and selected the geometrical center of rectangular EBSD observational area in SC samples as well as the point with the lowest **KAM** value within each single grain in PC samples as the reference points for **GROD** calculation here. Both $\mathbf{KAM}^{\mathrm{obj}}$ and **GROD** values of the plastically buckled SC sample #4 are much higher than those of the SC sample #1 deformed under tensile mode, though the lattice orientations of two SC samples are the same. Here $\mathbf{KAM}^{\mathrm{obj}}$ is uniformly distributed in the EBSD observational area of SC sample #4, while the **GROD** value is low in the middle (close to the reference point) but high at the edge (far from the reference point). At the same time, the lattice rotation axes are mostly parallel to the material rotation axis in buckled SC sample #4 but orient randomly in tensile SC sample #1. With respect to the sub-parameters, $\mathbf{KAM}^{\mathrm{I}}_{\mathrm{GND}}$ of the SC sample #4 occupies the major part in $\mathbf{KAM}^{\mathrm{obj}}$ and is much higher than that of the SC sample #1, while $\mathbf{KAM}^{\mathrm{II}}_{\mathrm{GND}}$ and $\mathbf{KAM}^{\mathrm{III}}_{\mathrm{GND}}$ of the SC sample #4 occupy the minor parts in $\mathbf{KAM}^{\mathrm{obj}}$ and are close to those of the SC sample #1. It is because the first sub-GND density tensor $\boldsymbol{\rho}^{\mathrm{I}}_{\mathrm{GND}}$ plays a leading role in total $\boldsymbol{\rho}_{\mathrm{GND}}$ in the buckling but becomes negligible in the tension, as predicted by the Eqs. (47), (49), (52) and (54) in previous Section 3.4.

Then the vertical distribution curves of horizontally averaged **GROD** were calculated and then shown in Fig. 14. From the **GROD** maps of SC samples in Fig. 13 and their distribution curves in Fig. 14a we can see, buckled SC samples #4 presents a "V-type" symmetric gradient distribution on two sides of the reference point, while the tensile SC sample #1 presents a smooth distribution with low **GROD** value though its equivalent plastic strain is even higher. As to the SC samples #4 and #5 with similar buckling curvature degree but different lattice orientations, their "V-type" **GROD** distribution curves are almost overlapped with each other, which means the azimuthal angles of slip systems activated during buckling does not produce a significant influence on the slope of "V-type" **GROD** distribution near neutral surface, as predicted by the Eqs. (48) and (53) in previous Section 3.4.

Different from the obvious difference of final misorientation distributions between buckled SC sample #4 and tensile SC sample #1, the **GROD** map of buckled PC sample #6 in Fig. 13 and its distribution curve in Fig. 14b are similar to those of tensile PC sample #2. It is because the intragranular misorientation averaged over multiple grains in PC material is different from local misorientation in SC material. As pointed out theoretically in previous Section 3.5 and confirmed experimentally by Section 4.1, $\overline{\mathbf{GROD}}$ averaged within a representative region containing enough grains has the capability of characterizing the equivalent plastic strain. Meanwhile, the comparison between PC samples #6 and #2 here reveals that $\overline{\mathbf{GROD}}$ is not very sensitive to plastic strain modes.

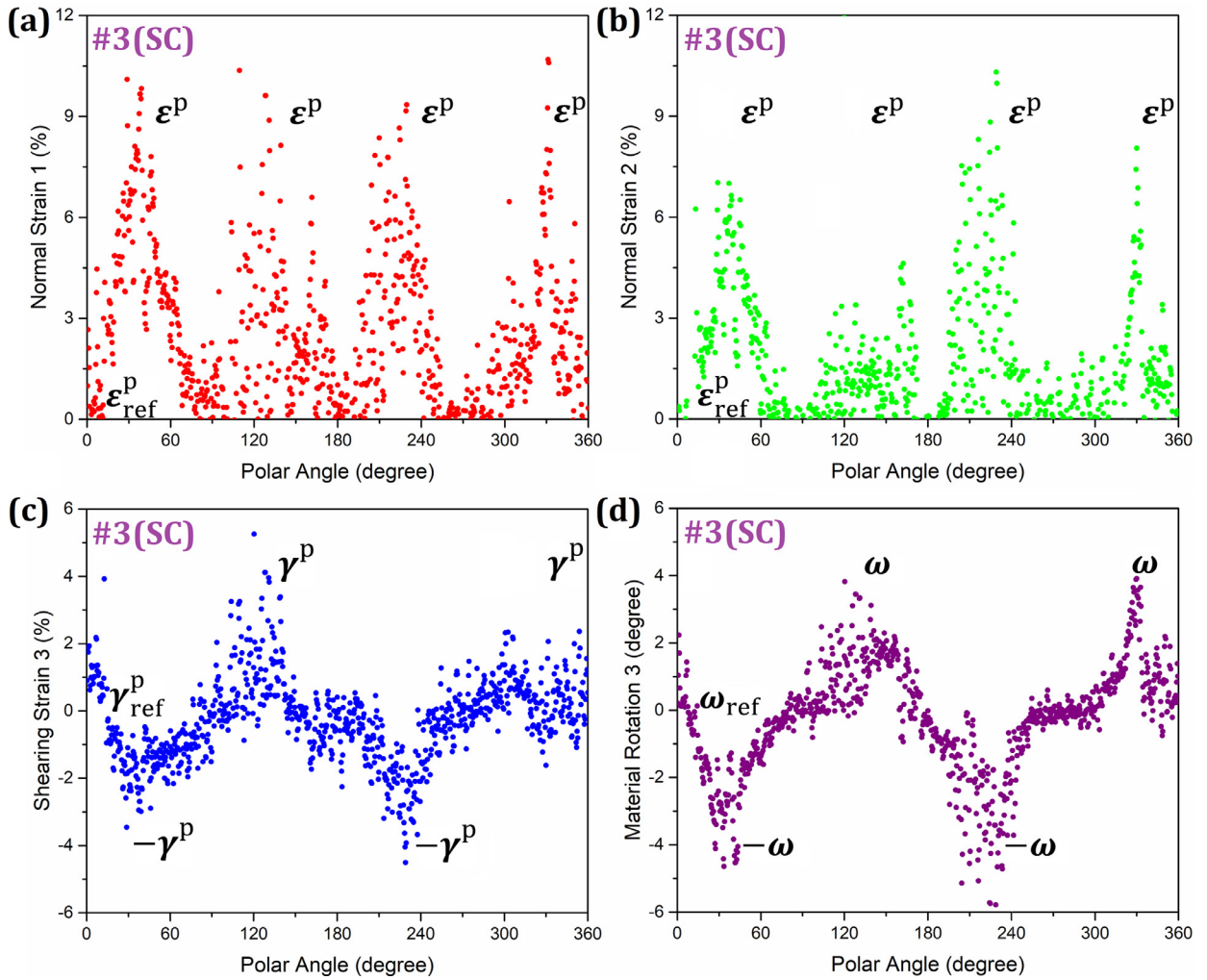

Fig. 10. Distribution of (a) normal plastic strain ε_1^p, (b) normal plastic strain ε_2^p, (c) shearing plastic strain γ_3^p and (d) material rotation ω_3 along the circuit in deformed case L (1120 MPa).

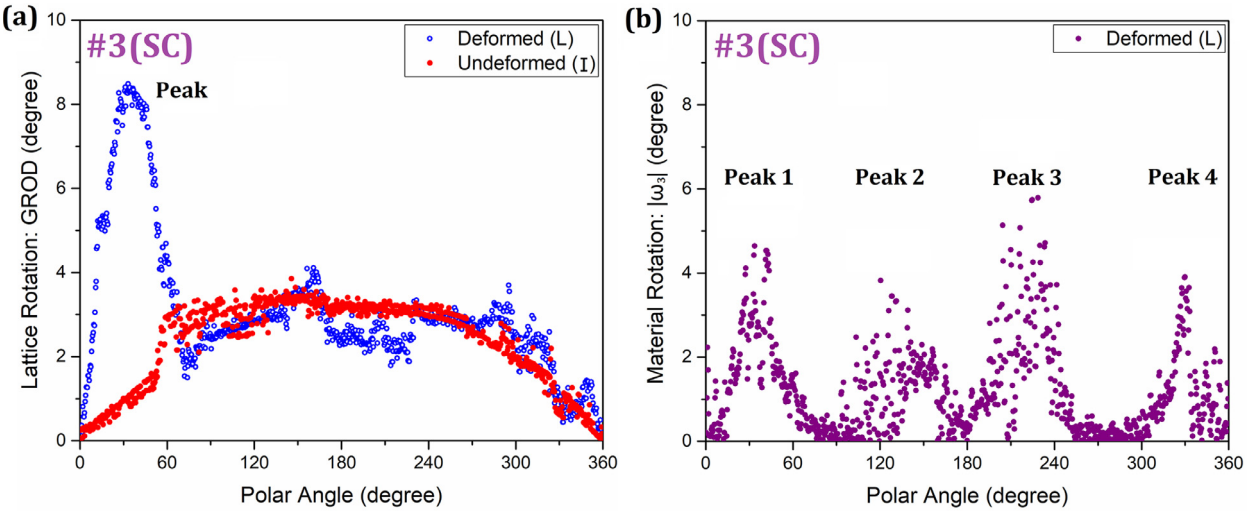

Fig. 11. Comparison between (a) relative lattice rotation: **GROD** and (b) absolute material rotation: $|\omega_3|$ distribution along the circuit in deformed case L (1120 MPa).

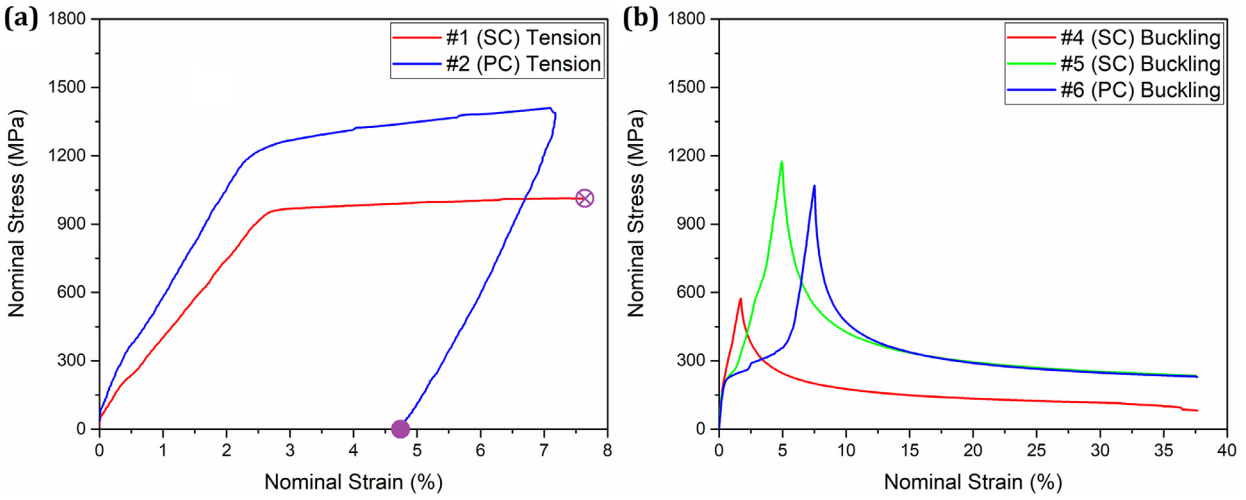

Fig. 12. Nominal stress — nominal strain curves of (a) the tensile samples #1 ~ #2 and (b) the buckled samples #4 ~ #6.

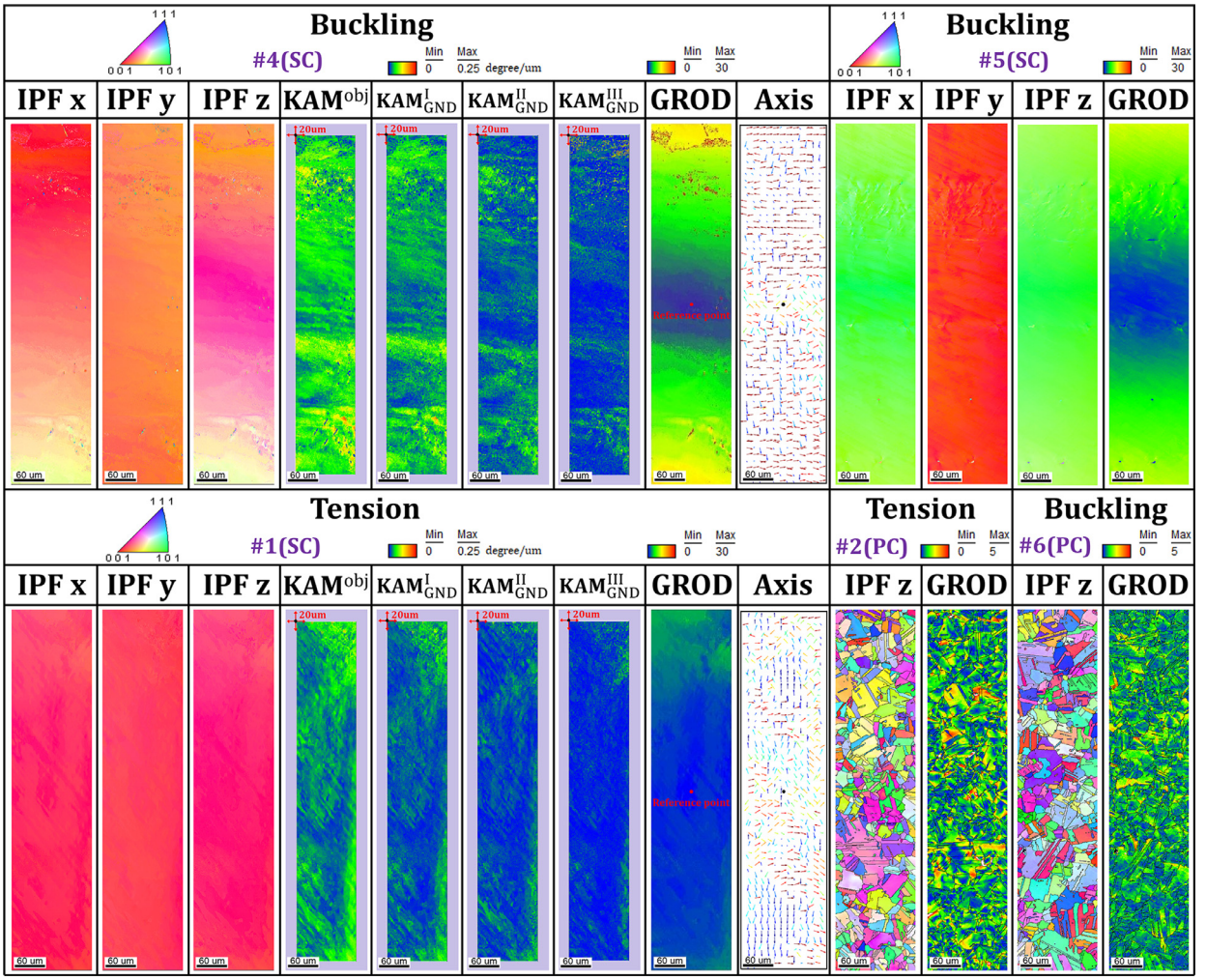

Fig. 13. Orientation (Inverse Pole Figure) and misorientation (**KAM**^{obj}, **KAM**$^{I}_{GND}$, **KAM**$^{II}_{GND}$, **KAM**$^{III}_{GND}$ and **GROD**) distributions in the tensile samples #1 ~ #2 and the buckled samples #4 ~ #6.

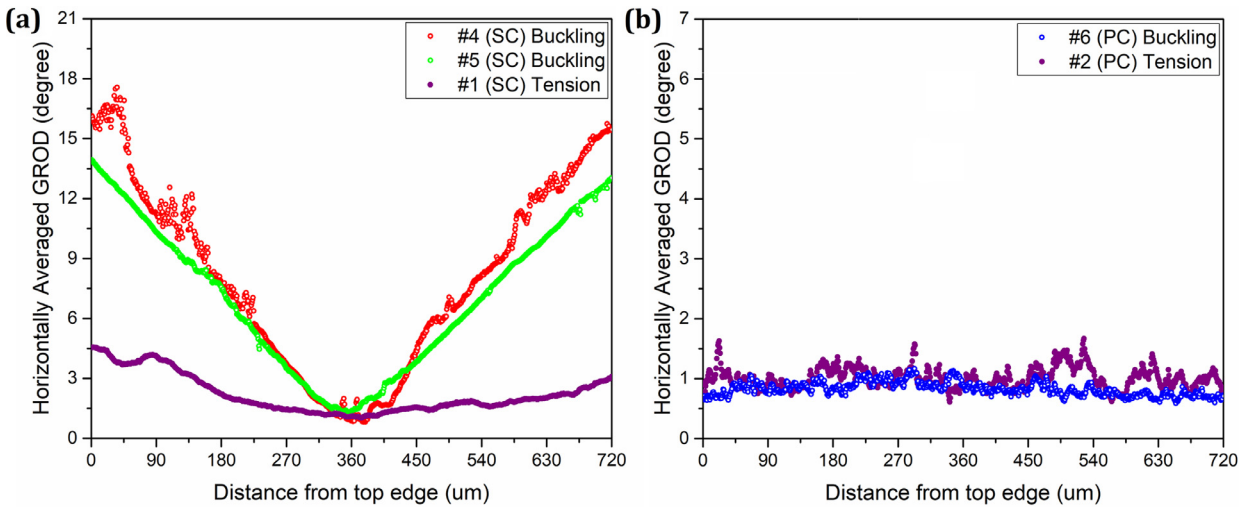

Fig. 14. Vertical distribution curves of horizontally averaged **GROD** in SC and PC samples after tension and buckling tests.

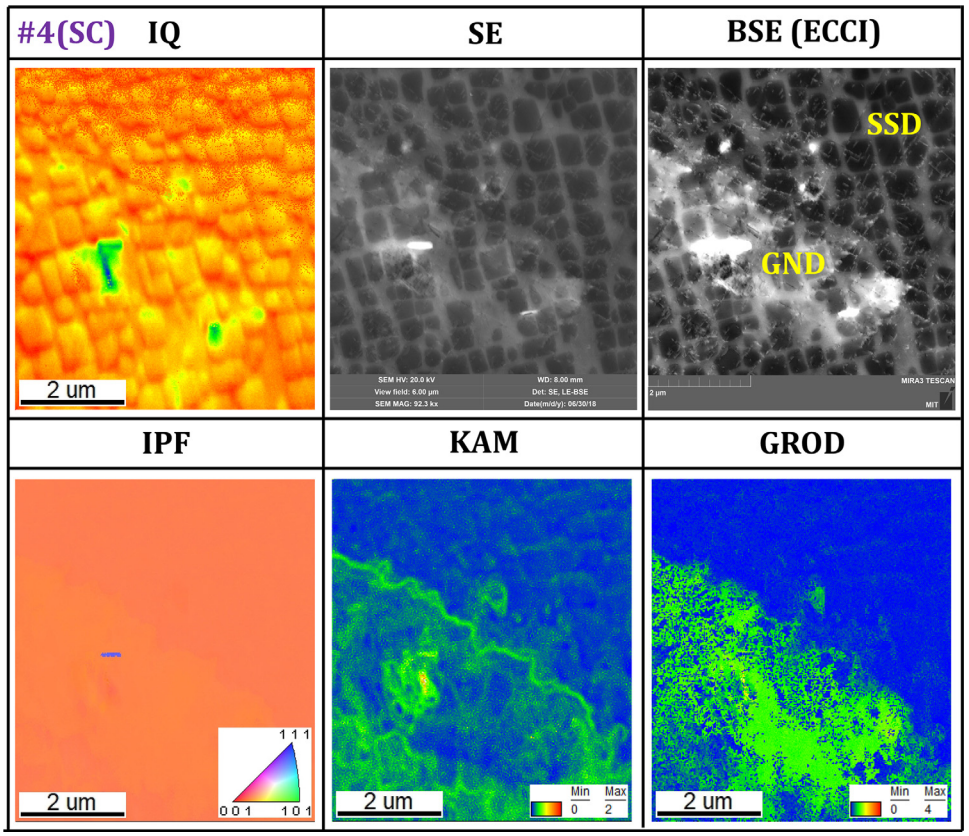

Fig. 15. True dislocations directly observed by ECCI and GND density indirectly evaluated by EBSD.

4.4. Comparison between true dislocations observed by ECCI and GND density evaluated by EBSD

Fig. 15 shows the comparison between true dislocations directly observed by ECCI technique and GND density distribution indirectly evaluated by diffraction-based misorientation mapping in buckled SC sample #4. The bottom left corner of the ECCI image looks very bright, while the upper right corner looks relatively dark. As mentioned before, the dislocation in BSE image looks bright in the dark background when the primary electron beam excites so-called “two-beam diffraction

condition". Therefore, the bright region in ECCI image is actually occupied by dense dislocations, while only a small quantity of discrete dislocation is distributed in the dark region. Accordingly, high misorientation value was captured in both **KAM** and **GROD** maps at the bright region shown in ECCI image, while low misorientation value was captured at the dark region.

As pointed out in previous Section 2.2.3, the GND density evaluated by EBSD only occupies a certain ratio of total true dislocations under the spatial resolution associated with scanning step size a. However, this ratio seems to be approximately constant when the scanning step size is determined. For example, Kubushiro et al. (2015) measured the GND density from **KAM** and true dislocation density from Transmission Electron Microscope (TEM) respectively in type SUS316L austenitic stainless steel under transient creep stage and found that they followed a linear relationship with each other. Therefore, **KAM** can still serve as the measure of true dislocation density as long as the step size keeps constant, though it only reflects the GND density actually. It should be pointed out that **GROD** does not have the capability of dislocation density characterization though its value also appeared very high in the bright area full of true dislocations. **GROD** only indirectly reflects the inhomogeneous lattice rotation distribution, i.e., orientation deviation induced by local GND pile up.

5. Conclusions

In this research, a continuum mechanics description of the relationship among lattice curvature (measured by 2D-EBSD), GND development (measured by ECCI) and material distortion (measured by μ-DIC) was made under the framework of two typical intragranular misorientation parameters **KAM** and **GROD**, widely used for diffraction-based misorientation maps. Combining with the experimental validation, the main conclusions are then highlighted in four points as follows:

(1) **KAM** theoretically turns out to result from three in-surface invariants ($\rho^{\mathrm{I}}_{\mathrm{GND}}$, $\rho^{\mathrm{II}}_{\mathrm{GND}}$ & $\rho^{\mathrm{III}}_{\mathrm{GND}}$) of GND density tensor $\boldsymbol{\rho}_{\mathrm{GND}}$ induced by plastic strain distribution incompatible with the activated slip systems in unloaded elastic-plastic condition, which cause the same lattice curvature effects as three elastic strain modes (buckling, in-surface bending & torsion) with non-zero curl in purely elastic condition. **KAM** does not reflect true dislocation density exactly, but the coupled EBSD and ECCI observations confirm that it serves as a qualitative description of true dislocations density distribution.

(2) **GROD** theoretically turns out to correspond to neither the local plastic strain ε^{p}, γ^{p}_{3} nor the local material rotation ω_3 alone in the in-plane deformed SC sample even if the ($\varepsilon^{\mathrm{p}}_{\mathrm{ref}}$, $\gamma^{\mathrm{p}}_{\mathrm{ref}}$, ω_{ref}) at the reference point is equal to zero, because the relationship between relative lattice rotation and material distortion is also influenced by the azimuthal angles φ_1, φ_2 of activated in-plane slip systems. The coupled EBSD and DIC observations indicate that **GROD** distribution differs from both local plastic strain and local material rotation distributions around the central hole of a tensile SC sample.

(3) Both **GROD** and **KAM** distributions in SC samples strongly rely on their plastic strain modes. **GROD** within a small region near the neutral surface presents a "V-type" distribution which theoretically turns out to be determined by the buckling curvature $1/r_0$ regardless of the azimuthal angles φ_1, φ_2 of activated slip systems in a buckled SC sample, but degenerates into a smooth distribution in a tensile SC sample. In addition, $\mathbf{KAM}^{\mathrm{I}}_{\mathrm{GND}}$ occupies the major part of $\mathbf{KAM}^{\mathrm{obj}}$ in buckling case but becomes negligible in tension case, which is consistent with the EBSD observation.

(4) Both $\overline{\mathbf{KAM}}$ and $\overline{\mathbf{GROD}}$ averaged over multiple grains increase with the nominal plastic strain applied in the PC material but keep almost constant in the SC material during the tensile deformation, which theoretically turn out to be attributed to the grain boundaries' constraint on lattice rotation. Meanwhile, $\overline{\mathbf{KAM}}$ is theoretically predicted to be proportional to the EBSD scanning step size a but inversely proportional to the grain size $\mathrm{D}_{\mathrm{Grain}}$, while $\overline{\mathbf{GROD}}$ is independent of the above two factors. Those agree with the EBSD observation results reported in this research or other literatures (Kamaya et al., 2005; Kamaya, 2011).

6. Acknowledgment

This research is financially supported by National Natural Science Foundation of China (Grant Nos. 11572171, 11632010, 11672151, 91860101), National Major Science and Technology Projects of China (Grant No. 2017-VI-0003-0073) and Tsinghua Scholarship for Overseas Graduate Studies (Contract No. 2017064). Dr. S. Mohadeseh Taheri-Mousavi, Mr. Benjamin Cameron and other colleagues from Prof. Tasan's Group at MIT are gratefully acknowledged for their contributions. In particular, a deep sense of gratitude also goes to my friends Mr. Zhihao Shang and Miss. Yan Li from Tsinghua University, for their help and support in applying for my visiting funding and J-1 visa.

Appendix I. Connection between GND density tensor and elastic & plastic incompatibility

The total deformation gradient tensor $\boldsymbol{F}$ maps the undeformed state of crystal to the deformed state, which can be multiplicatively decomposed into the elastic part $\boldsymbol{F}^{\mathrm{e}}$ and the plastic part $\boldsymbol{F}^{\mathrm{p}}$. Replacing the deformation gradient tensors $\boldsymbol{F}$, $\boldsymbol{F}^{\mathrm{e}}$ and $\boldsymbol{F}^{\mathrm{p}}$ by the distortion tensors $\mathbf{I}+\boldsymbol{\beta}$, $\mathbf{I}+\boldsymbol{\beta}^{\mathrm{e}}$ and $\mathbf{I}+\boldsymbol{\beta}^{\mathrm{p}}$ respectively ($\mathbf{I}$ is the metric tensor), we can then obtain the following Eq. (A1):

$$\boldsymbol{F}=\mathbf{I}+\boldsymbol{\beta}=\boldsymbol{F}^{\mathrm{e}}\cdot\boldsymbol{F}^{\mathrm{p}}=\left(\mathbf{I}+\boldsymbol{\beta}^{\mathrm{e}}\right)\cdot\left(\mathbf{I}+\boldsymbol{\beta}^{\mathrm{p}}\right)=\mathbf{I}+\boldsymbol{\beta}^{\mathrm{e}}+\boldsymbol{\beta}^{\mathrm{p}}+\boldsymbol{\beta}^{\mathrm{e}}\cdot\boldsymbol{\beta}^{\mathrm{p}} \tag{A1}$$

where the $\boldsymbol{\beta}^{\mathrm{e}}\cdot\boldsymbol{\beta}^{\mathrm{p}}$ item becomes negligible under small elastic-plastic deformation condition (Das et al., 2018). In this case, the total material distortion tensor $\boldsymbol{\beta}$ can be additively decomposed into elastic distortion part $\boldsymbol{\beta}^{\mathrm{e}}$ and plastic distortion part

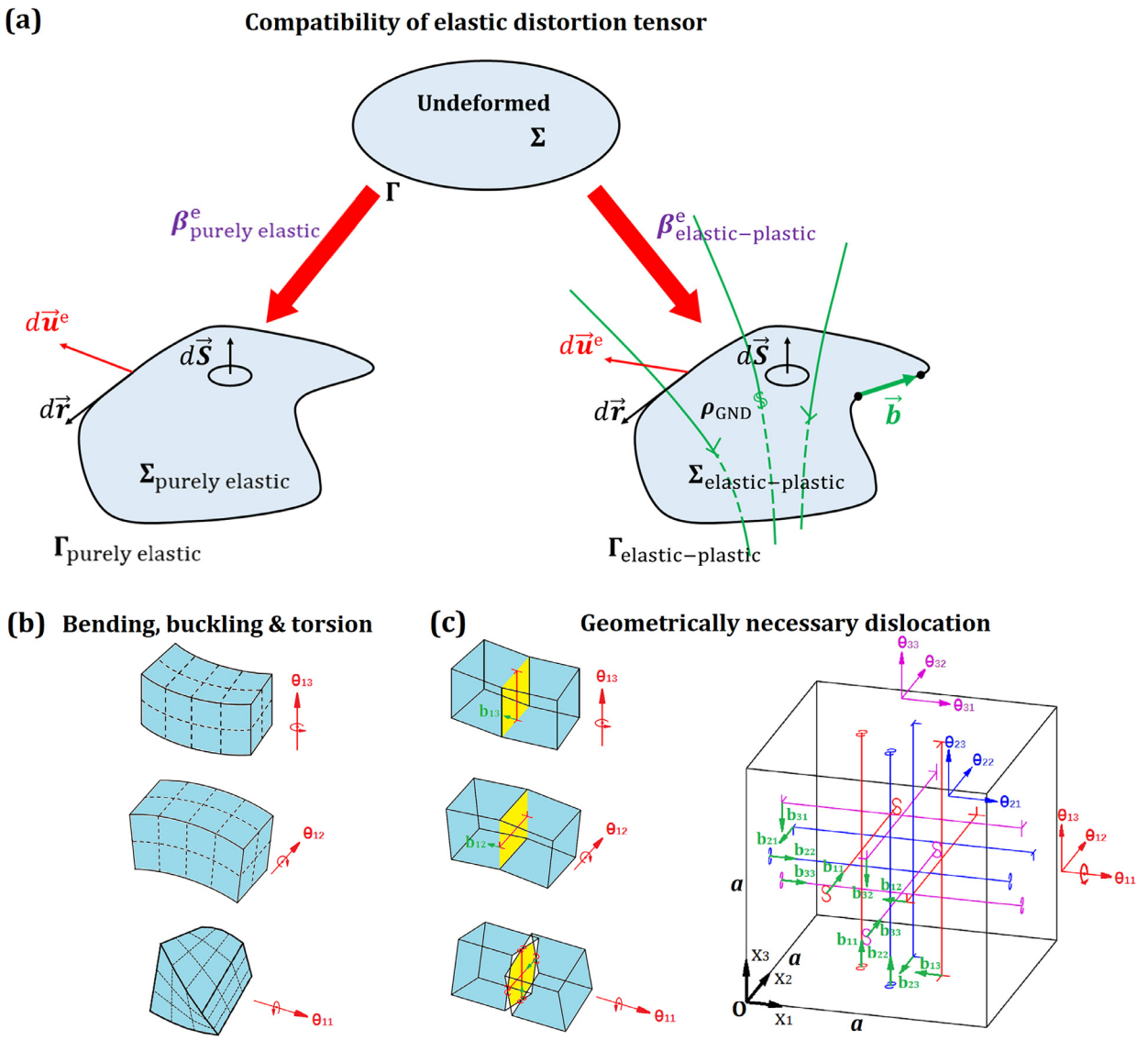

Fig. A1. (a) Compatibility of elastic distortion tensor $\boldsymbol{\beta}^{e}$ under purely elastic and elastic-plastic conditions, and orientation gradient induced by (b) elastic bending, buckling & torsion or (c) GND.

$\boldsymbol{\beta}^{p}$, which can be written as the following Eq. (A2):

$$\boldsymbol{\beta} = \boldsymbol{\beta}^{e} + \boldsymbol{\beta}^{p} \tag{A2}$$

Under purely elastic condition, the elastic distortion tensor $\boldsymbol{\beta}^{e}$ maps an enclosed circuit $\boldsymbol{\Gamma}$ to another enclosed circuit $\boldsymbol{\Gamma}_{\text{purely elastic}}$ without introducing any burgers vector. Thus, the circulatory integral of elastic displacement field $\vec{\boldsymbol{u}}^{e}$ is equal to zero as shown in Eq. (A3) and Fig. A1a (left-side). According to Stokes' law, the circulatory integral of elastic distortion $\boldsymbol{\beta}^{e}$ along circuit $\boldsymbol{\Gamma}_{\text{purely elastic}}$ can be transferred into the surface integral of $\boldsymbol{\beta}^{e} \times \nabla$ on the area $\boldsymbol{\Sigma}_{\text{purely elastic}}$ enclosed by the circuit, and thus the $\boldsymbol{\beta}^{e} \times \nabla$ item is also equal to zero. This type of elastic distortion tensor $\boldsymbol{\beta}^{e}$ is termed as "compatible", whose antisymmetric part $\boldsymbol{\Omega}_{\text{lattice}}$ can be completely removed after unloading.

$$\oint_{\Gamma}^{\text{purely elastic}} d\vec{\boldsymbol{u}}^{e} = \oint_{\Gamma}^{\text{purely elastic}} \boldsymbol{\beta}^{e} \cdot d\vec{\boldsymbol{r}} = \iint_{\Sigma}^{\text{purely elastic}} \boldsymbol{\beta}^{e} \times \nabla \cdot d\vec{\boldsymbol{S}} = \vec{0}, \;\; \boldsymbol{\beta}^{e} \times \nabla = 0 \tag{A3}$$

Under elastic-plastic condition, the burgers vector will gradually accumulate in the area $\boldsymbol{\Sigma}_{\text{elastic-plastic}}$ accompanied by different amounts of dislocations move-in and move-out, which leads to the appearance of plastic incompatibility especially

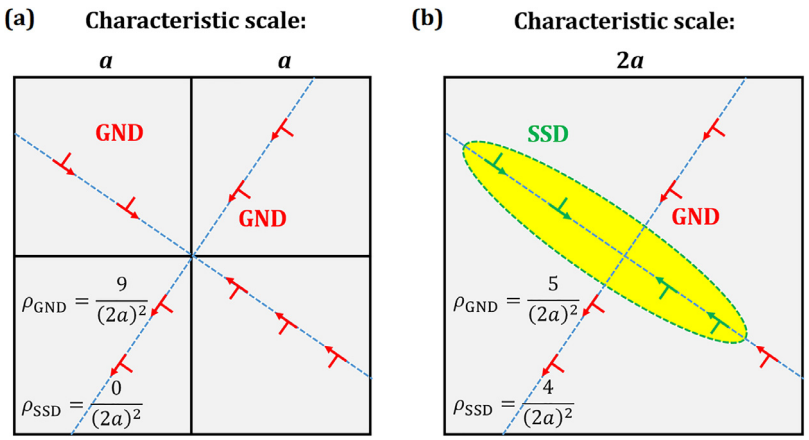

Fig. A2. Distinction between GND and SSD under different characteristic scales: (a) a and (b) $2a$.

in high strain gradient plasticity case (Kysar et al., 2007). Here the negative curl of plastic distortion tensor $\boldsymbol{\beta}^{\mathrm{p}}$ inside the area $\boldsymbol{\Sigma}_{\mathrm{elastic-plastic}}$ is defined as the local GND density tensor $\boldsymbol{\rho}_{\mathrm{GND}}$. With the appearance of plastic incompatibility in plastic distortion tensor $\boldsymbol{\beta}^{\mathrm{p}}$, the elastic incompatibility with the same magnitude but opposite symbol appears inevitably in elastic distortion tensor $\boldsymbol{\beta}^{\mathrm{e}}$ to keep the total material distortion tensor $\boldsymbol{\beta}$ compatible as shown in Eq. (A4), because none overlap or separation exists in the crystal during the elastic-plastic deformation.

$$\boldsymbol{\beta} \times \nabla \equiv 0,\ -\boldsymbol{\beta}^{\mathrm{p}} \times \nabla = \boldsymbol{\rho}_{\mathrm{GND}} \overset{\mathrm{def}}{=} \sum_{\alpha=1}^{k} \rho_{\mathrm{GND}}^{\alpha} \vec{\boldsymbol{b}}^{\alpha} \vec{\boldsymbol{t}}^{\alpha} = \begin{bmatrix} b_{11}^{\mathrm{s}} & b_{12}^{\mathrm{e}} & b_{13}^{\mathrm{e}} \\ b_{21}^{\mathrm{e}} & b_{22}^{\mathrm{s}} & b_{23}^{\mathrm{e}} \\ b_{31}^{\mathrm{e}} & b_{32}^{\mathrm{e}} & b_{33}^{\mathrm{s}} \end{bmatrix} = \boldsymbol{\beta}^{\mathrm{e}} \times \nabla \tag{A4}$$

where the vectors $\vec{\boldsymbol{b}}^{\alpha}$ and $\vec{\boldsymbol{t}}^{\alpha}$ represent burgers vector and dislocation unit line vector of the α^{th} type GND respectively. The GND density tensor $\boldsymbol{\rho}_{\mathrm{GND}}$ contains nine independent components in total, and six items (b_{12}^{e}, b_{21}^{e}, b_{13}^{e}, b_{23}^{e}, b_{33}^{s} and $b_{11}^{\mathrm{s}} - b_{22}^{\mathrm{s}}$) are measurable by 2D-EBSD while the remaining items (b_{31}^{e}, b_{32}^{e} and $b_{11}^{\mathrm{s}} + b_{22}^{\mathrm{s}}$) are measurable by 3D-EBSD if the contribution of elastic strain curl $\boldsymbol{\varepsilon}^{\mathrm{e}} \times \nabla$ to the lattice curvature was ignored (Pantleon, 2008). Thus the density $\rho_{\mathrm{GND}}^{\alpha}$ of the α^{th} type GND can be uniquely determined by 2D-EBSD when the total activated GND types number k is no more than six, or by 3D-EBSD when k is no more than nine, otherwise the solutions of $\rho_{\mathrm{GND}}^{\alpha}$ ($\alpha = 1 \cdots k$) are non-unique. For the latter, B.S. El-Dasher, S. Sun and B.L. Adams (El-Dasher et al., 2003; Sun et al., 2000; Sun et al., 1998) suggested the minimized $\sum_{\alpha=1}^{k} \rho_{\mathrm{GND}}^{\alpha}$ (lowest dislocation density) while A.J. Wilkinson (Wallis et al., 2016; Wilkinson and Randman, 2010) suggested the minimized $\sum_{\alpha=1}^{k} E^{\alpha} \rho_{\mathrm{GND}}^{\alpha}$ (lowest dislocation energy) as an additional criterion to determine the density $\rho_{\mathrm{GND}}^{\alpha}$ of the α^{th} type GND uniquely. Here E^{α} is the unit line energy for edge dislocation ($E_{\mathrm{e}}^{\alpha} \propto \vec{\boldsymbol{b}}^{\alpha} \cdot \vec{\boldsymbol{b}}^{\alpha}$) and screw dislocation ($E_{\mathrm{s}}^{\alpha} \propto \vec{\boldsymbol{b}}^{\alpha} \cdot \vec{\boldsymbol{b}}^{\alpha}/(1-\nu)$, ν is Poisson's ratio). Compared with **KAM** only reflecting the invariants $\rho_{\mathrm{GND}}^{\mathrm{I}}$, $\rho_{\mathrm{GND}}^{\mathrm{II}}$ & $\rho_{\mathrm{GND}}^{\mathrm{III}}$ of GND density tensor $\boldsymbol{\rho}_{\mathrm{GND}}$, total GND density $\sum_{\alpha=1}^{k} \rho_{\mathrm{GND}}^{\alpha}$ determined by EBSD based on minimization criterion is closer to but still lower than true dislocations density observed by ECCI. Due to the limited EBSD spatial resolution, SSD stored within EBSD step size cannot be identified from lattice curvature, as shown in Fig A2.

In this case, the circulatory integral of elastic distortion $\boldsymbol{\beta}^{\mathrm{e}}$ along circuit $\boldsymbol{\Gamma}_{\mathrm{elastic-plastic}}$ can also be transferred into the surface integral of non-zero elastic incompatibility $\boldsymbol{\beta}^{\mathrm{e}} \times \nabla$ (i.e. $\boldsymbol{\rho}_{\mathrm{GND}}$) on the area $\boldsymbol{\Sigma}_{\mathrm{elastic-plastic}}$ enclosed by the circuit. However, the circulatory integral of elastic displacement field $\vec{\boldsymbol{u}}^{\mathrm{e}}$ is no longer equal to zero as shown in Eq. (A5) and Fig. A1a (right-side), because the elastic distortion tensor $\boldsymbol{\beta}^{\mathrm{e}}$ here maps an enclosed circuit $\boldsymbol{\Gamma}$ to another open circuit $\boldsymbol{\Gamma}_{\mathrm{elastic-plastic}}$ by introducing the total burgers vector $\vec{\boldsymbol{b}}$. This type of elastic distortion tensor $\boldsymbol{\beta}^{\mathrm{e}}$ is termed as "incompatible", whose antisymmetric part $\boldsymbol{\Omega}_{\mathrm{lattice}}$ cannot be completely removed after unloading.

$$\boldsymbol{\beta}^{\mathrm{e}} \times \nabla = \boldsymbol{\rho}_{\mathrm{GND}},\ \oint_{\Gamma}^{\mathrm{elastic-plastic}} d\vec{\boldsymbol{u}}^{\mathrm{e}} = \oint_{\Gamma}^{\mathrm{elastic-plastic}} \boldsymbol{\beta}^{\mathrm{e}} \cdot d\vec{\boldsymbol{r}} = \iint_{\Sigma}^{\mathrm{elastic-plastic}} \boldsymbol{\beta}^{\mathrm{e}} \times \nabla \cdot d\vec{\boldsymbol{S}} = \vec{\boldsymbol{b}} \tag{A5}$$

Appendix II. Contribution of elastic strain curl & plastic incompatibility to lattice curvature

The EBSD measurable misorientation information is stored in the lattice rotation item $\boldsymbol{\Omega}_{\mathrm{lattice}}$ rather than the non-lattice rotation item $\boldsymbol{\Omega}_{\mathrm{non-lattice}}$. Here $\boldsymbol{\Omega}_{\mathrm{lattice}}$ is an antisymmetric tensor containing three independent components (mentioned in Eq. (6)), as shown in Eq. (A6) together with its curl $\boldsymbol{\Omega}_{\mathrm{lattice}} \times \nabla$ and the orientation gradient tensor $\boldsymbol{\kappa}$ (mentioned in Eq. (7))

having nine components.

$$\boldsymbol{\Omega}_{\text{lattice}}=\begin{bmatrix}0 & \theta_3 & -\theta_2\\ -\theta_3 & 0 & \theta_1\\ \theta_2 & -\theta_1 & 0\end{bmatrix},\ \boldsymbol{\Omega}_{\text{lattice}}\times\nabla=\begin{bmatrix}\dfrac{\partial\theta_2}{\partial x_2}+\dfrac{\partial\theta_3}{\partial x_3} & -\dfrac{\partial\theta_2}{\partial x_1} & -\dfrac{\partial\theta_3}{\partial x_1}\\ -\dfrac{\partial\theta_1}{\partial x_2} & \dfrac{\partial\theta_3}{\partial x_3}+\dfrac{\partial\theta_1}{\partial x_1} & -\dfrac{\partial\theta_3}{\partial x_2}\\ -\dfrac{\partial\theta_1}{\partial x_3} & -\dfrac{\partial\theta_2}{\partial x_3} & \dfrac{\partial\theta_1}{\partial x_1}+\dfrac{\partial\theta_2}{\partial x_2}\end{bmatrix},$$

$$\boldsymbol{\kappa}=\begin{bmatrix}\dfrac{\partial\theta_1}{\partial x_1} & \dfrac{\partial\theta_1}{\partial x_2} & \dfrac{\partial\theta_1}{\partial x_3}\\ \dfrac{\partial\theta_2}{\partial x_1} & \dfrac{\partial\theta_2}{\partial x_2} & \dfrac{\partial\theta_2}{\partial x_3}\\ \dfrac{\partial\theta_3}{\partial x_1} & \dfrac{\partial\theta_3}{\partial x_2} & \dfrac{\partial\theta_3}{\partial x_3}\end{bmatrix} \tag{A6}$$

Based on the listed components of lattice rotation curl $\boldsymbol{\Omega}_{\text{lattice}}\times\nabla$ and orientation gradient tensor $\boldsymbol{\kappa}$, it is easy to verify that the orientation gradient tensor $\boldsymbol{\kappa}$ can be expressed as $\frac{1}{2}[(\boldsymbol{\Omega}_{\text{lattice}}\times\nabla):\mathbf{I}]\mathbf{I}-(\boldsymbol{\Omega}_{\text{lattice}}\times\nabla)^{\mathrm{T}}$. Replacing the $\boldsymbol{\Omega}_{\text{lattice}}\times\nabla$ by $\boldsymbol{\rho}_{\text{GND}}-\boldsymbol{\varepsilon}^{\mathrm{e}}\times\nabla$ according to the calculation method of dislocation density tensor $\boldsymbol{\rho}_{\text{GND}}=\boldsymbol{\beta}^{\mathrm{e}}\times\nabla=\boldsymbol{\Omega}_{\text{lattice}}\times\nabla+\boldsymbol{\varepsilon}^{\mathrm{e}}\times\nabla$, we can obtain the contribution of elastic strain curl and plastic incompatibility to lattice curvature as Eq. (A7):

$$\boldsymbol{\kappa}=\frac{1}{2}[(\boldsymbol{\Omega}_{\text{lattice}}\times\nabla):\mathbf{I}]\mathbf{I}-(\boldsymbol{\Omega}_{\text{lattice}}\times\nabla)^{\mathrm{T}}=\left\{\frac{1}{2}\underbrace{[(-\boldsymbol{\varepsilon}^{\mathrm{e}}\times\nabla):\mathbf{I}]}_{=0}\mathbf{I}-(-\boldsymbol{\varepsilon}^{\mathrm{e}}\times\nabla)^{\mathrm{T}}\right\}+\left[\frac{1}{2}(\boldsymbol{\rho}_{\text{GND}}:\mathbf{I})\mathbf{I}-\boldsymbol{\rho}_{\text{GND}}^{\mathrm{T}}\right] \tag{A7}$$

Here the elastic strain $\boldsymbol{\varepsilon}^{\mathrm{e}}$ is a symmetric tensor containing six independent components, which is directly associated with applied stress $\boldsymbol{\sigma}$, as shown in Eq. (A8) together with its curl $\boldsymbol{\varepsilon}^{\mathrm{e}}\times\nabla$ having nine components. In particular, the trace of the elastic strain curl $(\boldsymbol{\varepsilon}^{\mathrm{e}}\times\nabla)$: $\mathbf{I}$ is identically equal to zero. Therefore, the formula shown in Eq. (A7) can be further simplified to the formula shown in the Eq. (16).

$$\boldsymbol{\varepsilon}^{\mathrm{e}}=\begin{bmatrix}\varepsilon_1^{\mathrm{e}} & \gamma_3^{\mathrm{e}} & \gamma_2^{\mathrm{e}}\\ \gamma_3^{\mathrm{e}} & \varepsilon_2^{\mathrm{e}} & \gamma_1^{\mathrm{e}}\\ \gamma_2^{\mathrm{e}} & \gamma_1^{\mathrm{e}} & \varepsilon_3^{\mathrm{e}}\end{bmatrix},\ \boldsymbol{\varepsilon}^{\mathrm{e}}\times\nabla=\begin{bmatrix}-\dfrac{\partial\gamma_2^{\mathrm{e}}}{\partial x_2}+\dfrac{\partial\gamma_3^{\mathrm{e}}}{\partial x_3} & -\dfrac{\partial\varepsilon_1^{\mathrm{e}}}{\partial x_3}+\dfrac{\partial\gamma_2^{\mathrm{e}}}{\partial x_1} & \dfrac{\partial\varepsilon_1^{\mathrm{e}}}{\partial x_2}-\dfrac{\partial\gamma_3^{\mathrm{e}}}{\partial x_1}\\ \dfrac{\partial\varepsilon_2^{\mathrm{e}}}{\partial x_3}-\dfrac{\partial\gamma_1^{\mathrm{e}}}{\partial x_2} & -\dfrac{\partial\gamma_3^{\mathrm{e}}}{\partial x_3}+\dfrac{\partial\gamma_1^{\mathrm{e}}}{\partial x_1} & -\dfrac{\partial\varepsilon_2^{\mathrm{e}}}{\partial x_1}+\dfrac{\partial\gamma_3^{\mathrm{e}}}{\partial x_2}\\ -\dfrac{\partial\varepsilon_3^{\mathrm{e}}}{\partial x_2}+\dfrac{\partial\gamma_1^{\mathrm{e}}}{\partial x_3} & \dfrac{\partial\varepsilon_3^{\mathrm{e}}}{\partial x_1}-\dfrac{\partial\gamma_2^{\mathrm{e}}}{\partial x_3} & -\dfrac{\partial\gamma_1^{\mathrm{e}}}{\partial x_1}+\dfrac{\partial\gamma_2^{\mathrm{e}}}{\partial x_2}\end{bmatrix},\ (\boldsymbol{\varepsilon}^{\mathrm{e}}\times\nabla):\mathbf{I}=0 \tag{A8}$$

Then the contribution of elastic strain components gradient $\partial\varepsilon_i^{\mathrm{e}}/\partial x_j$ and $\partial\gamma_i^{\mathrm{e}}/\partial x_j$, as well as GND density tensor components $b_{ij}^{\mathrm{e}}(i\neq j)$ and $b_{ij}^{\mathrm{s}}(i=j)$ to orientation gradient components $\partial\theta_i/\partial x_j$ is shown in Eq. (A9) by writing the $\boldsymbol{\varepsilon}^{\mathrm{e}}\times\nabla$ and $\boldsymbol{\rho}_{\text{GND}}$ explicitly in terms of components, which is the same as the result given in Ref. (Wilkinson and Randman, 2010). For purely elastic and unloaded elastic-plastic conditions, the right and left items can be accordingly neglected, and the Eq. (A9) degenerates into Eqs. (17) and (18) respectively.

$$\boldsymbol{\kappa}=\overbrace{\begin{bmatrix}-\dfrac{\partial\gamma_2^{\mathrm{e}}}{\partial x_2}+\dfrac{\partial\gamma_3^{\mathrm{e}}}{\partial x_3} & \dfrac{\partial\varepsilon_2^{\mathrm{e}}}{\partial x_3}-\dfrac{\partial\gamma_1^{\mathrm{e}}}{\partial x_2} & -\dfrac{\partial\varepsilon_3^{\mathrm{e}}}{\partial x_2}+\dfrac{\partial\gamma_1^{\mathrm{e}}}{\partial x_3}\\ -\dfrac{\partial\varepsilon_1^{\mathrm{e}}}{\partial x_3}+\dfrac{\partial\gamma_2^{\mathrm{e}}}{\partial x_1} & -\dfrac{\partial\gamma_3^{\mathrm{e}}}{\partial x_3}+\dfrac{\partial\gamma_1^{\mathrm{e}}}{\partial x_1} & \dfrac{\partial\varepsilon_3^{\mathrm{e}}}{\partial x_1}-\dfrac{\partial\gamma_2^{\mathrm{e}}}{\partial x_3}\\ \dfrac{\partial\varepsilon_1^{\mathrm{e}}}{\partial x_2}-\dfrac{\partial\gamma_3^{\mathrm{e}}}{\partial x_1} & -\dfrac{\partial\varepsilon_2^{\mathrm{e}}}{\partial x_1}+\dfrac{\partial\gamma_3^{\mathrm{e}}}{\partial x_2} & -\dfrac{\partial\gamma_1^{\mathrm{e}}}{\partial x_1}+\dfrac{\partial\gamma_2^{\mathrm{e}}}{\partial x_2}\end{bmatrix}}^{(\boldsymbol{\varepsilon}^{\mathrm{e}}\times\nabla)^{\mathrm{T}}}+\overbrace{\begin{bmatrix}\frac{b_{22}^{\mathrm{s}}+b_{33}^{\mathrm{s}}-b_{11}^{\mathrm{s}}}{2} & -b_{21}^{\mathrm{e}} & -b_{31}^{\mathrm{e}}\\ -b_{12}^{\mathrm{e}} & \frac{b_{33}^{\mathrm{s}}+b_{11}^{\mathrm{s}}-b_{22}^{\mathrm{s}}}{2} & -b_{32}^{\mathrm{e}}\\ -b_{13}^{\mathrm{e}} & -b_{23}^{\mathrm{e}} & \frac{b_{11}^{\mathrm{s}}+b_{22}^{\mathrm{s}}-b_{33}^{\mathrm{s}}}{2}\end{bmatrix}}^{\frac{1}{2}(\boldsymbol{\rho}_{\text{GND}}:\mathbf{I})\mathbf{I}-\boldsymbol{\rho}_{\text{GND}}^{\mathrm{T}}} \tag{A9}$$

Appendix III. Connection between residual material distortion and residual lattice rotation

According to the Eq. (19) shown in the above Section 3.1, the residual lattice rotation $\tilde{\boldsymbol{\Omega}}_{\text{lattice}}$ associated with the GND density distribution will be remained in the total residual material distortion $\tilde{\boldsymbol{\beta}}$ after unloading due to the existence of plastic incompatible during the elastic-plastic deformation. However, the residual lattice rotation $\tilde{\boldsymbol{\Omega}}_{\text{lattice}}(\tilde{\boldsymbol{\beta}})$ and non-lattice rotation $\tilde{\boldsymbol{\Omega}}_{\text{non-lattice}}(\tilde{\boldsymbol{\beta}})$ cannot be decoupled from the total material rotation $\boldsymbol{\Omega}_{\text{material}}(\tilde{\boldsymbol{\beta}})$, which should be attributed to lacking of activated slip systems information. In the 3D case, at least five independent slip systems $(\bar{\boldsymbol{s}}^1,\bar{\boldsymbol{n}}^1)\sim(\bar{\boldsymbol{s}}^5,\bar{\boldsymbol{n}}^5)$ should be activated to undertake any status of plastic strain $\boldsymbol{\varepsilon}^{\mathrm{p}}(\tilde{\boldsymbol{\beta}})$ with five independent components γ_1^{p}, γ_2^{p}, γ_3^{p}, $\varepsilon_1^{\mathrm{p}}$, $\varepsilon_2^{\mathrm{p}}$ (invariable volume : $\varepsilon_3^{\mathrm{p}}=-\varepsilon_1^{\mathrm{p}}-\varepsilon_2^{\mathrm{p}}$), where the unit vectors $\bar{\boldsymbol{s}}^{\alpha}$ and $\bar{\boldsymbol{n}}^{\alpha}$ represent the slip direction and the normal direction respectively of the α^{th} slip system. Then the Eq. (A10) containing eight unknown quantities (five slip amounts: $\gamma_1\sim\gamma_5$,

three residual lattice rotation components: $\theta_1 \sim \theta_3$) and eight known quantities (five plastic strain components γ_1^p, γ_2^p, γ_3^p, ε_1^p, ε_2^p, three material rotation components: $\omega_1 \sim \omega_3$) can be established. If the activated slip systems number is more than five, the unknown quantities number will be more than known quantities number and then the solutions of Eq. (A10) will be non-unique. Therefore, the same as the above lowest dislocation density or lowest dislocation energy criterions used for determining the GND density, minimized activated slip systems number assumption was made here to ensure the solution uniqueness of Eq. (A10).

$$\boldsymbol{\beta}^p\left(\tilde{\boldsymbol{\beta}}\right) + \tilde{\boldsymbol{\Omega}}_{\text{lattice}}\left(\tilde{\boldsymbol{\beta}}\right) = \left(\gamma_1 \vec{\boldsymbol{s}}^1\vec{\boldsymbol{n}}^1 + \gamma_2 \vec{\boldsymbol{s}}^2\vec{\boldsymbol{n}}^2 + \gamma_3 \vec{\boldsymbol{s}}^3\vec{\boldsymbol{n}}^3 + \gamma_4 \vec{\boldsymbol{s}}^4\vec{\boldsymbol{n}}^4 + \gamma_5 \vec{\boldsymbol{s}}^5\vec{\boldsymbol{n}}^5\right) + \begin{bmatrix} 0 & \theta_3 & -\theta_2 \\ -\theta_3 & 0 & \theta_1 \\ \theta_2 & -\theta_1 & 0 \end{bmatrix} = \tilde{\boldsymbol{\beta}}$$
$$= \begin{bmatrix} \varepsilon_1^p & \gamma_3^p + \omega_3 & \gamma_2^p - \omega_2 \\ \gamma_3^p - \omega_3 & \varepsilon_2^p & \gamma_1^p + \omega_1 \\ \gamma_2^p + \omega_2 & \gamma_1^p - \omega_1 & -\varepsilon_1^p - \varepsilon_2^p \end{bmatrix} \tag{A10}$$

To further simplify the problem, we only discuss the 2D plastic distortion $\boldsymbol{\beta}^p(\tilde{\boldsymbol{\beta}})$ made up of in-plane slip (both the slip direction $\vec{\boldsymbol{s}}^\alpha$ and the normal direction $\vec{\boldsymbol{n}}^\alpha$ are located in plane). In this case, at least two independent non-orthogonal slip systems $(\vec{\boldsymbol{s}}^1, \vec{\boldsymbol{n}}^1)$ and $(\vec{\boldsymbol{s}}^2, \vec{\boldsymbol{n}}^2)$ should be activated to undertake any status of in-plane plastic strain $\boldsymbol{\varepsilon}^p(\tilde{\boldsymbol{\beta}})$ with two independent components γ_3^p, ε^p(invariable volume : $\varepsilon_2^p = -\varepsilon_1^p = \varepsilon^p$). The azimuthal angle between $\vec{\boldsymbol{s}}^\alpha$ and axis $\vec{\boldsymbol{e}}_1$ is recorded as φ_α ($|\varphi_1 - \varphi_2| \neq \pi/2$), and the unit vectors $\vec{\boldsymbol{s}}^\alpha$ and $\vec{\boldsymbol{n}}^\alpha$ can be decomposed into $s_1^\alpha\vec{\boldsymbol{e}}_1 + s_2^\alpha\vec{\boldsymbol{e}}_2$ and $n_1^\alpha\vec{\boldsymbol{e}}_1 + n_2^\alpha\vec{\boldsymbol{e}}_2$ respectively under the current 2D coordinate system $(\vec{\boldsymbol{e}}_1, \vec{\boldsymbol{e}}_2)$, where s_β^α and n_β^α are the directional cosine of the slip direction and the normal direction respectively: $s_1^\alpha = \cos\varphi_\alpha$, $s_2^\alpha = \sin\varphi_\alpha$, $n_1^\alpha = -\sin\varphi_\alpha$ and $n_2^\alpha = \cos\varphi_\alpha$. As the major part of residual material distortion tensor $\tilde{\boldsymbol{\beta}}$, the plastic distortion tensor $\boldsymbol{\beta}^p(\tilde{\boldsymbol{\beta}})$ is made up of the slip amounts γ_1 and γ_2 in two activated slip systems, whose components under the current 2D coordinate system $(\vec{\boldsymbol{e}}_1, \vec{\boldsymbol{e}}_2)$ are shown in Eq. (A11):

$$\boldsymbol{\beta}^p\left(\tilde{\boldsymbol{\beta}}\right) = \gamma_1\vec{\boldsymbol{s}}^1\vec{\boldsymbol{n}}^1 + \gamma_2\vec{\boldsymbol{s}}^2\vec{\boldsymbol{n}}^2 = \gamma_1\left(s_1^1\vec{\boldsymbol{e}}_1 + s_2^1\vec{\boldsymbol{e}}_2\right)\left(n_1^1\vec{\boldsymbol{e}}_1 + n_2^1\vec{\boldsymbol{e}}_2\right) + \gamma_2\left(s_1^2\vec{\boldsymbol{e}}_1 + s_2^2\vec{\boldsymbol{e}}_2\right)\left(n_1^2\vec{\boldsymbol{e}}_1 + n_2^2\vec{\boldsymbol{e}}_2\right)$$
$$= \left(\gamma_1 s_1^1 n_1^1 + \gamma_2 s_1^2 n_1^2\right)\vec{\boldsymbol{e}}_1\vec{\boldsymbol{e}}_1 + \left(\gamma_1 s_1^1 n_2^1 + \gamma_2 s_1^2 n_2^2\right)\vec{\boldsymbol{e}}_1\vec{\boldsymbol{e}}_2 + \left(\gamma_1 s_2^1 n_1^1 + \gamma_2 s_2^2 n_1^2\right)\vec{\boldsymbol{e}}_2\vec{\boldsymbol{e}}_1 + \left(\gamma_1 s_2^1 n_2^1 + \gamma_2 s_2^2 n_2^2\right)\vec{\boldsymbol{e}}_2\vec{\boldsymbol{e}}_2 \tag{A11}$$

If the 2D residual material distortion $\tilde{\boldsymbol{\beta}}$ and the azimuthal angles φ_1, φ_2 of two independent activated slip systems were given in advance, we can establish the following Eq. (A12) with three unknown quantities (two slip amounts γ_1, γ_2, one residual lattice rotation component θ_3) and three known quantities (two plastic strain components γ_3^p, $\varepsilon_1^p = -\varepsilon_2^p = \varepsilon^p$, one material rotation component ω_3).

$$\boldsymbol{\beta}^p\left(\tilde{\boldsymbol{\beta}}\right) + \tilde{\boldsymbol{\Omega}}_{\text{lattice}}\left(\tilde{\boldsymbol{\beta}}\right) = \begin{bmatrix} \gamma_1 s_1^1 n_1^1 + \gamma_2 s_1^2 n_1^2 & \gamma_1 s_1^1 n_2^1 + \gamma_2 s_1^2 n_2^2 + \theta_3 \\ \gamma_1 s_2^1 n_1^1 + \gamma_2 s_2^2 n_1^2 - \theta_3 & \gamma_1 s_2^1 n_2^1 + \gamma_2 s_2^2 n_2^2 \end{bmatrix} = \tilde{\boldsymbol{\beta}} = \begin{bmatrix} \varepsilon_1^p = \varepsilon^p & \gamma_3^p + \omega_3 \\ \gamma_3^p - \omega_3 & \varepsilon_2^p = -\varepsilon^p \end{bmatrix} \tag{A12}$$

Similar with the 3D case, the residual lattice rotation $\tilde{\boldsymbol{\Omega}}_{\text{lattice}}(\tilde{\boldsymbol{\beta}})$ and plastic distortion $\boldsymbol{\beta}^p(\tilde{\boldsymbol{\beta}})$ in the 2D case can be uniquely determined by solving the Eq. (A12) based on the minimized activated slip systems number assumption. The results are shown in the following Eqs. (A13) and (A1) respectively.

$$\boldsymbol{\beta}^p\left(\tilde{\boldsymbol{\beta}}\right) = \begin{bmatrix} \varepsilon^p & -\dfrac{\sin(\varphi_1+\varphi_2)}{\cos(\varphi_1-\varphi_2)}\varepsilon^p + \dfrac{2\cos\varphi_1\cos\varphi_2}{\cos(\varphi_1-\varphi_2)}\gamma_3^p \\ \dfrac{\sin(\varphi_1+\varphi_2)}{\cos(\varphi_1-\varphi_2)}\varepsilon^p + \dfrac{2\sin\varphi_1\sin\varphi_2}{\cos(\varphi_1-\varphi_2)}\gamma_3^p & -\varepsilon^p \end{bmatrix} \tag{A13}$$

$$\tilde{\boldsymbol{\Omega}}_{\text{lattice}}\left(\tilde{\boldsymbol{\beta}}\right) = \begin{bmatrix} 0 & \omega_3 + \dfrac{\sin(\varphi_1+\varphi_2)}{\cos(\varphi_1-\varphi_2)}\varepsilon^p - \dfrac{\cos(\varphi_1+\varphi_2)}{\cos(\varphi_1-\varphi_2)}\gamma_3^p \\ -\omega_3 - \dfrac{\sin(\varphi_1+\varphi_2)}{\cos(\varphi_1-\varphi_2)}\varepsilon^p + \dfrac{\cos(\varphi_1+\varphi_2)}{\cos(\varphi_1-\varphi_2)}\gamma_3^p & 0 \end{bmatrix} \tag{A14}$$

References

Adams, B.L., 1997. Orientation imaging microscopy: emerging and future applications. Ultramicroscopy 67 (1), 11–17.

Arsenlis, A., Parks, D.M., 1999. Crystallographic aspects of geometrically-necessary and statistically-stored dislocation density. Acta Mater. 47 (5), 1597–1611.

Ashby, M.F., 1970. The deformation of plastically non-homogeneous materials. Philos. Mag. 21 (170), 399–424.

Bilby, B.A., Bullough, R., Smith, E., 1955. Continuous distributions of dislocations: a new application of the methods of non-Riemannian geometry. Proceed. Royal Soc. Lond. Ser. A. Math. Phys. Sci. 231 (1185), 263.

Brewer, L.N., Field, D.P., Merriman, C.C., 2009. Mapping and assessing plastic deformation using EBSD. In: Schwartz, A.J., Kumar, M., Adams, B.L., Field, D.P. (Eds.), Electron Backscatter Diffraction in Materials Science. Springer US, Boston, MA, pp. 251–262.

Britton, T.B., Wilkinson, A.J., 2012. High resolution electron backscatter diffraction measurements of elastic strain variations in the presence of larger lattice rotations. Ultramicroscopy 114, 82–95.

Calcagnotto, M., Ponge, D., Demir, E., Raabe, D., 2010. Orientation gradients and geometrically necessary dislocations in ultrafine grained dual-phase steels studied by 2D and 3D EBSD. Mater. Sci. Eng. A 527 (10–11), 2738–2746.

Dahlberg, C.F.O., Saito, Y., Öztop, M.S., Kysar, J.W., 2014. Geometrically necessary dislocation density measurements associated with different angles of indentations. Int. J. Plast. 54, 81–95.

Dahlberg, C.F.O., Saito, Y., Öztop, M.S., Kysar, J.W., 2017. Geometrically necessary dislocation density measurements at a grain boundary due to wedge indentation into an aluminum bicrystal. J. Mech. Phys. Solid. 105 (Supplement C), 131–149.
Das, S., Hofmann, F., Tarleton, E., 2018. Consistent determination of geometrically necessary dislocation density from simulations and experiments. Int. J. Plast. 109, 18–42.
Di Gioacchino, F., Quinta da Fonseca, J., 2015. An experimental study of the polycrystalline plasticity of austenitic stainless steel. Int. J. Plast. 74, 92–109.
El-Dasher, B.S., Adams, B.L., Rollett, A.D., 2003. Viewpoint: experimental recovery of geometrically necessary dislocation density in polycrystals. Scr. Mater. 48 (2), 141–145.
Field, D.P., Trivedi, P.B., Wright, S.I., Kumar, M., 2005. Analysis of local orientation gradients in deformed single crystals. Ultramicroscopy 103 (1), 33–39.
Fujiyama, K., Mori, K., Kaneko, D., Kimachi, H., Saito, T., Ishii, R., Hino, T., 2009a. Creep damage assessment of 10Cr-1Mo-1W-VNbN steel forging through EBSD observation. Int. J. Press. Vessels Pip. 86 (9), 570–577.
Fujiyama, K., Mori, K., Matsunaga, T., Kimachi, H., Saito, T., Hino, T., Ishii, R., 2009b. Creep-damage assessment of high chromium heat resistant steels and weldments. Mater. Sci. Eng. A 510–511, 195–201.
Fujiyama, K., Saito, T., Mori, K., Hino, T., Ishii, R., 2007. Creep damage assessment through EBSD method and hardness measurement for a high chromium turbine rotor steel forging. ASME Creep 8th.
Gao, H., Huang, Y., 2003. Geometrically necessary dislocation and size-dependent plasticity. Scr. Mater. 48 (2), 113–118.
Gutierrez-Urrutia, I., Raabe, D., 2012. Dislocation density measurement by electron channeling contrast imaging in a scanning electron microscope. Scr. Mater. 66 (6), 343–346.
Jiang, J., Britton, T.B., Wilkinson, A.J., 2013b. Evolution of dislocation density distributions in copper during tensile deformation. Acta Mater. 61 (19), 7227–7239.
Jiang, J., Britton, T.B., Wilkinson, A.J., 2013a. Measurement of geometrically necessary dislocation density with high resolution electron backscatter diffraction: effects of detector binning and step size. Ultramicroscopy 125, 1–9.
Jiang, J., Zhang, T., Dunne, F.P.E., Britton, T.B., 2016. Deformation compatibility in a single crystalline Ni superalloy. Proceed. Roy. Soc. A Math. Phys. Eng. Sci. 472 (2185), 20150690.
Kamaya, M., 2009. Measurement of local plastic strain distribution of stainless steel by electron backscatter diffraction. Mater. Charact. 60 (2), 125–132.
Kamaya, M., 2011. Assessment of local deformation using EBSD: quantification of accuracy of measurement and definition of local gradient. Ultramicroscopy 111 (8), 1189–1199.
Kamaya, M., da Fonseca, J.Q., Li, L.M., Preuss, M., 2007. Local plastic strain measurement by EBSD. Appl. Mech. Mater. 7-8, 173–179.
Kamaya, M., Wilkinson, A.J., Titchmarsh, J.M., 2005. Measurement of plastic strain of polycrystalline material by electron backscatter diffraction. Nucl. Eng. Des. 235 (6), 713–725.
Kamaya, M., Wilkinson, A.J., Titchmarsh, J.M., 2006. Quantification of plastic strain of stainless steel and nickel alloy by electron backscatter diffraction. Acta Mater. 54 (2), 539–548.
Kobayashi, D., Miyabe, M., Achiwa, M., 2014. Failure analysis method of Ni-base superalloy by EBSD observation of the cross section. JSMS 13th Fractographic Conference.
Kobayashi, D., Miyabe, M., Achiwa, M., 2015. Failure analysis and life assessment of thermal fatigue crack growth in a nickel-base superalloy based on EBSD method. ASME Turbo Expo.
Kobayashi, D., Miyabe, M., Kagiya, Y., Sugiura, R., Yokobori, A.T., 2013. An assessment and estimation of the damage progression behavior of IN738LC under various applied stress conditions based on EBSD analysis. Metall. Mater. Trans. A 44 (7), 3123–3135.
Konijnenberg, P.J., Zaefferer, S., Raabe, D., 2015. Assessment of geometrically necessary dislocation levels derived by 3D EBSD. Acta Mater. 99, 402–414.
Kröner, E., 1958. Continuum Theory of Dislocation and Self-Stresses. Springer-Verlag, Berlin.
Kubushiro, K., Sakakibara, Y., Ohtani, T., 2015. Creep strain analysis of austenitic stainless steel by SEM/EBSD. J. Soc. Mater. Sci. Jpn. 64 (2), 106–112.
Kysar, J.W., Gan, Y.X., Morse, T.L., Chen, X., Jones, M.E., 2007. High strain gradient plasticity associated with wedge indentation into face-centered cubic single crystals: geometrically necessary dislocation densities. J. Mech. Phys. Solid. 55 (7), 1554–1573.
Kysar, J.W., Saito, Y., Oztop, M.S., Lee, D., Huh, W.T., 2010. Experimental lower bounds on geometrically necessary dislocation density. Int. J. Plast. 26 (8), 1097–1123.
Lehockey, E.M., Lin, Y.-P., Lepik, O.E., 2000. Mapping residual plastic strain in materials using electron backscatter diffraction. In: Schwartz, A.J., Kumar, M., Adams, B.L. (Eds.), Electron Backscatter Diffraction in Materials Science. Springer US, Boston, MA, pp. 247–264.
Littlewood, P.D., Wilkinson, A.J., 2012. Geometrically necessary dislocation density distributions in cyclically deformed Ti–6Al–4 V. Acta Mater. 60 (15), 5516–5525.
Nye, J.F., 1953. Some geometrical relations in dislocated crystals. Acta Metall. 1 (2), 153–162.
Pantleon, W., 2005. Disorientations in dislocation structures. Mater. Sci. Eng. A 400-401, 118–124.
Pantleon, W., 2008. Resolving the geometrically necessary dislocation content by conventional electron backscattering diffraction. Scr. Mater. 58 (11), 994–997.
Rogowitz, A., Zaefferer, S., Dubosq, R., 2018. Direct observation of dislocation nucleation in pyrite using combined electron channelling contrast imaging and electron backscatter diffraction. Terra Nova 30 (6), 423–430.
Rui, S.-S., Shang, Y.-B., Fan, Y.-N., Han, Q.-N., Niu, L.-S., Shi, H.-J., Hashimoto, K., Komai, N., 2018b. EBSD analysis of creep deformation induced grain lattice distortion: a new method for creep damage evaluation of austenitic stainless steels. Mater. Sci. Eng. A 733, 329–337.
Rui, S.-S., Shang, Y.-B., Qiu, W., Niu, L.-S., Shi, H.-J., Matsumoto, S., Chuman, Y., 2017. Fracture mode identification of low alloy steels and cast irons by electron back-scattered diffraction misorientation analysis. J. Mater. Sci. Technol. 33 (12), 1582–1595.
Rui, S.-S., Shang, Y.-B., Su, Y., Qiu, W., Niu, L.-S., Shi, H.-J., Matsumoto, S., Chuman, Y., 2018a. EBSD analysis of cyclic load effect on final misorientation distribution of post-mortem low alloy steel: a new method for fatigue crack tip driving force prediction. Int. J. Fatigue 113, 264–276.
Sarac, A., Kysar, J.W., 2018. Experimental validation of plastic constitutive hardening relationship based upon the direction of the net burgers density vector. J. Mech. Phys. Solid. 111 (Supplement C), 358–374.
Sarac, A., Oztop, M.S., Dahlberg, C.F.O., Kysar, J.W., 2016. Spatial distribution of the net burgers vector density in a deformed single crystal. Int. J. Plast. 85, 110–129.
Schwartz, A.J., Kumar, M., Adams, B.L., Field, D.P., 2009. Electron Backscatter Diffraction in Materials Science, Second Edition Springer.
Shen, R.R., Efsing, P., 2018. Overcoming the drawbacks of plastic strain estimation based on KAM. Ultramicroscopy 184, 156–163.
Sun, S., Adams, B.L., King, W.E., 2000. Observations of lattice curvature near the interface of a deformed aluminium bicrystal. Philos. Mag. A 80 (1), 9–25.
Sun, S., Adams, B.L., Shet, C., Saigal, S., King, W., 1998. Mesoscale investigation of the deformation field of an aluminum bicrystal. Scr. Mater. 39 (4), 501–508.
Tasan, C.C., Diehl, M., Yan, D., Zambaldi, C., Shanthraj, P., Roters, F., Raabe, D., 2014a. Integrated experimental–simulation analysis of stress and strain partitioning in multiphase alloys. Acta Mater. 81, 386–400.
Tasan, C.C., Hoefnagels, J.P., Diehl, M., Yan, D., Roters, F., Raabe, D., 2014b. Strain localization and damage in dual phase steels investigated by coupled in-situ deformation experiments and crystal plasticity simulations. Int. J. Plast. 63, 198–210.
Vilalta-Clemente, A., Naresh-Kumar, G., Nouf-Allehiani, M., Gamarra, P., di Forte-Poisson, M.A., Trager-Cowan, C., Wilkinson, A.J., 2017. Cross-correlation based high resolution electron backscatter diffraction and electron channelling contrast imaging for strain mapping and dislocation distributions in InALN thin films. Acta Mater. 125, 125–135.
Wallis, D., Hansen, L.N., Ben Britton, T., Wilkinson, A.J., 2016. Geometrically necessary dislocation densities in olivine obtained using high-angular resolution electron backscatter diffraction. Ultramicroscopy 168, 34–45.
Wallis, D., Hansen, L.N., Britton, T.B., Wilkinson, A.J., 2017. Dislocation interactions in olivine revealed by HR-EBSD. J. Geophys. Res. Solid Earth.
Wei, S., Kim, J., Tasan, C.C., 2019. Boundary micro-cracking in metastable Fe45Mn35Co10Cr10 high-entropy alloys. Acta Mater. 168, 76–86.

Wilkinson, A.J., Randman, D., 2010. Determination of elastic strain fields and geometrically necessary dislocation distributions near nanoindents using electron back scatter diffraction. Philos. Mag. 90 (9), 1159–1177.
Wright, S.I., Nowell, M.M., Field, D.P., 2011. A review of strain analysis using electron backscatter diffraction. Microsc. Microanal. 17 (3), 316–329.
Wright, S.I., Suzuki, S., Nowell, M.M., 2016. In situ EBSD observations of the evolution in crystallographic orientation with deformation. JOM 68 (11), 2730–2736.
Yan, D., Tasan, C.C., Raabe, D., 2015. High resolution in situ mapping of microstrain and microstructure evolution reveals damage resistance criteria in dual phase steels. Acta Mater. 96, 399–409.
Zaefferer, S., Elhami, N.-N., 2014. Theory and application of electron channelling contrast imaging under controlled diffraction conditions. Acta Mater. 75, 20–50.